

HE  
18.5  
.A38  
no.DOT-  
TSC-171-1

REPORT NO. DOT-TSC-171-1

DEPARTMENT OF  
TRANSPORTATION

JAN 18 1973

Library

# DEVELOPMENT OF METHODS FOR PREDICTING AIRLOADS ON TACV CONFIGURATIONS DUE TO STRONG CROSSWIND GUSTS

J. R. RUETENIK, G. ZARTARIAN  
KAMAN AVIDYNE  
83 SECOND AVE.  
N. W. INDUSTRIAL PARK  
BURLINGTON, MA. 01803

MARCH 1972  
INTERIM REPORT



Availability is Unlimited. Document may be Released  
To the National Technical Information Service,  
Springfield, Virginia 22151, for Sale to the Public.

Prepared for:

DEPARTMENT OF TRANSPORTATION  
TRANSPORTATION SYSTEMS CENTER  
CAMBRIDGE, MA. 02142

The contents of this report reflect the views of Kaman AviDyne which is responsible for the facts and the accuracy of the data presented herein. The contents do not necessarily reflect the official views or policy of the Department of Transportation. This report does not constitute a standard, specification or regulation.

## TECHNICAL REPORT STANDARD TITLE PAGE

1. Report No. 71-1 DOT-TSC-171-1,	2. Government Accession No.	3. Recipient's Catalog No. DEPARTMENT OF TRANSPORTATION	
4. Title and Subtitle Development of Methods for Predicting Airloads on TACV Configurations Due to Strong Cross- Wind Gusts.		5. Report Date JAN 18 1973 March 27, 1972	
7. Author(s) J. Ray Ruetenik and Garabed Zartarian		6. Performing Organization Code LIBRARY	
9. Performing Organization Name and Address Kaman AviDyne. 83 Second Avenue N.W. Industrial Park Burlington, Ma. 01803		10. Work Unit No.	
12. Sponsoring Agency Name and Address Department of Transportation Transportation Systems Center (TSC) Cambridge, MA 02142		11. Contract or Grant No. DOT-TSC-171	
15. Supplementary Notes		13. Type of Report and Period Covered Interim Report	
16. Abstract Equations for predicting the transient side force and yawing moment on TACV cars due to a strong side gust are developed. The protection afforded by side rails is estimated. The equations account for transient slender-body effects and growth of vortices on the lee side. For a vehicle speed of 150 mph, the analysis indicates a side gust of 60 mph would produce a transient peak in side force of 1x the steady-state value for the first car to 4.3x for the third car. An unresolved uncertainty of a factor of two in predicting the steady-state side force on TACV models in wind-tunnel tests with a moving ground plane is attributed to flow effects between the vehicle bottom and the ground plane.			
Because of questions regarding ground-plane simulation in wind-tunnel tests, effect of side rails on gust airloads, and the airloads due to passing trains, the feasibility of developing a facility for measuring forces and moments on moving models is explored. It is concluded that a laboratory facility with a 25-30 ft track for testing 1-ft length models at 100 fps would provide useful data; principal development problems would be associated with model-support vibration and model-balance measurement. A larger facility with a 120-140 ft track for testing 4-5 ft length models would provide good Reynolds-number simulation, readily met model guideway tolerance requirements and greater ease of measurement.			
17. Key Words Tracked Air Cushion Vehicles Crosswinds Gust Loadings	18. Distribution Statement Availability is Unlimited. Document may be Released To the National Technical Information Service, Springfield, Virginia 22151, for Sale to the Public.		
19. Security Classif. (of this report) Unclassified	20. Security Classif. (of this page) Unclassified	21. No. of Pages 106	22. Price



## FOREWORD

This research was carried out by the Kaman AviDyne Division of Kaman Sciences Corporation, Burlington, Massachusetts, for the Department of Transportation, Transportation Systems Center, Cambridge, Massachusetts, under Contract No. DOT-TSC-171. Dr. Timothy M. Barrows of the Technology Directorate, Power and Propulsion Branch, served as the technical monitor.

Dr. J. Ray Ruetenik was the Project Leader under Dr. Norman P. Hobbs, Technical Director of Kaman AviDyne. The authors would like to express appreciation for the constructive guidance provided by Dr. Barrows through the technical reviews during the progress of this work.



## SUMMARY

Equations for predicting the transient side force and yawing moment on TACV cars due to a strong side gust are developed. The protection afforded by side rails is estimated. The equations account for transient slender-body effects and growth of vortices on the lee side. For a vehicle speed of 150 mph, the analysis indicates a side gust of 60 mph would produce a transient peak in side force of 1x the steady-state value for the first car to 4.3x for the third car. An unresolved uncertainty of a factor of two in predicting the steady-state side force on TACV models in wind-tunnel tests with a moving ground plane is attributed to flow effects between the vehicle bottom and the ground plane.

Because of questions regarding ground-plane simulation in wind-tunnel tests, effect of side rails on gust airloads, and the airloads due to passing trains, the feasibility of developing a facility for measuring forces and moments on moving models is explored. It is concluded that a laboratory facility with a 25-30 ft track for testing 1-ft length models at 100 fps would provide useful data; principal development problems would be associated with model-support vibration and model-balance measurement. A larger facility with a 120-140 ft track for testing 4-5 ft length models would provide good Reynolds-number simulation, readily met model guideway tolerance requirements and greater ease of measurement.



## TABLE OF CONTENTS

<u>SECTION</u>	<u>TITLE</u>	<u>PAGE</u>
1	INTRODUCTION . . . . .	1-1
2	ANALYSIS OF LATERAL GUST LOADS . . . . .	2-1
	2.1 Introduction . . . . .	2-1
	2.2 Development of Equations for First Car . .	2-2
	2.3 Results for First Car . . . . .	2-18
	2.4 Equations for N <sup>th</sup> Car . . . . .	2-37
	2.5 Results for Second and Third Car . . . .	2-39
	2.6 Conclusions . . . . .	2-57
3	FEASIBILITY ANALYSIS OF LABORATORY FACILITY FOR MEASURING TACV GUST LOADS . . . . .	3-1
	3.1 Introduction . . . . .	3-1
	3.2 General Considerations . . . . .	3-2
	3.3 Cable System . . . . .	3-13
	3.4 Accelerate-Coast-Decelerate System . . . .	3-19
	3.5 Force and Moment Balance . . . . .	3-24
	3.6 Conclusions . . . . .	3-34
4	REFERENCES	



## LIST OF ILLUSTRATIONS

<u>FIGURE</u>	<u>TITLE</u>	<u>PAGE</u>
2.1	Sketch of Representative Vehicle Constructed for Basis of Analysis . . . . .	2-3
2.2	Functions in Equation (2.9) . . . . .	2-9
2.3	g-function in Equation (2.15) . . . . .	2-11
2.4	Comparison of Steady-State Section Side Force Measured by Perkins and Jorgensen (NASA TN D-3716) and the Predicted Values of the Slender-Body Theory (Equation 2.9) and the Ruetenik-Brooks Theory (Equations 2.10 and 2.18) . . . . .	2-14
2.5	Variation of Side-Rail Factor With Side-Rail Height for Viscous Cross-Flow. First Car . . . . .	2-17
2.6	Variation of Side-Force Coefficient With Reduced Time for Various Side-Rail Heights. First Car . . . . .	2-19
2.7	Variation of Yawing-Moment Coefficient With Reduced Time for Various Side-Rail Heights . . . . .	2-25
2.8	Variation of Steady-State Side-Force Coefficient With Side-Rail Height. First Car, 3-Caliber Nose. . . . .	2-29
2.9	Variation of Yawing-Moment Coefficient With Side-Rail Height. First Car, 3-Caliber Nose . . . . .	2-30
2.10	Drawing of Vehicle Configurations Tested by Grunwald (NASA TN D-5935). All Noses Elliptical. Dimensions Based on Vehicle Length . . . . .	2-31
2.11	Comparison of Predicted Side-Force Coefficient With Values Measured in Three Wind-Tunnel Tests Over a Range of Sideslip Angles . . . . .	2-33
2.12	Comparison of Side-Force Coefficient Measured by Grunwald (NASA TN D-5935) for Six Configurations as a Function of Gap Height above Ground Plane $\beta = 20^\circ$ . . . . .	2-36
2.13	Variation of Side-Force Coefficient With Reduced Time for Various Side-Rail Heights. Second Car. . . . .	2-40
2.14	Variation of Yawing-Moment Coefficient With Reduced Time for Various Side-Rail Heights. Second Car. . . . .	2-43
2.15	Variation of Side-Force Coefficient With Reduced Time for Various Side-Rail Heights. Third Car. . . . .	2-46
2.16	Variation of Yawing-Moment Coefficient With Reduced Time for Various Side-Rail Heights. Third Car. . . . .	2-49

LIST OF ILLUSTRATIONS (CONT.)

<u>FIGURE</u>	<u>TITLE</u>	<u>PAGE</u>
3.1	Layout of Experimental Track . . . . .	3-3
3.2	Configuration of Representative Model Selected for Feasibility Study . . . . .	3-4
3.3	Schematic Drawing of Model, Components, Balance, Strut, Carriage and Way . . . . .	3-6
3.4	Comparison of Reynolds Number Based on Model Length for Three Models and Values for Models Tested in Wind Tunnels as a Function of Model Speed. $\beta = 20^\circ$ . . . . .	3-8
3.5	Side-Force for Three Models as a Function of Model Speed. $\beta = 20^\circ$ . . . . .	3-10
3.6	Side-Force/Model-Weight Ratio for Three Models as a Function of Model Speed . . . . .	3-11
3.7	Distance Required to Attain Test Speed With Constant Acceleration From Rest . . . . .	3-12
3.8	Variation of Acceleration With Period for Sinusoid as a Function of Half Amplitude . . . . .	3-14
3.9	Schematic Drawing of Test Facility Using Cable-Propelled Models . . . . .	3-15
3.10	Schematic Drawing of Cable-Propelled Model and Carriage-Way System . . . . .	3-17
3.11	Sketch of Air-Piston Accelerator to Propel Model . . . . .	3-20
3.12	Sketch of Channel-Brake for Model Deceleration . .	3-22
3.13	Sketch of Arresting Cable System for Model Deceleration . . . . .	3-23
3.14	Sketch of Cantilever Side-Force Balance . . . . .	3-25
3.15	First Frequency and Static Nose Deflection as a Function of Dimensions for Side-Force Balance With Rectangular Beam Cross Section. $W = 0.9$ lb., $\Delta e = 50\mu$ in/in . . . . .	3-27
3.16	First Frequency and Static Nose Deflection as a Function of Dimensions for Side-Force Balance With Rectangular Beam Cross Section. $W = 0.5$ lb., $\Delta e = 20\mu$ in/in . . . . .	3-28
3.17	First Frequency and Static Nose Deflection as a Function of Dimensions for Cut-Out-Beam Side-Force Balance . . . . .	3-30

LIST OF ILLUSTRATIONS (CONT.)

<u>FIGURE</u>	<u>TITLE</u>	<u>PAGE</u>
3.18	Differential Static Strain Signal as a Function of First Frequency for Cut-Out-Beam Side-Force Balance . . . . .	3-31
3.19	Sketch of Rolling-Moment Balance . . . . .	3-32
3.20	Sketch of Yawing-Moment Balance . . . . .	3-33

TABLE

<u>TABLE</u>	<u>TITLE</u>	<u>PAGE</u>
3.1	MODEL DESIGN CHARACTERISTICS . . . . .	3-7



## SYMBOLS

A	base area
$C_n$	yawing-moment coefficient, $M_z/SLq$
$C_Y$	side-force coefficient, $Y/Sq$
$\bar{C}_Y$	side-force coefficient based on base area, $Y/Aq$
H	nominal height setting of model from ground belt (NASA TN D-5935)
L	body length
M	vehicle relative Mach number, $v_r/a$
$M_z$	yawing moment (Fig. 2.1)
N	car number in train
S	reference area $\pi H_v^2/2$ for TACV-type body $\pi r_b^2$ for body with circular or elliptic cross section
V	vehicle velocity
Y	side force
a	sound speed
$d_e$	diameter of a circle with cross-sectional area equivalent to maximum cross-sectional area of model (NASA TN D-5935)
$f, f_o$	functions in Equation (2.9)
$g, g_L, g_T$	functions in Equation (2.15)
$h_v, H_v, \bar{h}_v$	vehicle local, maximum and reduced height, $\bar{h}_v = h_v/H_v$
$h_w$	side-rail height
k	constant in Equation (2.15)
$\Delta p$	differential pressure between corresponding windward and lee sides of body

$q$	dynamic pressure, $\rho v_r^2/2$
$r_b$	radius of circle or semi-axis of ellipse normal to $x$ coordinate
$r_w$	side-rail factor
$t$	time
$\bar{t}$	reduced time, $V\beta t/H_v$
$v_c$	cross-wind velocity
$v_r$	relative velocity, $\sqrt{V^2 + v_c^2}$
$x, z$	longitudinal and vertical coordinates (Fig. 2.1)
$\beta$	sideslip angle
$\gamma$	nondimensional wall height, $h_w/H_v$
$\bar{\gamma}$	function in Equation (2.15)
$\lambda$	reduced body length, $L/H_v$
$\lambda_1$	reduced length of body nose (Fig. 2.1)
$\xi, \zeta$	reduced coordinates; $\xi = x/H_v$ , $\zeta = z/H_v$
$\xi_1$	$\xi$ -coordinate where side-rail height equals body height
$\sigma$	function defined in Equation (2.16)
$\tau$	reduced time, $at/H_v$

### Subscripts

$a$	cylindrical section
$c$	viscous, cross-flow value
$f$	nose section
$s$	slender-body value

## 1. INTRODUCTION

At the speeds being considered for TACV, ranging from 150 to 300 miles per hour, side gust airloads could be an important design factor. For example, the protection against gust airloads provided by the side rails of a U-guideway may be a critical factor to guideway selection.

Conservative estimates (upper bounds) of the side force probably can be made at present, but available data indicate this estimate may be two to five times greater, or more, than might be necessary if results of further tests and analysis were available. A conservative estimate, although satisfactory from a safety point of view, could impose significant sacrifice in ride quality and initial cost of guideway.

The objective of the study reported here is (1) to propose an engineering method for predicting cross-wind gust loadings on tracked-air-cushion-vehicle (TACV) configurations in trains of one to three cars and (2) to propose a laboratory facility for measuring cross-wind gust loadings on TACV models.

The method developed by Ruetenik and Brooks<sup>1</sup> for predicting the aerodynamic forces on a body of revolution undergoing indicial sinking (step function sinking rate) indicates the transient force on rearward portions of a body for high sink rates could be as much as 5 times greater than the steady-state value. Airloads during the brief period of gust envelopment would differ from the airloads during the corresponding period of indicial motion; but the greatest airloads on a body suddenly subjected to a large angle of attack or sideslip are expected from vortices formed on the lee side, and analysis indicates this airloads peak would be reached well after gust envelopment, thereby being essentially the same as for indicial translation (provided the relative angles of sideslip, etc., are equal).

In Section 2 the method of Ruetenik and Brooks<sup>1</sup> is used to estimate the transient side force and yawing moment on TACV-type configurations in trains of one or more cars. Three guideway side-rail heights are considered: 0, 30 and 60 percent of the vehicle height. The results indicate the peak transient side force and yawing moment on a single-car TACV (or first car of a TACV train) would nearly equal the steady-state values, the peak transient side force on the second car of a multiple car train would be roughly 1 to 2 times the steady-state side force and on the third car would be about 2 to 4 times its steady-state value.

Wind-tunnel data are examined in Section 2 with respect to the effect of vehicle cross section, ground-plane gap height and side-rail height on the steady-state side force.

Side-force measurements by Grunwald<sup>2</sup> on TACV-type configurations in a wind-tunnel with a moving-belt ground plane indicate unresolved differences for various configurations amounting to a factor of two. Because of questions regarding ground-plane simulation, effect of side rails and effect of passing trains, a feasibility study is described in Section 3 of a laboratory facility using moving models on stationary tracks for measurement of airloads.

## 2. ANALYSIS OF LATERAL GUST LOADS

### 2.1 INTRODUCTION

The two classical unsteady aerodynamic models are the Küssner gust with a front fixed in space, leading to gust envelopment at the vehicle speed, and the Wagner model of indicial body motion, which corresponds to instantaneous gust envelopment. Gust envelopment in the atmosphere presumably falls somewhere between.

Lateral gust envelopment of a side-railed TACV, compared to aircraft or missile envelopment, is complicated by passage over the windward rail in front of the vehicle. The cylindrical portion of the body may be close enough to the rails that the body and rails here can be considered one body. Ahead of the body the siderails are a disturbance to the flow.

At large angles of sideslip, such as  $20^\circ$ , the vortices on the leeward side, formed by separation of the viscous flow, are a principal factor in the loading. Leeward vortices are expected to grow slowly compared with presumed gust envelopment times, so it would appear that the rate of gust envelopment is of secondary importance for large gust-induced angles of sideslip.

Ruetenik and Brooks<sup>1</sup> have developed a method for prediction of the transient body forces on bodies of revolution due to indicial sinking, the Wagner model, that embodies the growth of leeward vortices at large angles of attack, so this method is adopted here to the rail problem. Semiempirical factors are developed to account for the non-circular cross section of the vehicle, side rail and ground-plane image. Side-rail blockage is estimated using the pressure distribution data measured by Perkins and Jorgensen<sup>3</sup> on a body of revolution.

The side-rail disturbance effect ahead of the vehicle is not accounted for here, because of the lack of experimental data. The leeward vortex is expected to experience relatively small growth on the nose, so flow disturbance by the windward rail may

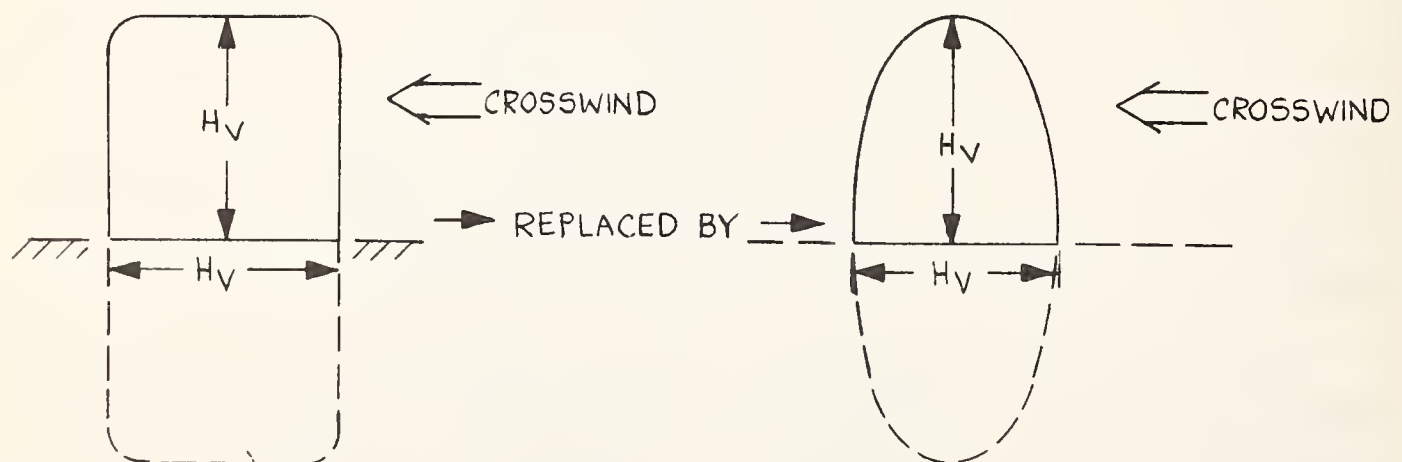
be unimportant. If, however, the origin of leeward vortices is moved rearward due to siderail blockage, the side force could be reduced significantly, which would make the disturbance important. These questions await resolution by experiment. In the meantime, the present analysis provides a method for estimating the transient, viscous airloads on a basis believed to be conservative, that is, estimates on the high side.

A single-car TACV is analyzed in Sections 2.2 and 2.3. The equations developed would apply also to the first car of a multi-car TACV train. These equations are extended in Section 2.4 to other cars in a multi-car TACV train.

## 2.2 DEVELOPMENT OF EQUATIONS FOR FIRST CAR

### Assumptions and Definitions

The vehicle configuration drawn in Figure 2.1 is used for development of this analysis. The frontal view shows a nearly square cross-section. For aerodynamic purposes, the clearance from the ground is assumed zero. The loads on this cross-section are assumed to be those of the top half of a larger body, the larger body being the sum of section A-A and its image about the ground. For the further simplification, the cross-section A-A is replaced by the top half of a 2:1 ellipse as shown in the sketch below.



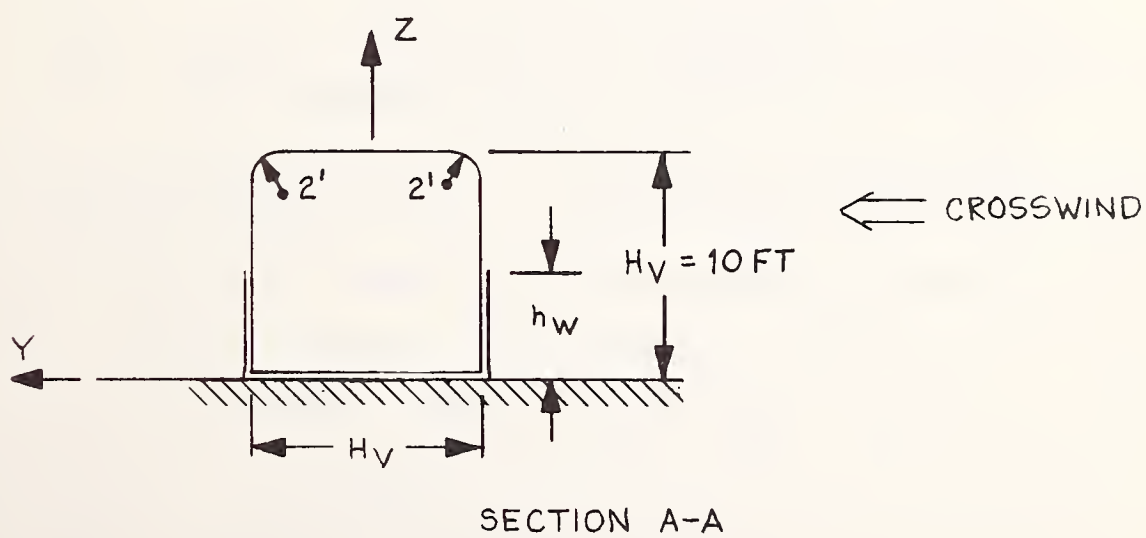
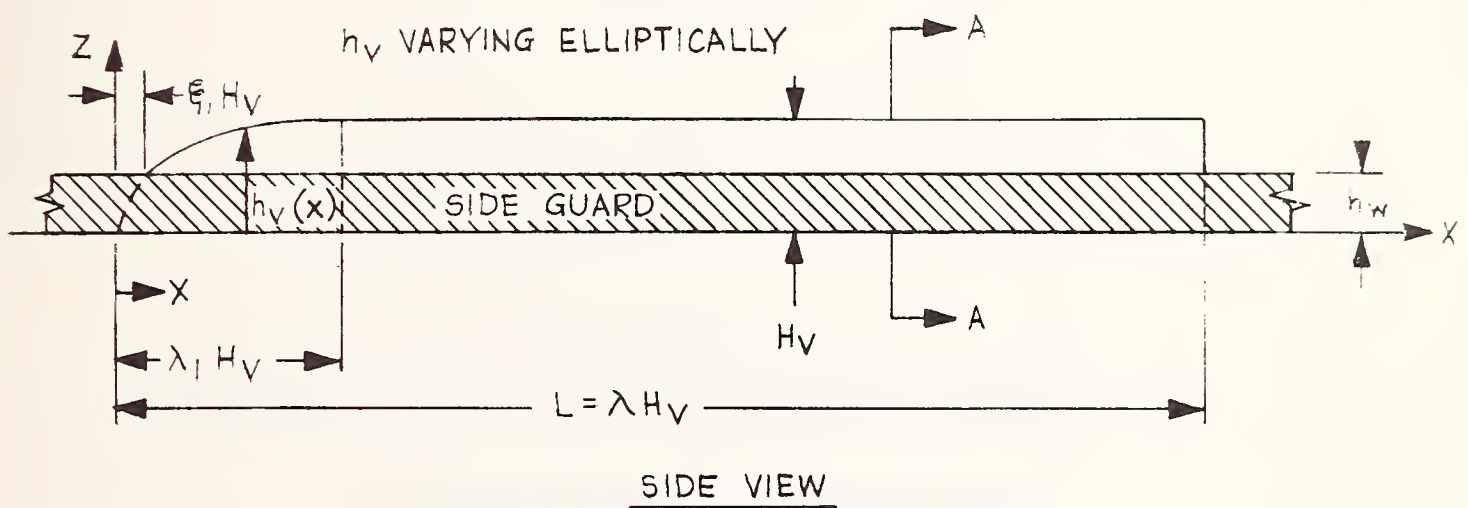
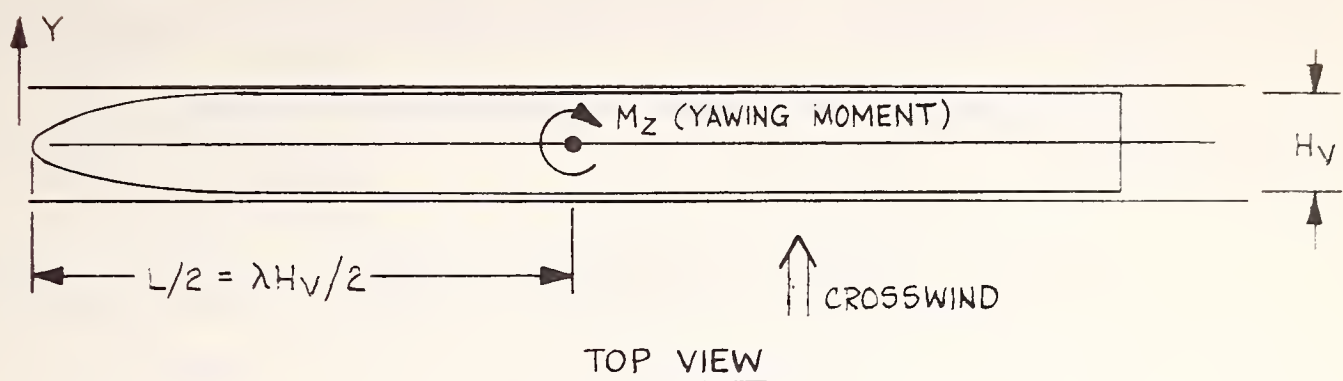


Fig. 2.1 Sketch of Representative Vehicle Constructed for Basis of Analysis.

The cross sections at any  $x$  are assumed similar to section A-A, differing only in scale. The characteristic dimension at station  $x$  is the train height  $h_v(x)$ , Figure 2.1.

An elliptic nose shape is assumed of length  $\lambda_1 H_v$ , described by

$$h_v(x) = H_v \left[ \frac{x}{\lambda_1 H_v} \left( 2 - \frac{x}{\lambda_1 H_v} \right) \right]^{1/2} \quad \text{for } x \leq \lambda_1 H_v$$

Defining  $\xi = x/H_v$  and  $\bar{h}_v(\xi) = h_v(x)/H_v$ , the body height is

$$\begin{aligned} \bar{h}_v(\xi) &= \left[ \frac{\xi}{\lambda_1} \left( 2 - \frac{\xi}{\lambda_1} \right) \right]^{1/2} & \xi \leq \lambda_1 \\ &= 1 & \xi \geq \lambda_1 \end{aligned} \quad (2.1)$$

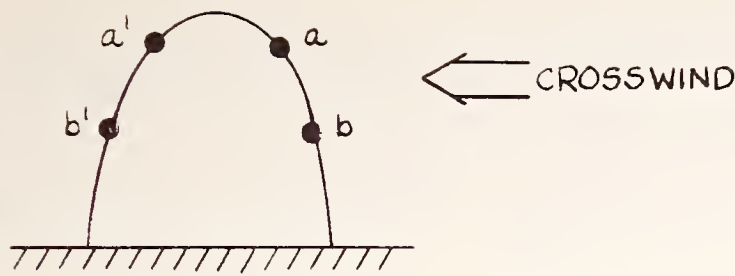
Following the work of Ruetenik and Brooks,<sup>1</sup> the aerodynamic loading is assumed to be made up of two parts:

- a) Non-viscous, slender-body part.
- b) Viscous, cross-flow part incorporating the leeward vortices.

The parts are discussed and computed separately.

The side rail or guard is assumed to be part of the elliptical surface. However, in computing lateral loads and moments, loads on the side rails are omitted. This means that all train surfaces below the top of the guard rail,  $z < h_w$ , do not contribute to the side force  $Y$ , or the yawing moment,  $M_x$ .

Define  $\Delta p$  as the pressure difference of two "corresponding points," one on the windward side and the other on the leeward side, as shown in the sketch below. Let  $Y$  and  $M_z$  be divided into two parts each. The first, subscripted by  $f$ , represents the contribution of the nose section; the second, subscripted by  $a$ , represents the contribution of the cylindrical afterbody.



$$\Delta p_a = p_a - p_{a'}$$

$$\Delta p_b = p_b - p_{b'}, \text{ etc. . . .}$$

Define the coefficients for side force and yawing moment

$$C_Y = \frac{Y}{Sq} \quad (2.2)$$

$$C_n = \frac{M_z}{SLq} \quad (2.3)$$

where

$q$  = the dynamic pressure,  $1/2 \rho v_r^2$

$v_r$  = relative wind,  $\sqrt{V^2 + v_c^2}$

$V$  = train speed

$v_c$  = cross wind velocity

$S$  = reference area,

$$= \begin{cases} \frac{\pi H_v^2}{2} & \text{for TACV type body} \\ \pi r_b^2 & \text{for circle or elliptic section} \end{cases}$$

$r_b$  = radius of circle or semi-axis of ellipse normal to flow direction

Define the reduced parameters  $\gamma = h_w/H_v$ ,  $\zeta = z/H_v$  and  $\xi_1$  is the  $\xi_1$ -station where  $h_v = h_w$ , and  $\xi_1 = (1 - \sqrt{1 - \gamma^2})$ . Note that  $\Delta p \equiv \Delta p(\xi, \zeta; t)$ . The force and moment coefficients become

$$C_Y = C_{Y_f} + C_{Y_a} \quad (2.4)$$

where

$$C_{Y_f} = \frac{2}{\pi} \int_{\xi_1}^{\lambda_1} \int_{\gamma}^{\bar{h}_v(\xi)} \frac{\Delta p}{q} d\zeta d\xi$$

$$C_{Y_a} = \frac{2}{\pi} \int_{\lambda_1}^{\lambda} \int_{\gamma}^1 \frac{\Delta p}{q} d\zeta d\xi$$

$$C_n = C_{n_f} + C_{n_a} \quad (2.5)$$

where

$$C_{n_f} = \frac{1}{2} C_{Y_f} - \frac{2}{\pi \lambda} \int_{\xi_1}^{\lambda_1} \xi \int_{\gamma}^{\bar{h}_v(\xi)} \frac{\Delta p}{q} d\zeta d\xi$$

$$C_{n_a} = \frac{1}{2} C_{Y_a} - \frac{2}{\pi \lambda} \int_{\lambda_1}^{\lambda} \xi \int_{\gamma}^1 \frac{\Delta p}{q} d\zeta d\xi$$

Let subscript *s* denote the part evaluated by slender-body theory and subscript *c* denote the additional loads due to viscous "cross flow." Thus

$$Y_f = Y_{fs} + Y_{fc}$$

$$C_{Y_f} = C_{Y_{fs}} + C_{Y_{fc}}$$

$$\frac{\Delta p}{q} = \left(\frac{\Delta p}{q}\right)_s + \left(\frac{\Delta p}{q}\right)_c, \text{ etc.}$$

Slender-body part of loads - The theoretical loading distribution on a slender body with elliptical cross sections, Nielsen<sup>4</sup> (p. 78), is used. The following integral is valid for a steady-state angle of sideslip  $\beta$ .

$$\int_0^{\bar{h}_v(\xi)} \left( \frac{\Delta p}{q} \right)_s d\xi = 2\pi \bar{h}_v(\xi) \bar{h}_v'(\xi) \beta \quad (2.6)$$

where  $\bar{h}_v'(\xi) \equiv d\bar{h}_v/d\xi$ . Define  $r_w$ .

$$r_w \equiv \frac{\int_0^{\bar{h}_v(\xi)} \frac{\Delta p}{q} d\xi}{\int_0^{\bar{h}_v(\xi)} \frac{\Delta p}{q} d\xi} \quad (2.7)$$

which accounts for the shielding of the side rails. For the loading distribution on the 2:1 elliptical section sketched on page 2-2 at a constant sideslip angle, it can be shown

$$r_{ws}(\xi, \gamma) = \frac{4}{\pi} \left\{ \delta_w - \frac{1}{2} \tan^{-1}(2 \tan \delta_w) \right\} \quad (2.8)$$

where

$$\delta_w = \cos^{-1} \left( \frac{\gamma}{\bar{h}_v(\xi)} \right) \quad \gamma < \bar{h}_v(\xi) < 1$$

Reference 1 adopted the following equation from Miles<sup>5</sup> for the transient case

$$\int_0^{\bar{h}_v(\xi)} \left( \frac{\Delta p}{q} \right)_s d\xi = \pi \left\{ 2 \bar{h}_v' f_o(\tau) + \frac{1}{M} f(\tau) \right\} \bar{h}_v \beta \quad (2.9)$$

where

$$\tau = at/h_v(x) = at/(\bar{h}_v(\xi)H_v)$$

The functions  $f_o(\tau)$  and  $f(\tau)$  from reference 5 are given in Figure 2.2. It is assumed that the side-rail factor  $r_{ws}(\xi)$  for a fixed angle of sideslip applies to the transient case, so

$$\int_{\gamma}^{\bar{h}_v(\xi)} \left( \frac{\Delta p}{q} \right)_s d\xi = \pi \left\{ 2 \bar{h}'_v f_o(\tau) + \frac{1}{M} f(\tau) \right\} \bar{h}_v r_{ws}(\xi, \gamma) \beta \quad (2.10)$$

Defining the following integrals

$$\begin{aligned} I_1(\gamma) &= \int_{\xi_1}^{\lambda_1} \bar{h}_v(\xi) \bar{h}'_v(\xi) r_{ws}(\xi, \gamma) d\xi \\ I_2(\gamma) &= \int_{\xi_1}^{\lambda_1} \bar{h}_v(\xi) r_{ws}(\xi, \gamma) d\xi \\ I_3(\gamma) &= \int_{\xi_1}^{\lambda_1} \xi \bar{h}_v(\xi) \bar{h}'_v(\xi) r_{ws}(\xi, \gamma) d\xi \\ I_4(\gamma) &= \int_{\xi_1}^{\lambda_1} \xi \bar{h}_v(\xi) r_{ws}(\xi, \gamma) d\xi \end{aligned}$$

the following equations are obtained for the coefficients

$$C_{Y_{fs}} = 2 \left[ 2 I_1(\gamma) f_o(\tau) + \frac{1}{M} I_2(\gamma) f(\tau) \right] \beta \quad (2.11)$$

$$C_{Y_{as}} = \frac{2}{M} r_{ws}(\lambda_1, \gamma) (\lambda - \lambda_1) f(\tau) \beta \quad (2.12)$$

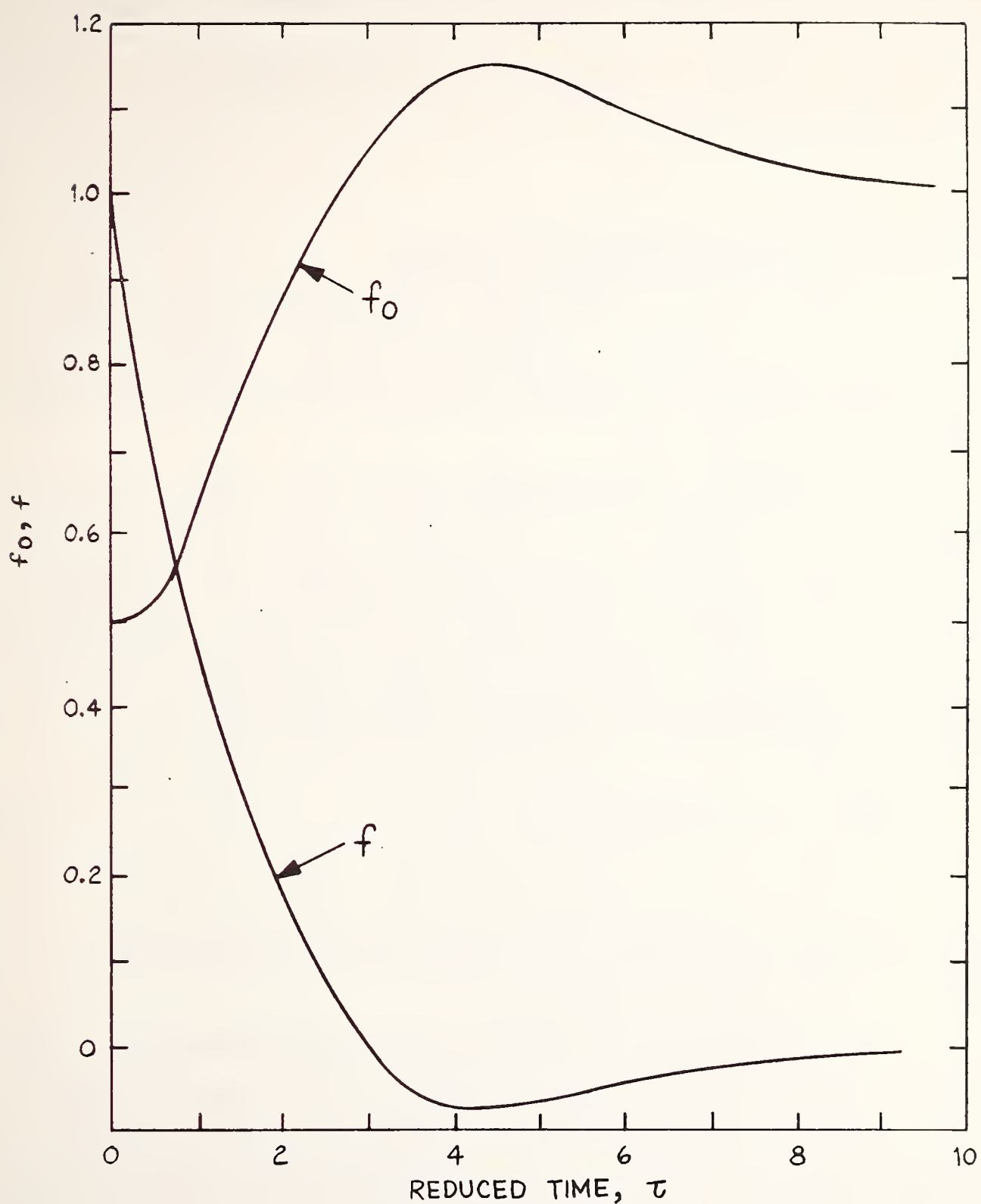


Fig. 2.2 Functions in Equation (2.9).

$$C_{n_{fs}} = \frac{1}{2} C_{Y_{fs}} - \frac{2}{\lambda} \left[ 2I_3(\gamma) f_o(\tau) + \frac{1}{M} I_4(\gamma) f(\tau) \right] \beta \quad (2.13)$$

$$C_{n_{as}} = \frac{1}{2} C_{Y_{as}} - \frac{1}{\lambda M} r_{ws}(\lambda_1, \gamma) (\lambda^2 - \lambda_1^2) f(\tau) \beta \quad (2.14)$$

### Viscous Cross-Flow Part of Loading

For the viscous cross-flow, the method of Ruetenik and Brooks<sup>1</sup> is also adopted. Here the body is assumed to be a cylinder from the tip of the nose rearward, which provided good correlation in reference 1.

Two factors are introduced into the loading expression of reference 1: a factor  $\bar{\zeta}(\zeta)$  to account for the distribution of loading around the body at an axial station, and a factor  $k$  to incorporate the effects of body cross-sectional configuration, nose profile and other differences between measured forces and those given by reference 1. The resulting equation is

$$\left( \frac{\Delta p}{q} \right)_c = k \bar{\zeta}(\zeta) g(\sigma) \beta^2 \quad (2.15)$$

where  $g(\sigma)$  is the modified-Bryson function<sup>6</sup> of reference 1 (Figure 9), reproduced in Figure 2.3.

Two functions for  $g(\sigma)$  are given in reference 1. The selection is made on the basis of whether the boundary layer on the body is laminar or turbulent; if laminar,  $g_L(\sigma)$  is used, and if turbulent,  $g_T(\sigma)$ . The latter would generally be applicable, except for models in wind tunnels at subcritical Reynolds numbers.

The theoretical function  $g(\sigma)$  given in reference 1 is for a body with a circular cross-section. For other bodies, an equivalent circular section must be selected. A correspondence

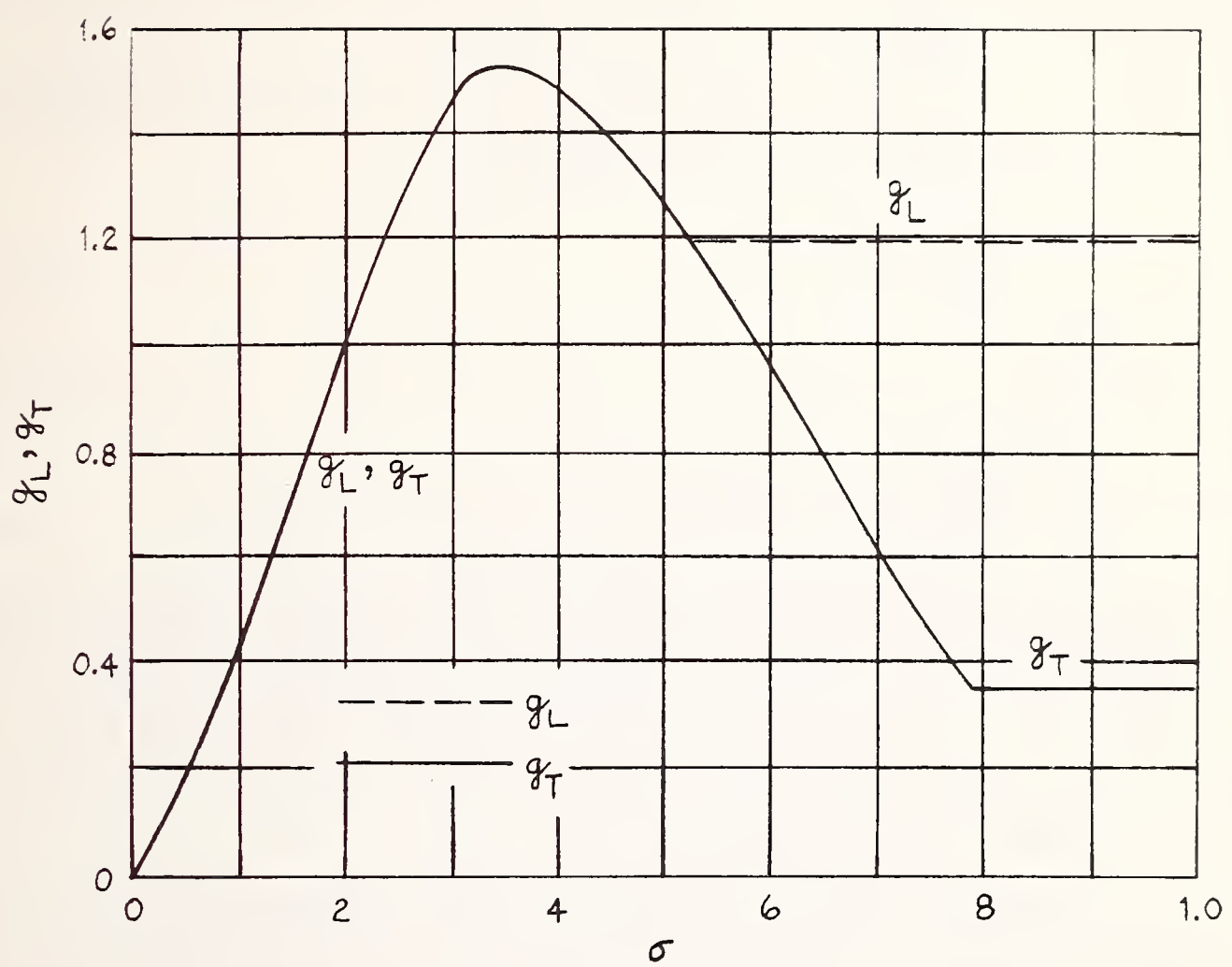


Fig. 2.3  $g$ -function in Equation (2.15)

is taken from slender-body theory, for which the equivalent circular section is the one with a diameter equal to the maximum dimension transverse to the flow direction,  $2H_v$  for the present body.

Therefore

$$\begin{aligned}\sigma &= \frac{x\beta}{H_v} & x \leq Vt \\ &= \frac{V\beta t}{H_v} & x > Vt\end{aligned}\tag{2.16}$$

The function  $\bar{\zeta}(\zeta)$  is defined so

$$\int_0^1 \bar{\zeta}(\zeta) d\zeta = 1\tag{2.17}$$

and therefore

$$\int_0^1 \left(\frac{\Delta p}{q}\right)_c d\zeta = k g(\sigma) \beta^2\tag{2.18}$$

By taking  $k$  as a constant, the cross-flow pressure distribution at various cross sections is assumed to be similar, scaled by the term  $g(\sigma)$ . For a circular cross section, the theoretical solution of reference 1 is  $k = 1.0$ . The problem is to find  $k$  for an elliptic cross section.

Schindel<sup>7</sup> has measured the normal force on a 2:1 elliptical cross-section body with a length ratio  $L/r_b = 9.9$ . Integration of Equation (2.18) along the whole elliptic body, both sides, for steady-state flow gives

$$Y_c = 2q \int_0^L \int_0^{r_b} \left(\frac{\Delta p}{q}\right)_c dz dx = 2qkr_b^2 \beta \int_0^{\beta\lambda} g(\sigma) d\sigma$$

or

$$C_{Y_c} = \frac{2}{\pi} k \beta \int_0^{\beta\lambda} g(\sigma) d\sigma \quad \text{for } t = \infty\tag{2.19}$$

The Schindel<sup>7</sup> data for  $\beta = 23.8^\circ$  (0.415 rad.),  $\lambda = 9.9$  are  $C_Y = 2.4$ . By definition

$$C_{Y_c} = C_Y - C_{Y_s}$$

$$= 2.4 - 2(0.415) = 1.57$$

and using either  $g_L$  or  $g_T$ , for this test condition

$$\int_0^{\beta\lambda} g(\sigma) d\sigma = 3.80$$

giving  $k = 1.57$ , which will be the value used for the TACV configuration.

This means the measured value of the non-slender-body component of the lateral force is 57 percent greater than indicated by the theory of Ruetenik and Brooks<sup>1</sup>. In view of the short length of this body (5 diameters), this difference is not particularly surprising. Figure 2.4 is taken from reference 1 where the sectional semi-side force  $\int_0^1 \frac{\Delta p}{q} d\zeta$  measured by Perkins and Jorgensen for a circular body with a 3-caliber ogive nose is plotted versus the axial station for an angle of attack of  $20^\circ$ . The Mach number is 1.98, but it can be considered to be low so far as cross-flow loads are concerned. The slender-body prediction is indicated by the dashed line. We are interested in the excess sectional force over the slender-body value for a body of about 10 radii length—the front half of this body. The theoretical prediction of reference 1 is indicated by the solid line. It is apparent that the measured sectional force exceeds the predicted value significantly in the region  $x/r_b$  from 4 to 12, and this explains the large value of  $k$ . For bodies of greater length,  $k$  would approach unity; in fact, for the complete body of Figure 2.4,  $k$  is 1.27.

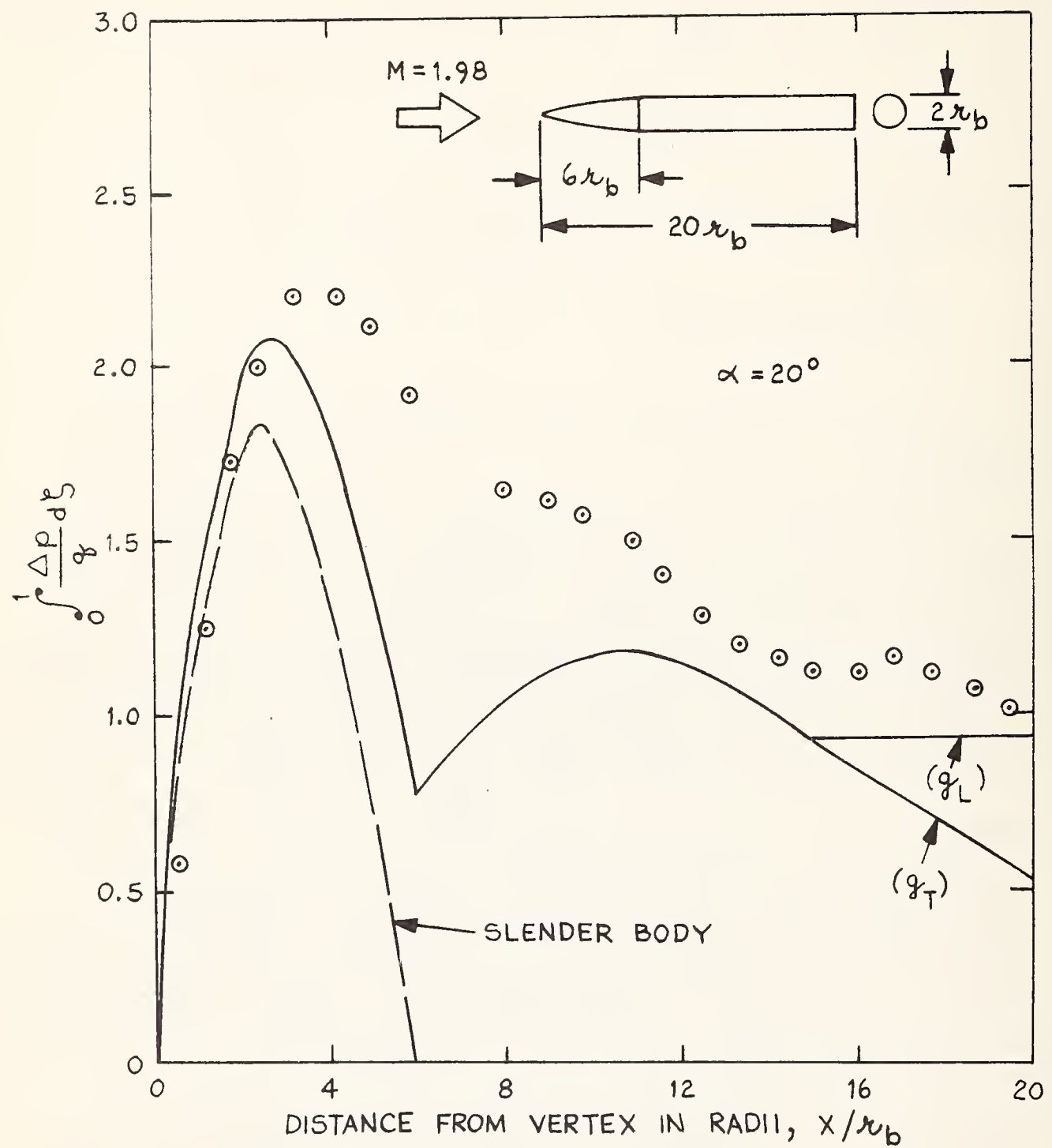


Fig. 2.4 Comparison of Steady-State Section Side Force Measured by Perkins and Jorgensen (NASA TN D-3716) and the Predicted Values of the Slender-Body Theory (Equation 2.9) and the Ruetenik-Brooks Theory (Equations 2.10 and 2.18).

The loads in this region of a body, where slender-body theory indicates a fall off along the axis, characteristically have been difficult to predict. At small angles of attack the loads do not fall off as fast as slender-body theory would indicate, and at large angles of attack methods that account for separation, such as that of reference 1 or the Allen theory<sup>8</sup>, do not increase fast enough along the axis to equal the measured loads. Theories have been developed accounting for body thickness to a higher order than slender-body theory for steady-state flow, but the transient loading cannot be determined. Consequently, all of the difference between the measured loading and the slender-body loading is attributed to the viscous cross flow.

Until the loading is better understood,  $k$  should be determined from measurements on bodies with as similar characteristics as possible. Therefore the present value, selected from the measurements on an elliptic-section body, applies most directly to a TACV configuration of a semi-elliptic or semi-circular section.

The next question concerns the application of  $k$  to the transient loading. In the transient situation, vortices develop within lamina already on the body in a fashion similar to the development of vortices within each lamina passing over the body in steady flow. This was the basis of the method developed in reference 1, and the assumption was confirmed by the comparisons made in reference 1. The  $k$  factor is applied, therefore, to the prediction of the transient loads.

The side-rail factor for the viscous cross flow is

$$r_{wc}(\gamma) = \int_{\gamma}^1 \bar{\zeta}(\zeta) d\zeta \quad (2.20)$$

From Perkins and Jorgensen<sup>3</sup> measurements on a body of revolution with a 3-caliber tangent-ogive nose, Figure 2.4,  $r_{wc}$  is evaluated. In this graph, the slender-body values and the value using  $k = 1$  are shown, the latter for both  $g_L$  and  $g_T$ . At the station  $x/r_b = 8.12$ ,  $k = 1.53$ --nearly equal the Schindel-data value. At this station the slender-body loading is zero, so  $\Delta p_c = \Delta p$ , therefore the loading data at this station and Equation (2.20) are used to determine  $r_{wc}(\gamma)$ , plotted in Figure 2.5.

The transient side-force and moment coefficients for a single body due to the viscous cross flow are:

$$\text{for } 0 \leq t \leq \frac{\lambda H_v}{V} ;$$

$$C_{Y_c} = \frac{2kr_{wc}(\gamma)\beta}{\pi} \left\{ \int_0^{\bar{t}} g(\sigma)d\sigma + g(\bar{t})[\beta\lambda - \bar{t}] \right\} \quad (2.21)$$

$$C_{n_c} = \frac{1}{2} C_{Y_c} - \frac{2kr_{wc}(\gamma)}{\pi\lambda} \left\{ \int_0^{\bar{t}} \sigma g(\sigma)d\sigma + g(\bar{t}) \left[ \frac{(\beta\lambda)^2}{2} - \frac{\bar{t}^2}{2} \right] \right\} \quad (2.22)$$

$$\text{for } t \geq \frac{\lambda H_v}{V} ;$$

$$C_{Y_c} = \frac{2kr_{wc}(\gamma)\beta}{\pi} \int_0^{\beta\lambda} g(\sigma)d\sigma \quad (2.23)$$

$$C_{n_c} = \frac{1}{2} C_{Y_c} - \frac{2kr_{wc}(\gamma)}{\pi\lambda} \int_0^{\beta\lambda} \sigma g(\sigma)d\sigma \quad (2.24)$$

where  $\bar{t}$  is defined  $\bar{t} = V\beta t/H_v$ .

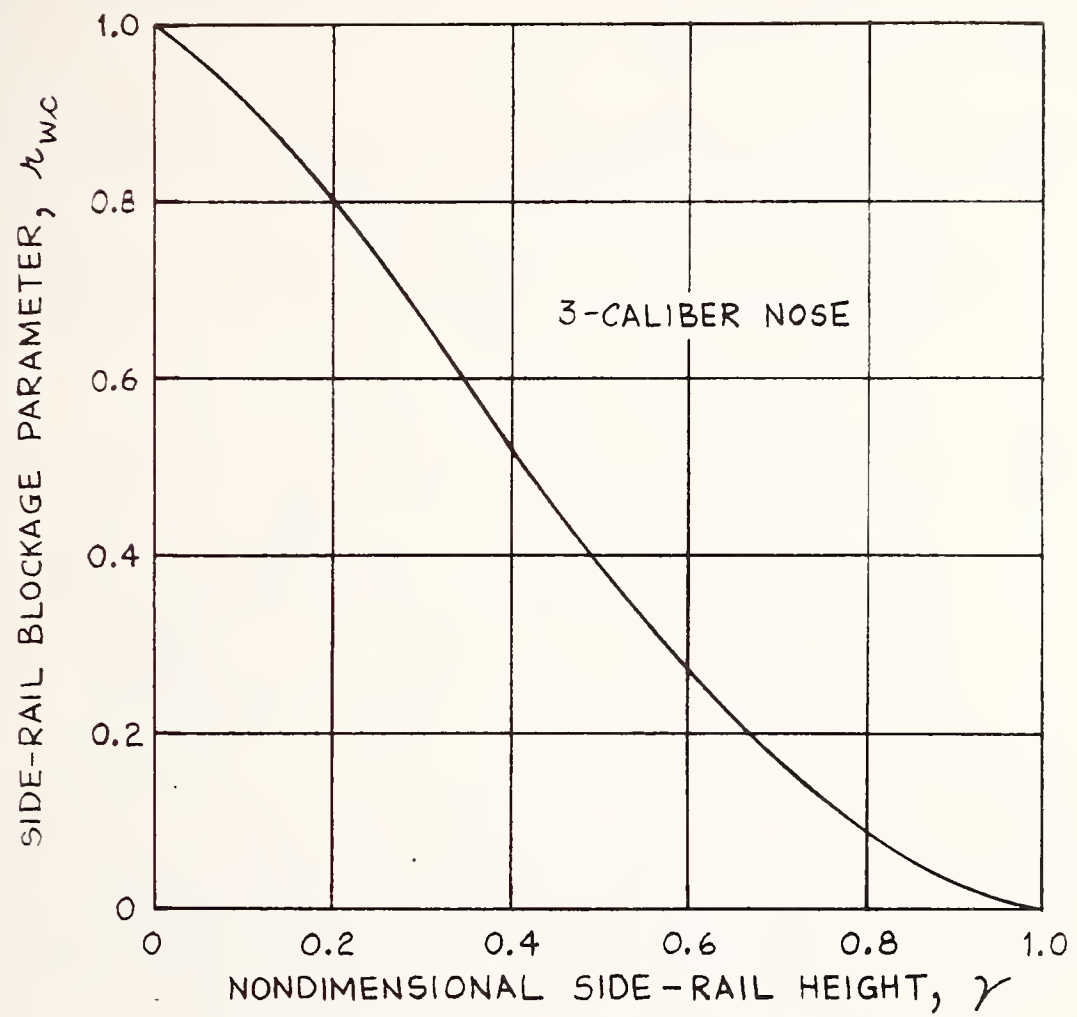


Fig. 2.5 Variation of Side-Rail Factor with Side-Rail Height for Viscous Cross-Flow. First Car.

### 2.3 RESULTS FOR FIRST CAR

A typical condition of interest is a TACV traveling 150 mph subject to a 60-mph gust, resulting in a sideslip angle of  $21.8^\circ$  or 0.38 radians and resultant Mach number of 0.209. Siderail heights of 0, 30 and 60 percent of the vehicle height are considered. The nose length is  $\lambda_1 = 2$ . The resulting integrals are

$\gamma$		$I_1$	$I_2$	$I_3$	$I_4$	$r_w$ ( $\varepsilon = 2$ )
0		0.500	1.571	0.333	1.808	1.0
0.3		0.249	0.998	0.209	1.230	0.711
0.6		0.080	0.452	0.088	0.627	0.409

and  $\bar{t} = 0.0794 \tau$ .

The curves for the transient side-force coefficient and yawing-moment coefficient are plotted in Figures 2.6 and 2.7. These apply to a single car or first car of a train.

The side force jumps to a very high value at time zero due to slender-body loads, but the duration of this peak is very short--about 0.035 sec for a 10-ft high vehicle--so the impulse probably is not critical. The side force increases again to a peak value, nearly equal the steady-state value, in 0.3 to 0.4 seconds for a 10-ft high vehicle.

The yawing moment first is large negatively, increases almost linearly to a positive peak in about 0.035 sec (10-foot high vehicle) and decreases to a small positive moment, generally, at about 0.3 to 0.6 seconds.

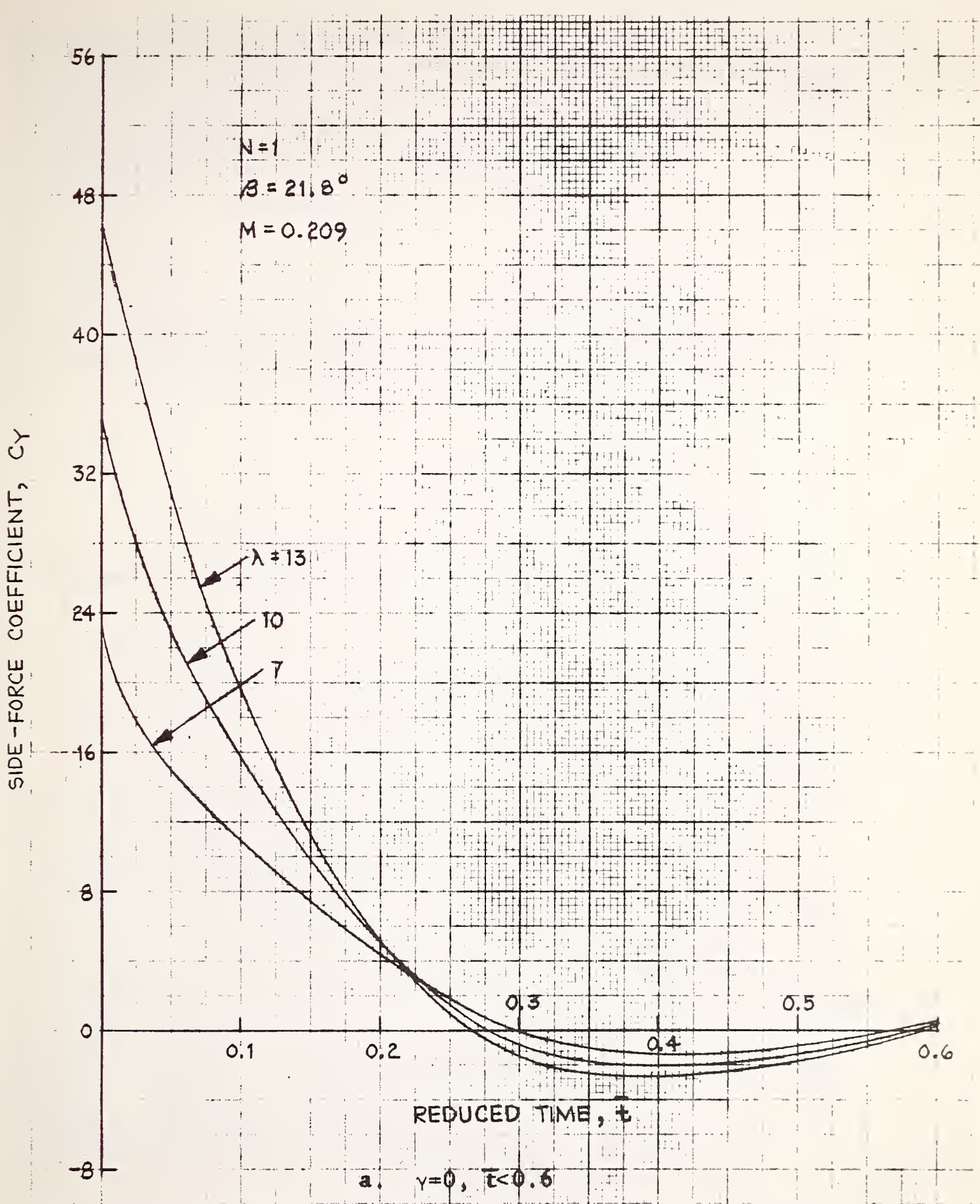


Fig. 2.6 Variation of Side-Force Coefficient with Reduced Time for Various Side-Rail Heights. First Car.

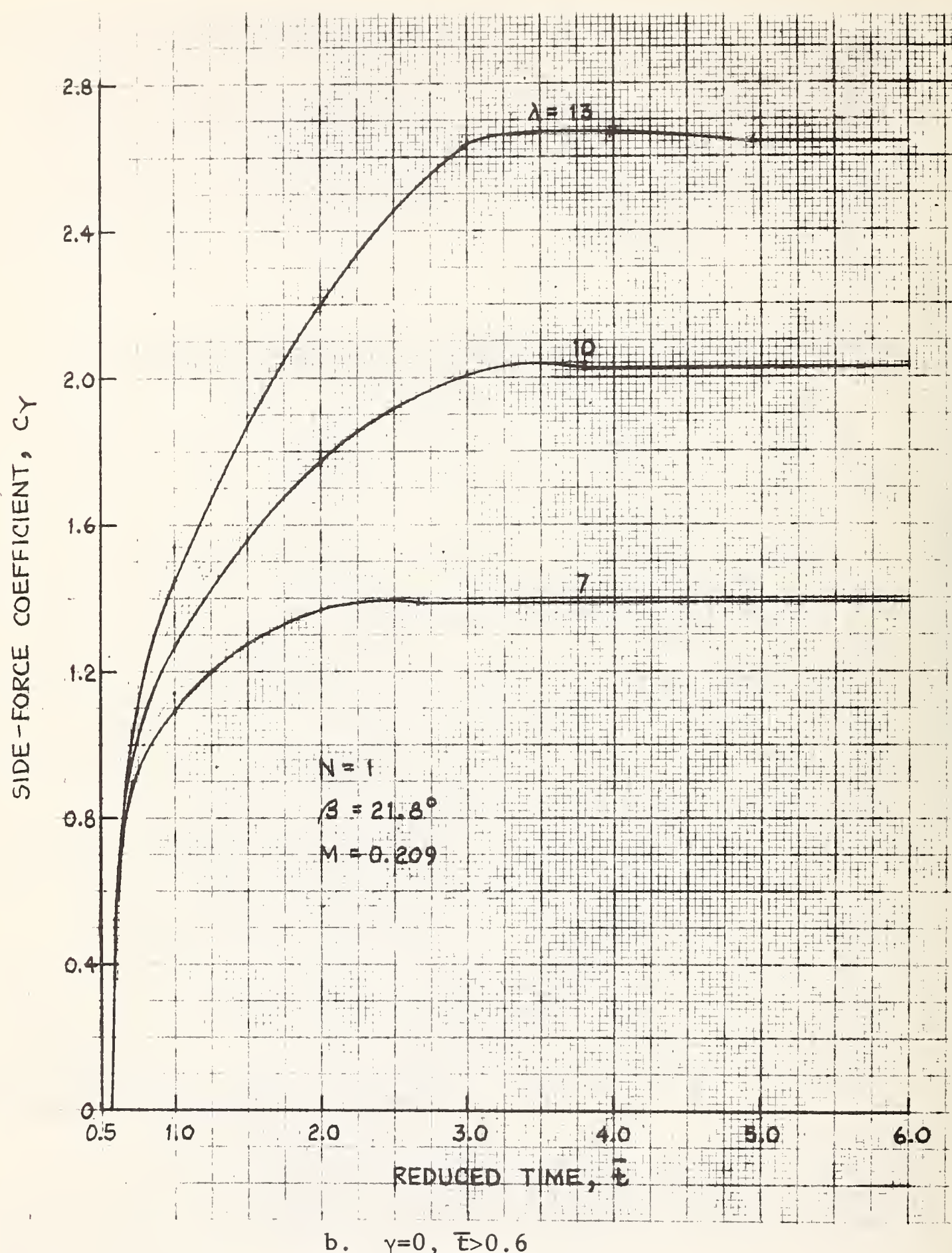


Fig. 2.6 (Continued)

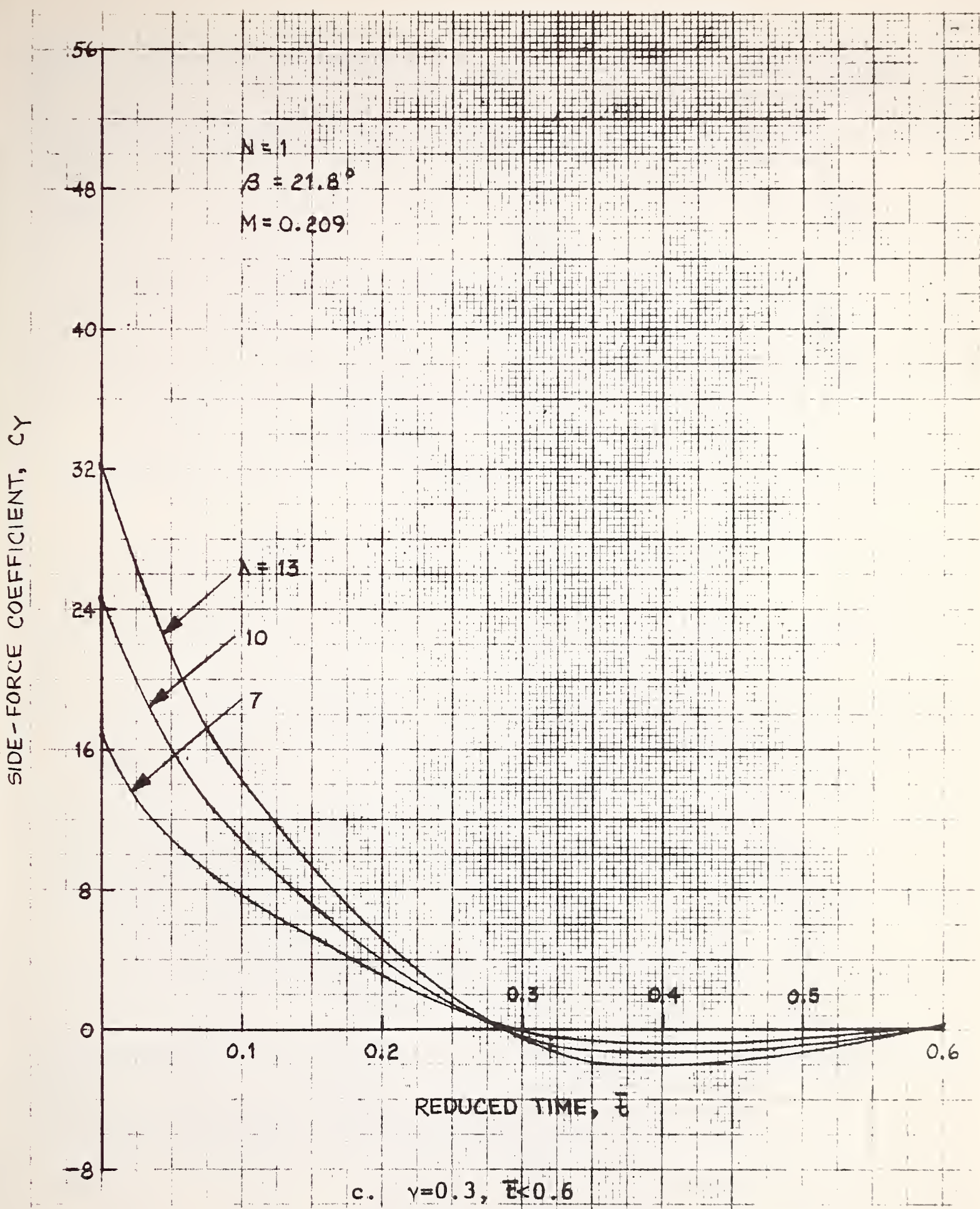


Fig. 2.6 (Continued)

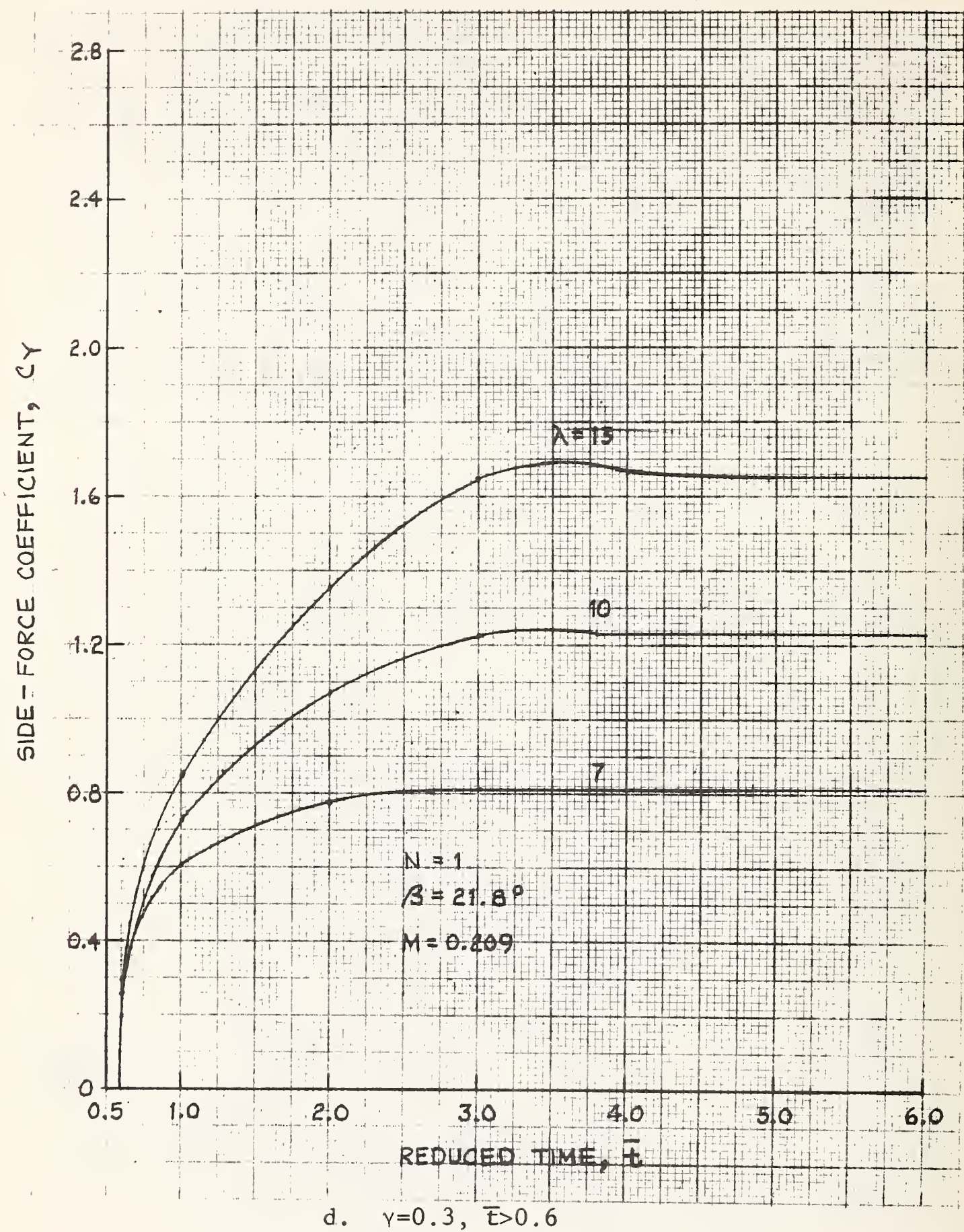


Fig. 2.6 (Continued)

SIDE-FORCE COEFFICIENT,  $C_Y$

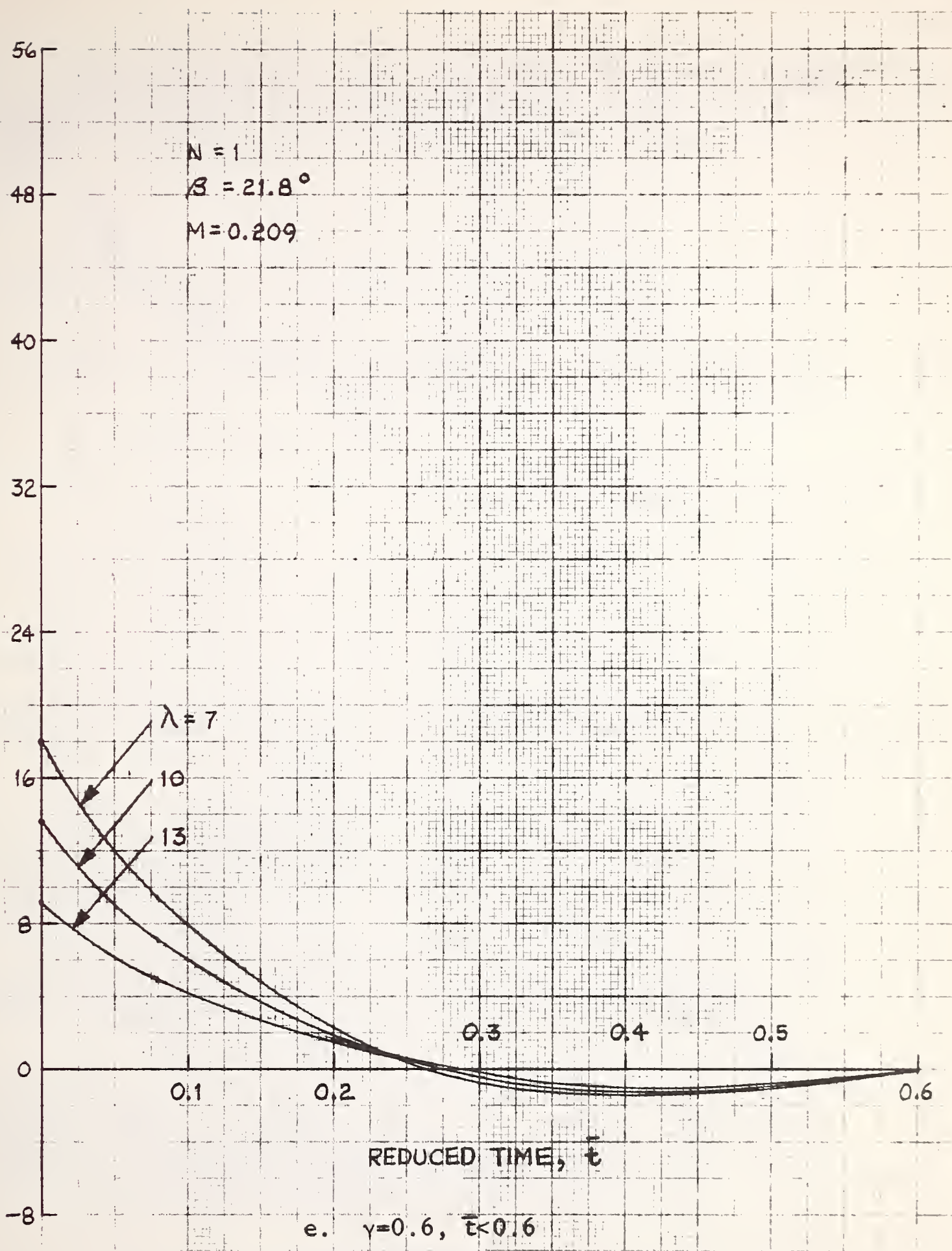


Fig. 2.6 (Continued)

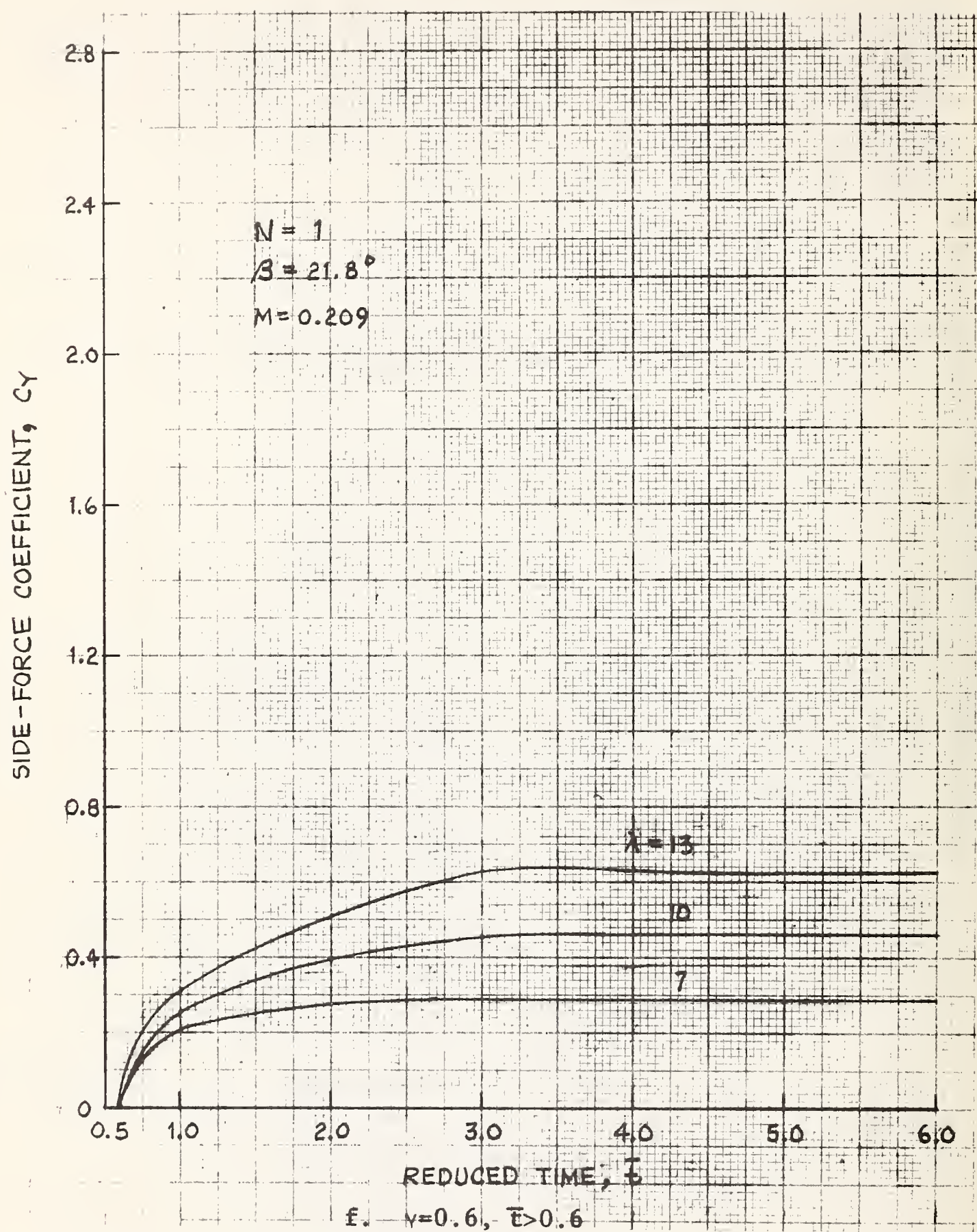


Fig. 2.6 (Concluded)

YAWING-MOMENT COEFFICIENT,  $C_n$

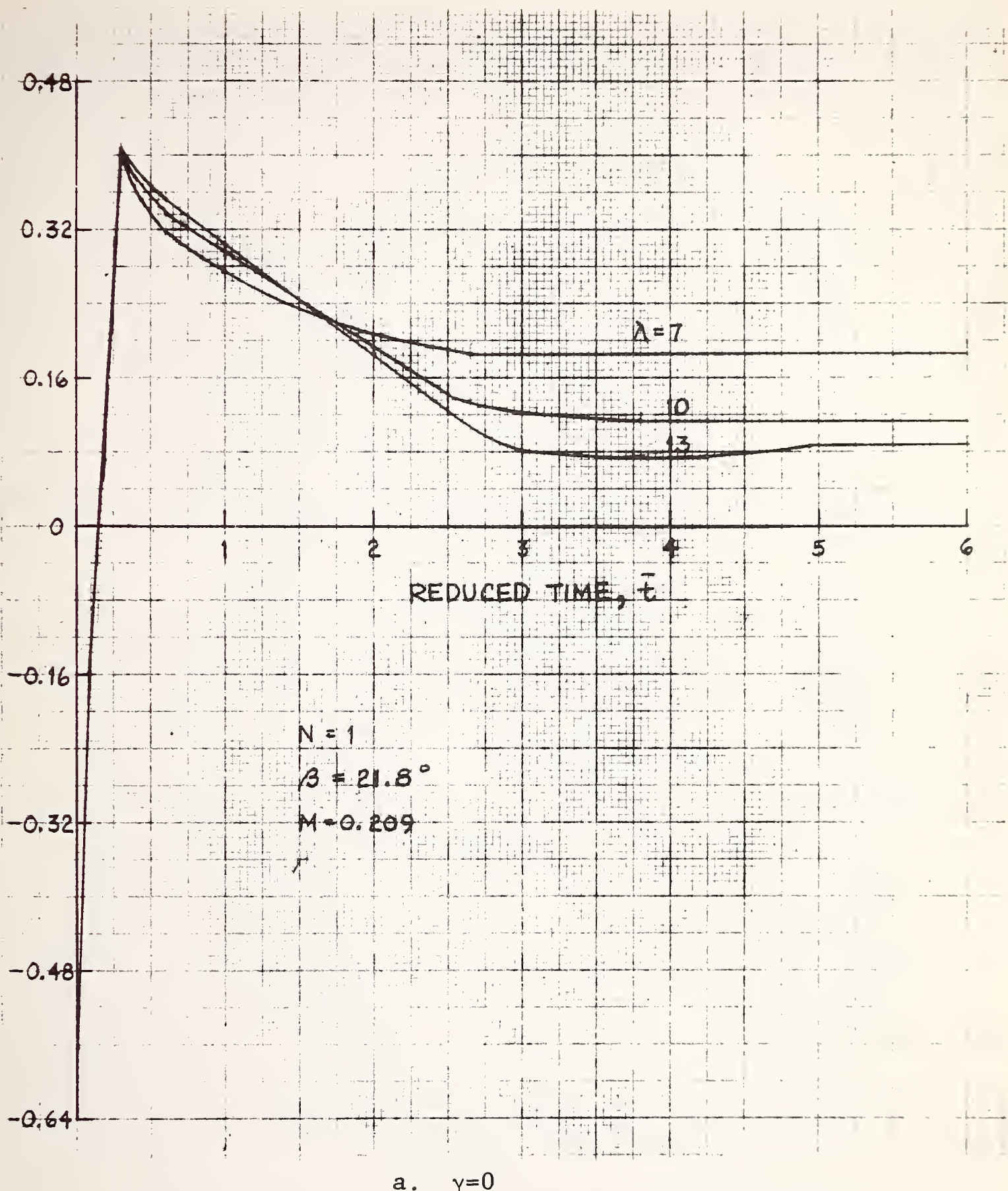


Fig. 2.7 Variation of Yawing-Moment Coefficient with Reduced Time for Various Side-Rail Heights. First Car.

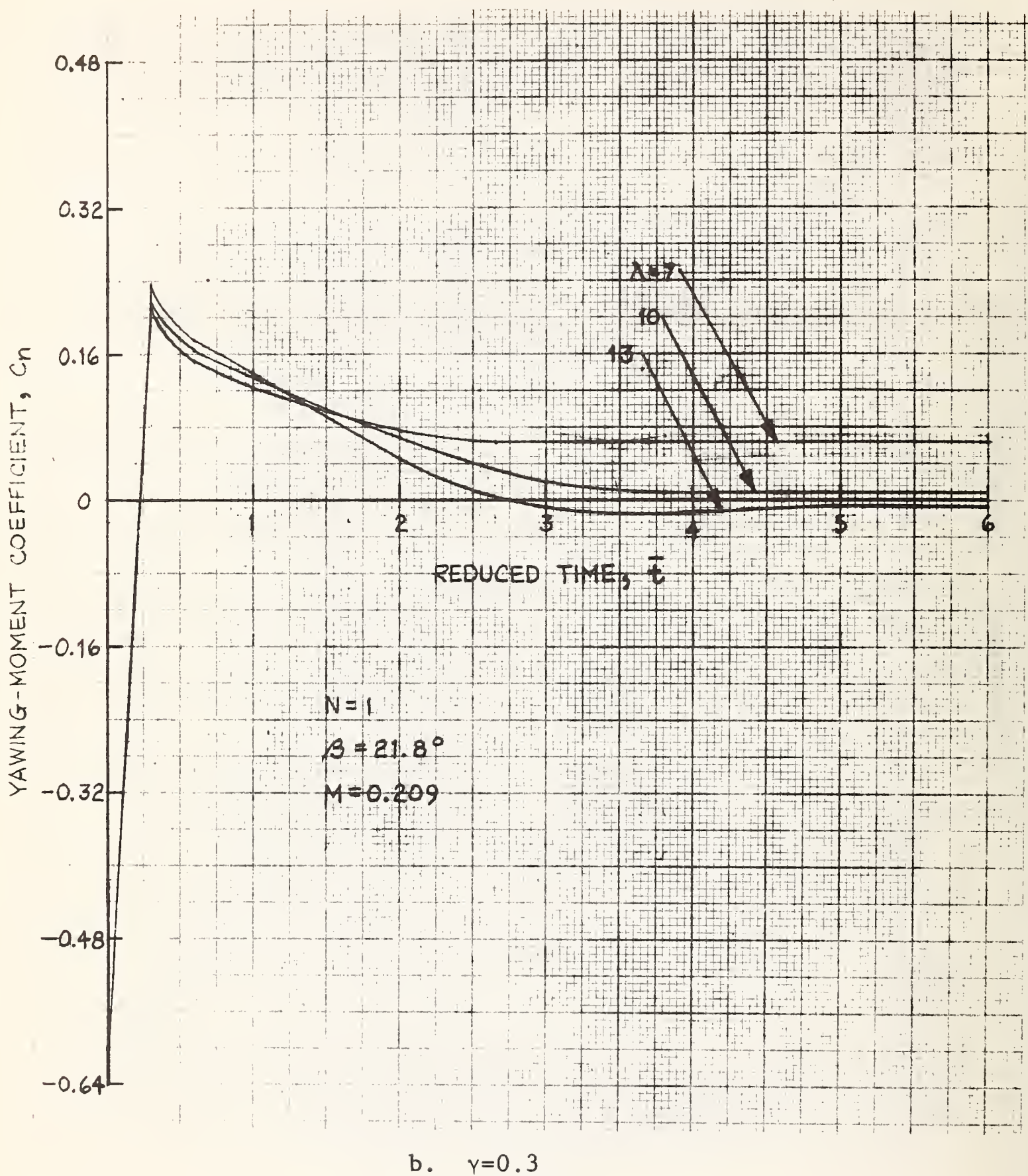


Fig. 2.7 (Continued)

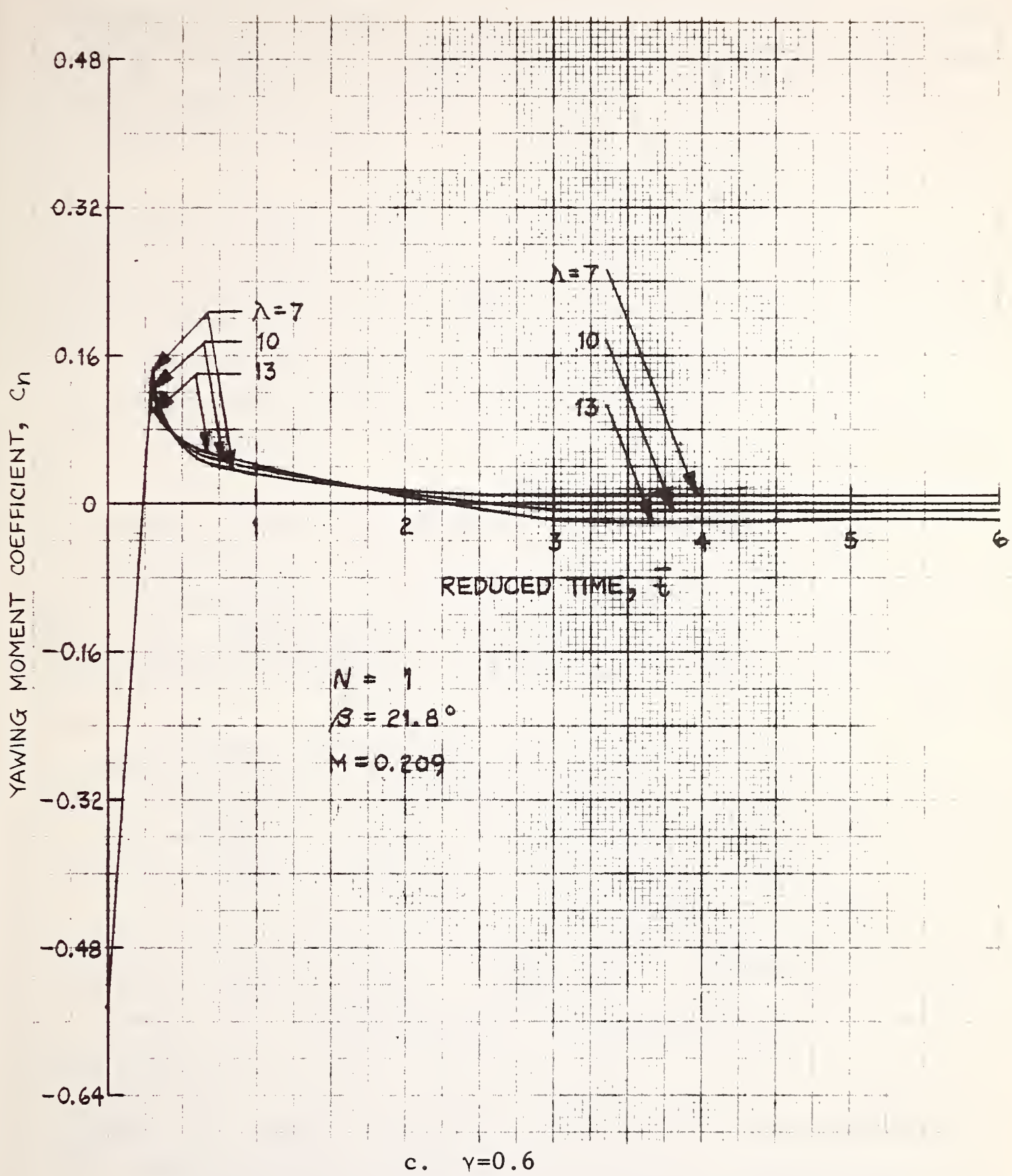


Fig. 2.7 (Concluded)

The side-rail effect on the steady-state  $C_Y$  for the first car, Figure 2.8, indicates that a height of 35 to 40 percent of  $H_v$  would be required to reduce  $C_Y$  by one half. Based on slender-body theory, Woolard<sup>10</sup> indicates a 23-percent side-rail height would cut  $C_Y$  in half for a similar body having a semi-elliptic cross section.

The side-rail effect on the steady-state  $C_n$  for the first car, Figure 2.9, indicates a drastic reduction in  $C_n$  with increasing height. In fact,  $C_n$  would tend to be stabilizing for the negative values associated with high side-rail heights. This marked effect of side-rail height on  $C_n$  reflects the greater sensitivity of the slender-body forces located at the forebody to wall height, whereas the less sensitive viscous forces predominate aft of the moment center.

The rapid buildup of the transient side force predicted by this method and the small overshoot beyond the steady-state value focus attention on the steady-state lateral wind forces for the first car. Therefore, we will examine some steady-state side-force and yawing-moment data measured in wind-tunnel tests.

Grunwald<sup>2</sup> measured steady-state forces and moments on the configurations shown in Figure 2.10 in wind-tunnel tests with a moving-belt ground plane. The measured  $C_Y$  values are plotted in Figure 2.11 as a function of the sideslip angle for a gap  $H$  between the models and the ground plane of  $0.05 d_e$ , where  $d_e$  is the diameter of a circle equivalent in area to the maximum cross section of the model. A moving belt was used for the ground plane to provide TACV simulation in a wind tunnel. The belt was aligned with the wind and moved with the wind speed. To examine the effect of the moving belt, Grunwald performed measurements both with the belt moving and stopped. The effect on the side force and yawing moment proved to be very small. The data from the tests with the moving belt are used here.

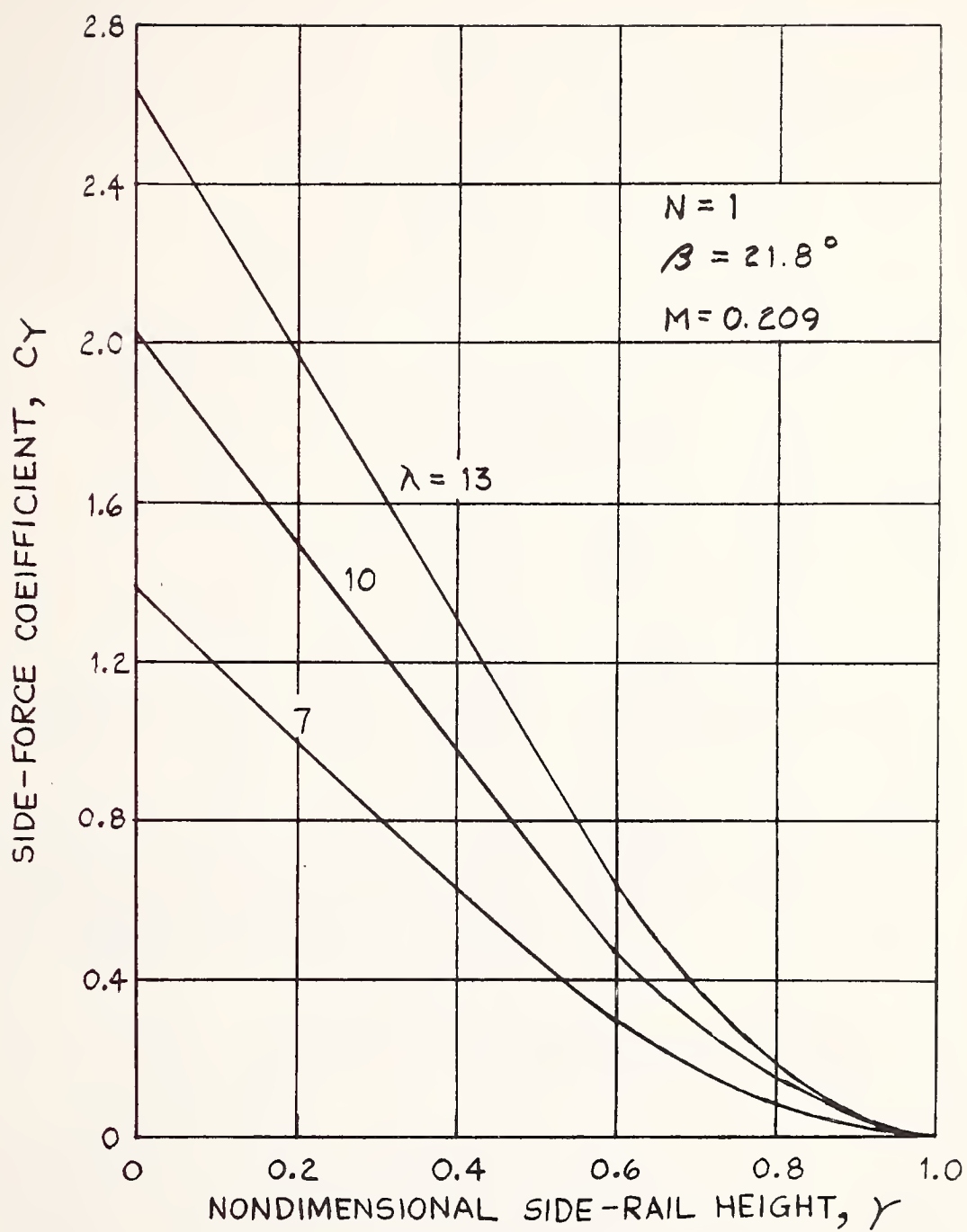


Fig. 2.8 Variation of Steady-State Side-Force Coefficient with Side-Rail Height. First Car, 3-Caliber Nose.

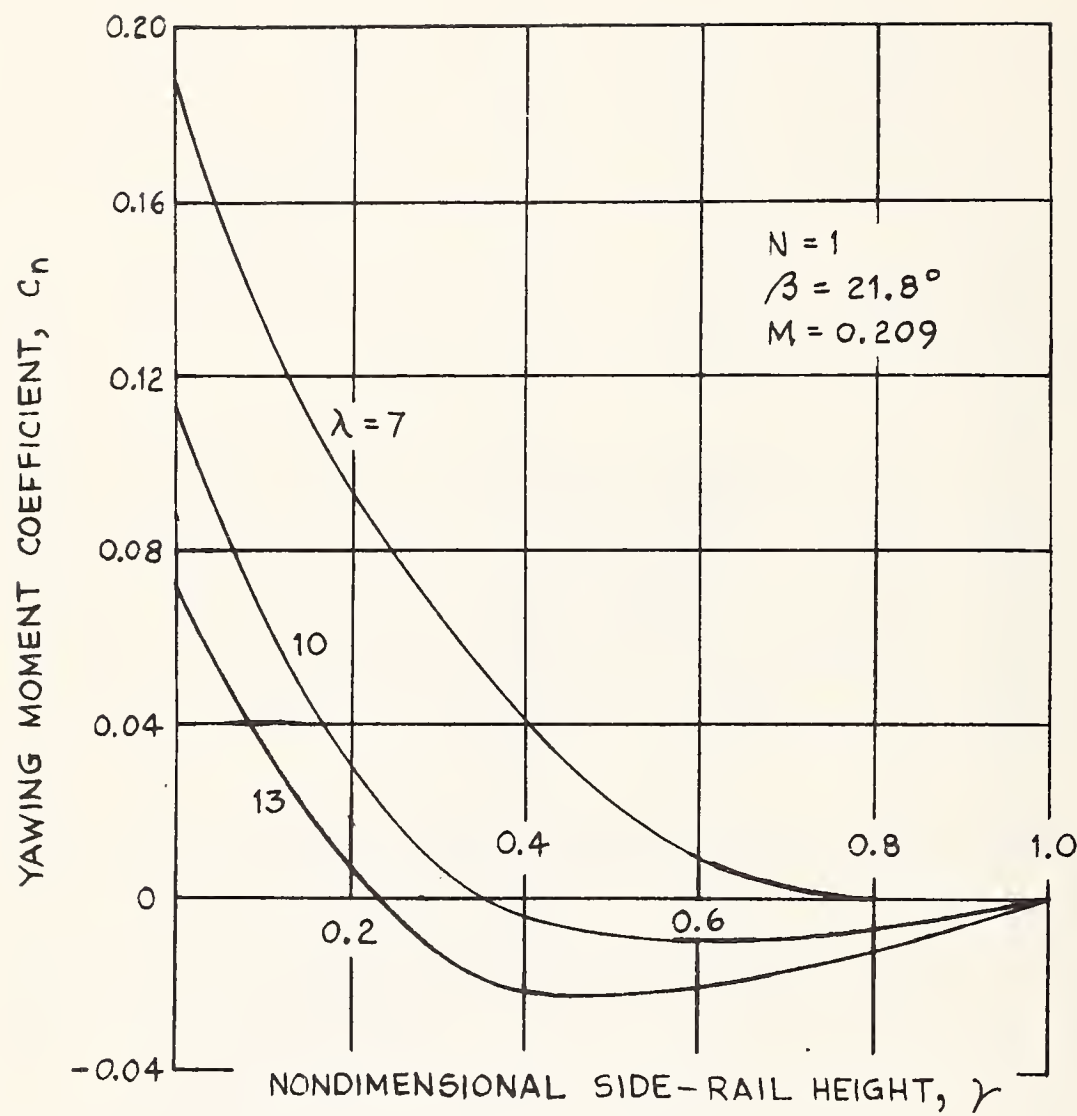


Fig. 2.9 Variation of Yawing-Moment Coefficient with Side-Rail Height. First Car, 3-Caliber Nose.

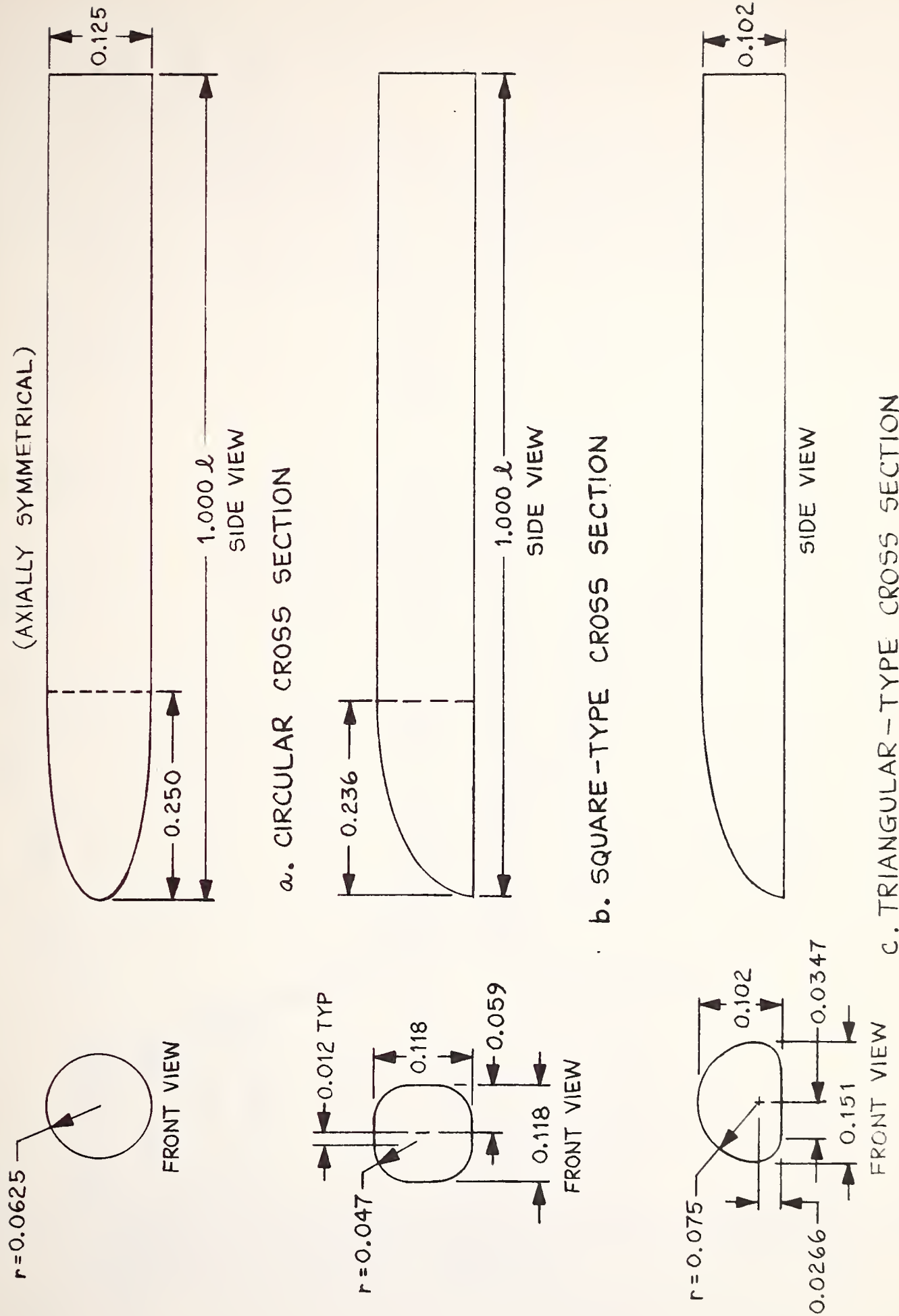
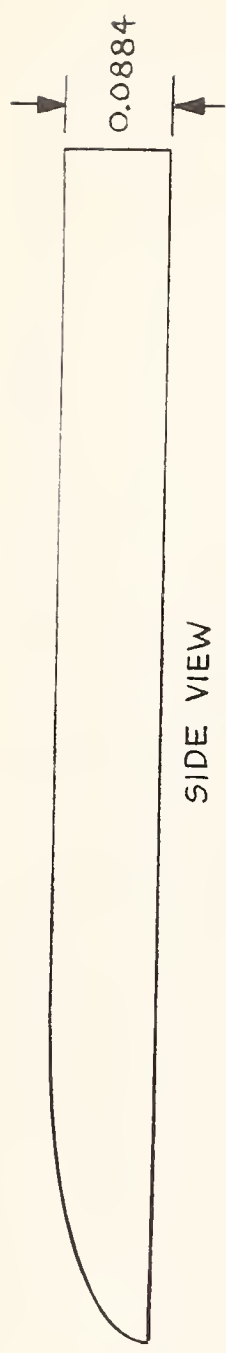
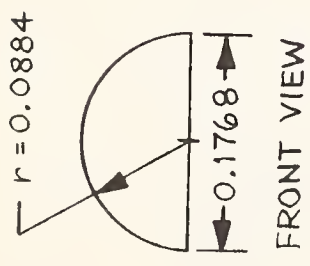
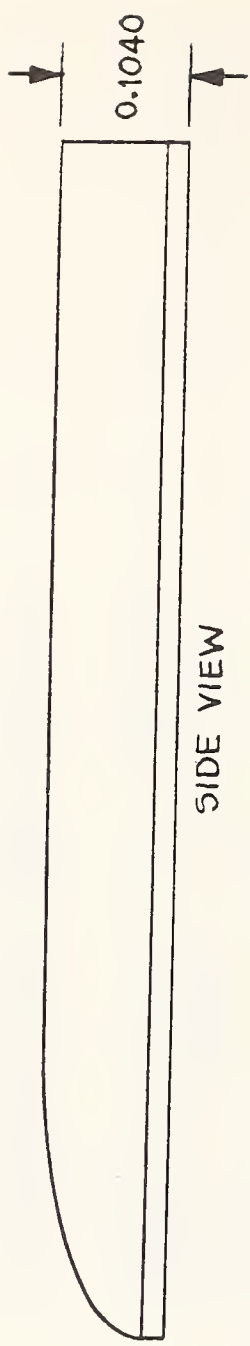
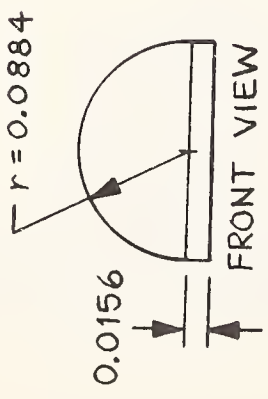


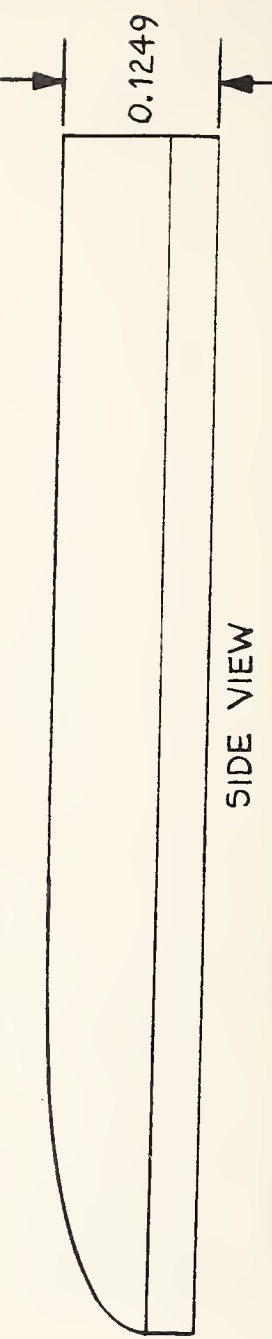
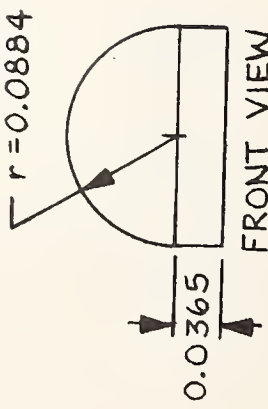
Fig. 2.10 Drawing of Vehicle Configurations Tested by Grunwald (NASA TN D-5935). All Noses Elliptical. Dimensions Based on Vehicle Length.



d. HALF-CIRCLE CROSS SECTION



e. HALF-CIRCLE (SHORT SIDES) CROSS SECTION



f. HALF-CIRCLE (LONG SIDES) CROSS SECTION

Fig. 2.10 (concluded)

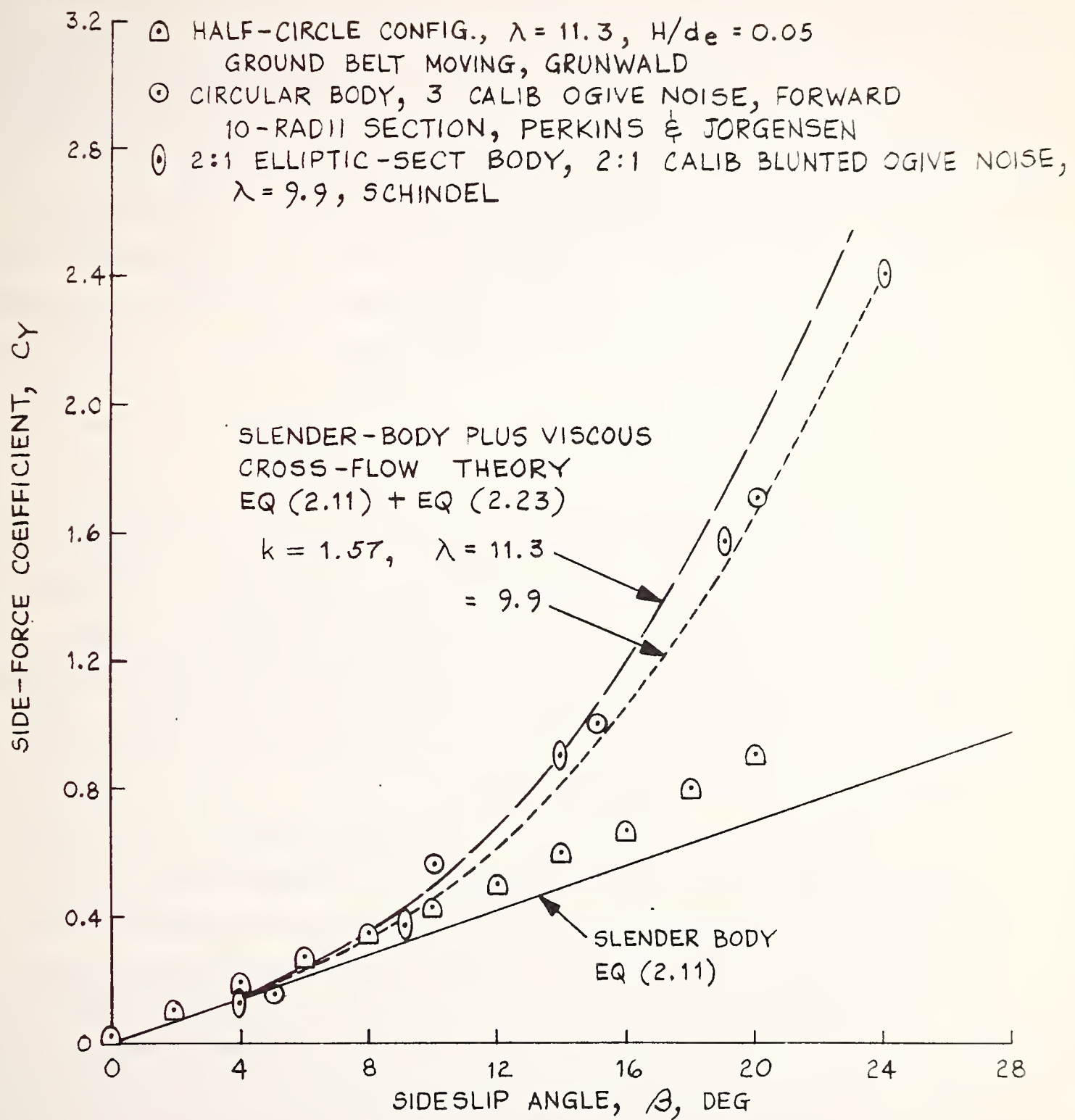


Fig. 2.11 Comparison of Predicted Side-Force Coefficient with Values Measured in Three Wind-Tunnel Tests over a Range of Sideslip Angles.

The predicted lateral force coefficient is plotted in Figure 2.11 for  $\beta = 20^\circ$ . It is greater than the value measured by Grunwald by a factor of 2.13.

For comparison, the slender-body value for  $C_y$  is also plotted in Figure 2.11, along with the values measured by Perkins and Jorgensen<sup>3</sup> and Schindel<sup>7</sup>. For the half-circle configuration measured by Grunwald, the force coefficient at  $20^\circ$  is only 1.30 times the slender-body value; the predicted value is 2.77 times the slender-body value. For the 2:1-elliptic-section body, 9.9 major-semi-axis lengths long, the side-force coefficient measured by Schindel<sup>7</sup> is 2.35 times the slender-body value. For the circular configuration at  $\beta = 20^\circ$ , Perkins and Jorgensen<sup>3</sup> measured a side-force for the first 10-radii length of the body of 1.9 times the slender-body value. Why the values measured by Grunwald are so near the slender-body value is not readily explained. The most obvious factor, of course, is the ground plane. Drag measurements by Roshko<sup>9</sup> on a body with a splitter plane in the wake demonstrate that such an obstruction can markedly reduce the drag force. The Roshko measurements indicate the plate inhibits the development of the wake vortices. The ground plane could have a similar effect on vortex growth on the lee side of TACV configurations.

Some questions remain unanswered, however, regarding the ground-plane simulation achieved in the wind-tunnel tests. For correct simulation of the relative wind to the ground and a TACV, the belt should move in the direction of the TACV-model axis. This was not feasible in the wind-tunnel tests, where the belt moved in the direction of the tunnel air flow. It is hoped that the importance of ground-plane simulation could be assessed by comparing the forces and moments with the belt moving and with it stopped. Unfortunately, compensating effects occur in these tests (the moving belt may improve the pressure recovery on the lee side, reducing the side force, and the stopped belt may cause separation on the windward side, also reducing the side force), so a definite conclusion cannot be reached.

These speculations are highly problematical without the aid of further measurements. In addition, pressure measurements on the vehicle would be very helpful in evaluating the simulation. The bottom gap and upper body configuration are expected to be important factors to the loading which should be examined.

To indicate the effect of gap height and external configuration on the side force coefficient, data of Grunwald<sup>2</sup> for  $\beta = 20^\circ$  for the 6 configurations are plotted in Figure 2.12 as a function of nondimensional gap height. The side-force coefficient  $\bar{C}_Y$  for this plot is based on the base area,  $A$ ,

$$\bar{C}_Y = \frac{Y}{qA} \quad (2.25)$$

The variation in  $\bar{C}_Y$  with  $H/d_e$  for the configurations falls into two groups: sensitivity to gap height, which includes the circular and square-type, and insensitivity to gap height, which includes the half circle and half circle (long sides). The triangular type falls in between, and for the half circle (short sides) there are insufficient data. The configurations with rounded bottoms appear to have the greatest sensitivity to gap height, whereas the flat-bottomed configurations are nearly insensitive. Furthermore, at the lowest values of  $H/d_e$ ,  $\bar{C}_Y$  for the gap-sensitive configurations is double that for the gap-insensitive configurations; this is about the ratio of the  $C_y$  values in Figure 2.11. From these results it is concluded that gap height and external configuration, particularly the bottom surface, are important, and interacting, factors for the side force where no side rail is present.

Measurements by Grunwald<sup>2</sup> of the rolling moment about the intersection of the model centerline and its base show the rolling-moment coefficient at large angles of sideslip follows the pattern for body configuration in the same way. The values are the largest (moment positive for body rolling away from

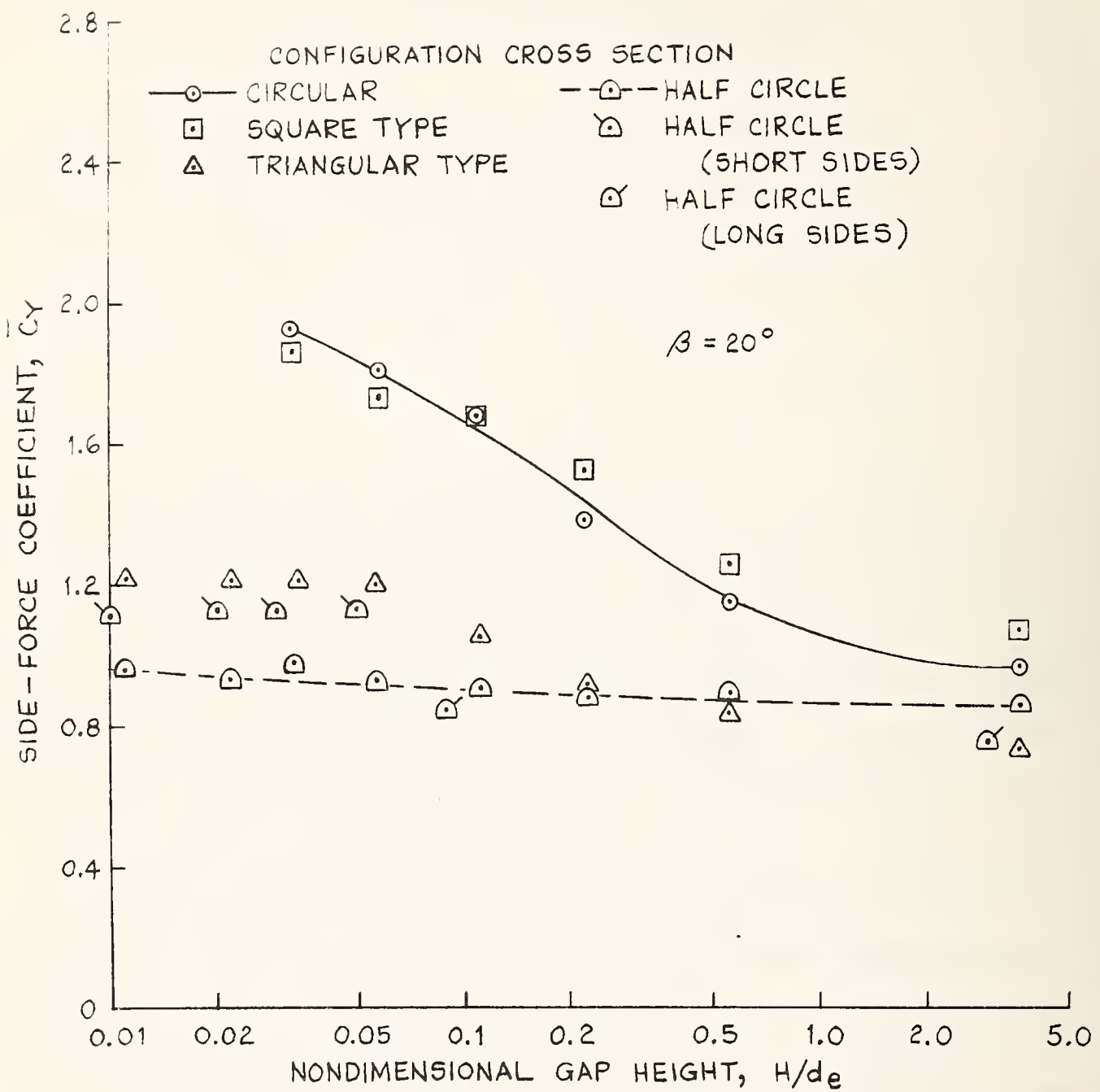


Fig. 2.12 Comparison of Side-Force Coefficient Measured by Grunwald (NASA TN D-5935) for Six Configurations as a Function of Gap Height above Ground Plane.  $\beta=20^\circ$ .

side wind) for the circular and square-type configurations, nearly zero or negative for the half circle configurations, and midway between for the triangular-type configuration. For the largest gap, the rolling-moment coefficient for the half circle is nearly as large negatively as it is positive for the circular configuration. As the gap is reduced, the spread in the values nearly doubles and becomes more positive.

Examination of the side-force, rolling-moment and lift coefficients would indicate that the flow probably always separates from the bottom surface of the flat-bottom bodies, giving a more uniform pressure on the bottom surface. On bottom surfaces with curved edges, the separation point is believed to be sensitive to the gap height, moving windward as the gap is reduced; the lee pressure is sensitive to this separation point, thereby, perhaps, affecting the separation point on the upper surface and thereby the side force and rolling moment.

It is concluded the shape of the gap is an important factor to the side force and rolling moment, where no side rail is present. Side rails are expected to reduce the side force, both by shielding and also by separation of the flow in the gap at the top of the gap on the windward side, the side gaps being an extension of the bottom gap, of the flat-bottom type. The situation is complicated, of course, by the ram effect at the nose of the body and levitation air from the air cushion.

## 2.4 EQUATIONS FOR $N^{\text{th}}$ CAR

The equations for the transient side force and yawing moment for a single car or the first car of a TACV train are developed in Section 2.2. The equations for the  $N^{\text{th}}$  car in a TACV train are presented in this section. The  $N^{\text{th}}$ -car equations apply to all cars except the first car.

The side-force coefficient,  $C_Y$ , and yawing-moment coefficient,  $C_n$ , are defined the same as for the first car, which are given by Equations (2.2) and (2.3). The yawing moment is defined about the mid-point of the car, as shown in Fig. 2.1 for the first car.

The forebody coefficients are assumed to be zero for all cars but the first, even though the forebody shape may be the same for these cars as for the first car, so:

for  $N > 1$ ;

$$C_{Y_f} = C_{n_f} = 0 \quad (2.26)$$

$$C_Y = C_{Y_{as}} + C_{Y_c} \quad (2.27)$$

$$C_n = C_{n_{as}} + C_{n_c} \quad (2.28)$$

The coefficients  $C_{Y_{as}}$  and  $C_{n_{as}}$  are computed from Equations (2.12) and (2.14). The equations for  $C_{Y_c}$  and  $C_{n_c}$  have been developed in the same way as Equations (2.21) to (2.24) for the first car. The resulting equations for  $N > 1$  are:

for  $0 \leq \bar{\epsilon} \leq (N - 1)\lambda\beta$ ;

$$C_{Y_c} = \frac{2}{\pi} kr_{wc}(\gamma)\lambda\beta^2 g(\bar{\epsilon}) \quad (2.29)$$

$$C_{n_c} = 0 \quad (2.30)$$

for  $(N - 1)\lambda\beta \leq \bar{\epsilon} \leq N\lambda\beta$ ;

$$C_{Y_c} = \frac{2}{\pi} kr_{wc}(\gamma)\beta \left[ \int_{\beta(N-1)\lambda}^{\bar{\epsilon}} g(\sigma)d\sigma + (N\lambda\beta - \bar{\epsilon})g(\bar{\epsilon}) \right] \quad (2.31)$$

$$C_{n_c} = \frac{2N - 1}{2} C_{Y_c} - \frac{2kr_{wc}(\gamma)}{\pi\lambda} \left\{ \int_{(N-1)\lambda\beta}^{\bar{\tau}} \sigma g(\sigma) d\sigma + \frac{1}{2} [ (N\lambda\beta)^2 - \bar{\tau}^2 ] g(\bar{\tau}) \right\} \quad (2.32)$$

for  $N\lambda\beta \leq \bar{\tau}$ ;

$$C_{Y_c} = \frac{2}{\pi} kr_{wc}(\gamma)\beta \int_{(N-1)\lambda\beta}^{N\lambda\beta} g(\sigma) d\sigma \quad (2.33)$$

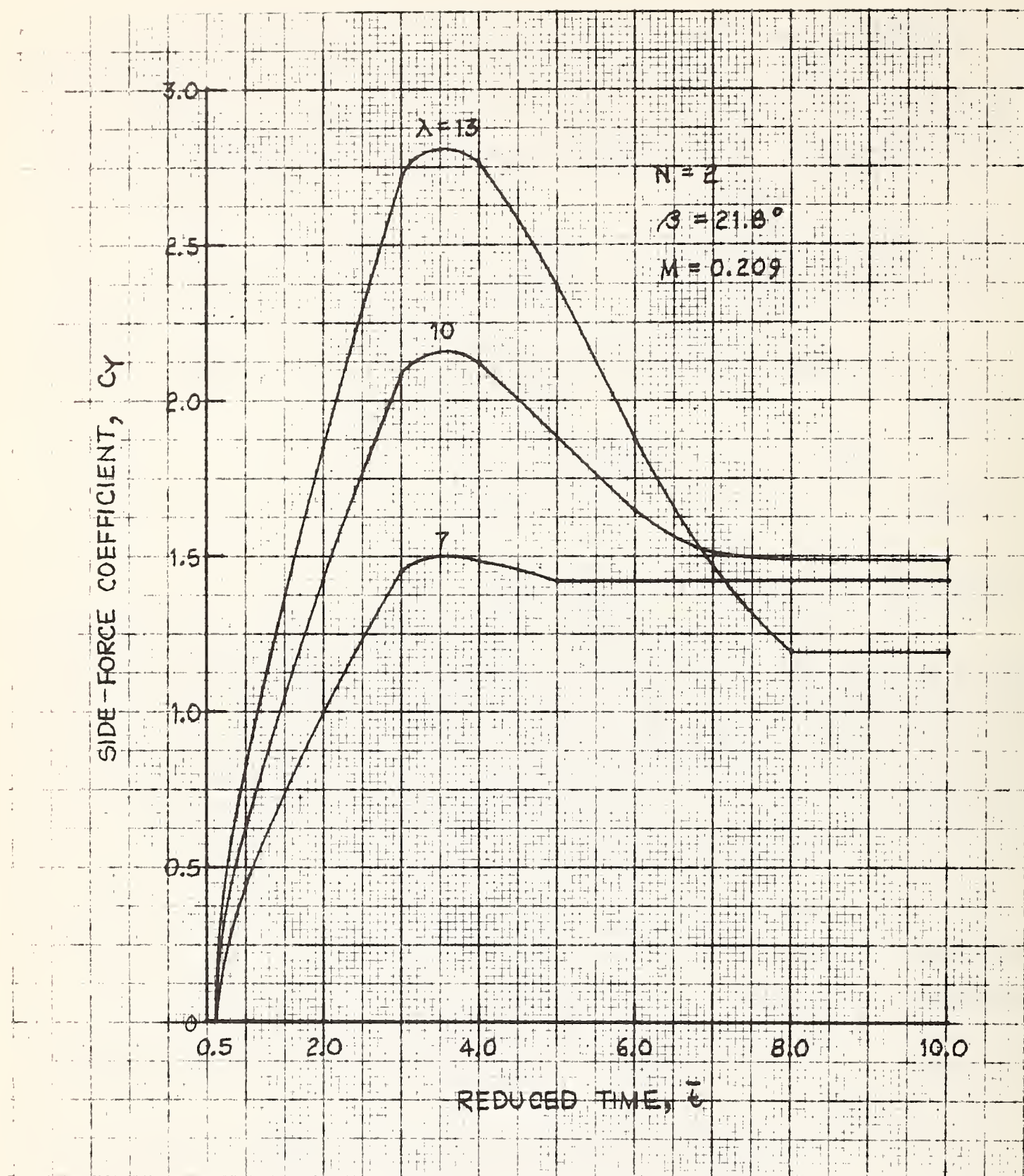
$$C_{n_c} = \frac{2N - 1}{2} C_{Y_c} - \frac{2kr_{wc}(\gamma)}{\pi\lambda} \int_{(N-1)\lambda\beta}^{N\lambda\beta} \sigma g(\sigma) d\sigma \quad (2.34)$$

## 2.5 RESULTS FOR SECOND AND THIRD CAR

The transient side-force and yawing-moment coefficients for the second and third car of a TACV train were computed using the equations of Section 2.4. The results are presented in Fig. 2.13 to 2.16 for three side-rail heights,  $\gamma$ , of 0, 30 and 60 percent of the maximum vehicle height,  $H_v$ . The sideslip angle  $\beta = 21.8^\circ$  and the Mach number  $M = 0.209$  are the same as for the first-car calculations of Fig. 2.6 and 2.7.

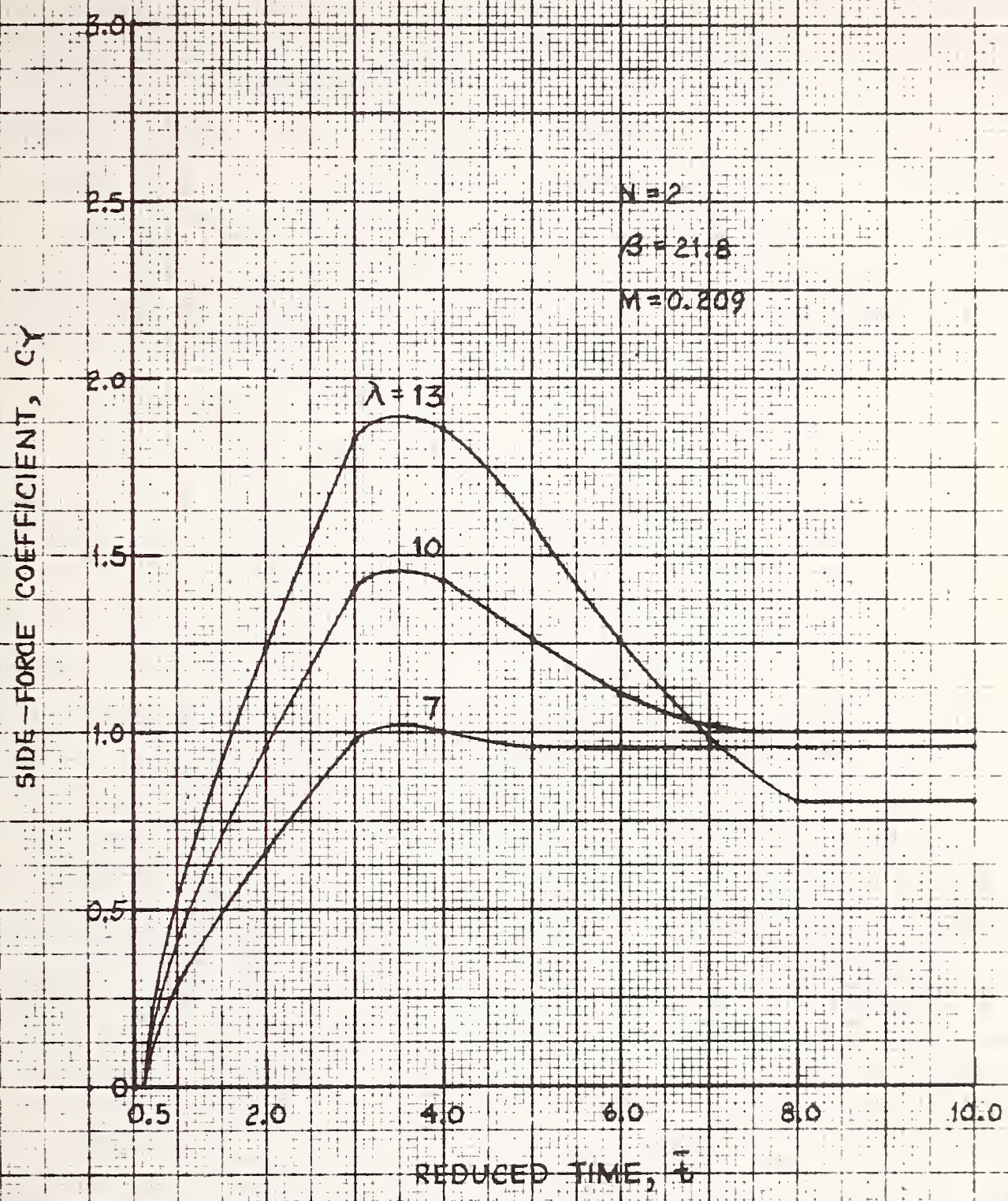
The side force has a very short duration spike that decreases to zero in  $\bar{\tau} < 0.3$ . This force is due to the slender-body non-viscous part of the loading. The impulse due to this early peak is expected to not be critical, as for the first car, Section 2.3, so this portion of the loading history is not shown in these figures.

The side-force coefficient reaches a second peak at about  $\bar{\tau} = 3.5$ . The side force then decreases to reach a steady-state value at about  $\bar{\tau} = 5$  for the second car if  $\lambda = 7$  and  $\bar{\tau} = 8$  for all other cases. The ratio of the peak side force to the steady-state side force ranges from 1.1 to 2.4 for the second car and from 2.0 to 4.3 for the third car.



$$a. \quad \gamma = 0$$

Fig. 2.13 Variation of Side-Force Coefficient With Reduced Time for Various Side-Rail Heights. Second Car.



b.  $\gamma = 0.3$

Fig. 2.13 (Continued)

SIDE-FORCE COEFFICIENT,  $C_Y$

3.0

2.5

2.0

1.5

1.0

0.5

0

$N = 2$

$\beta = 21.8^\circ$

$M = 0.209$

$\lambda = 13$

10

7

4

2

1

0.5 2.0

4.0

6.0

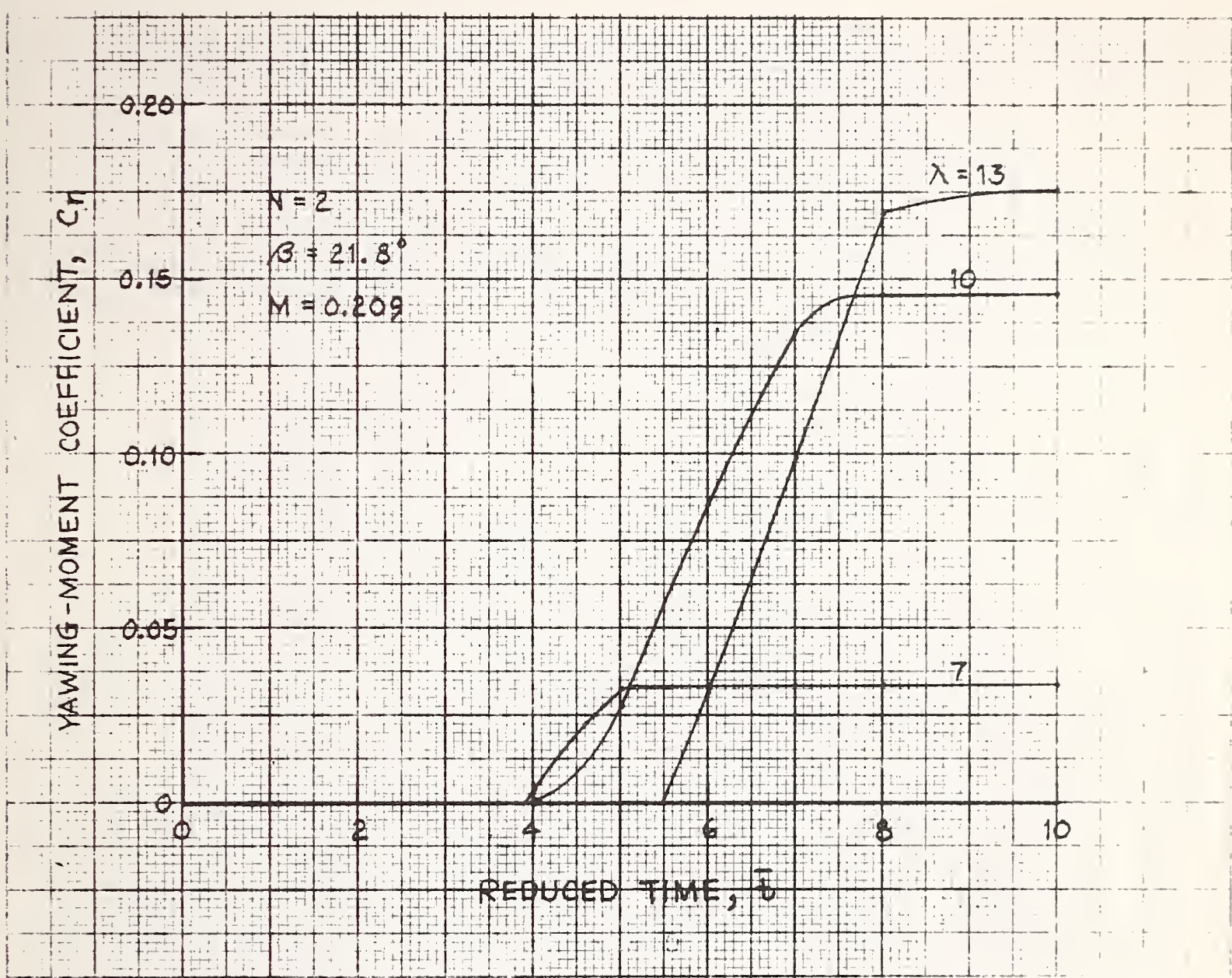
8.0

10.0

REDUCED TIME,  $t$

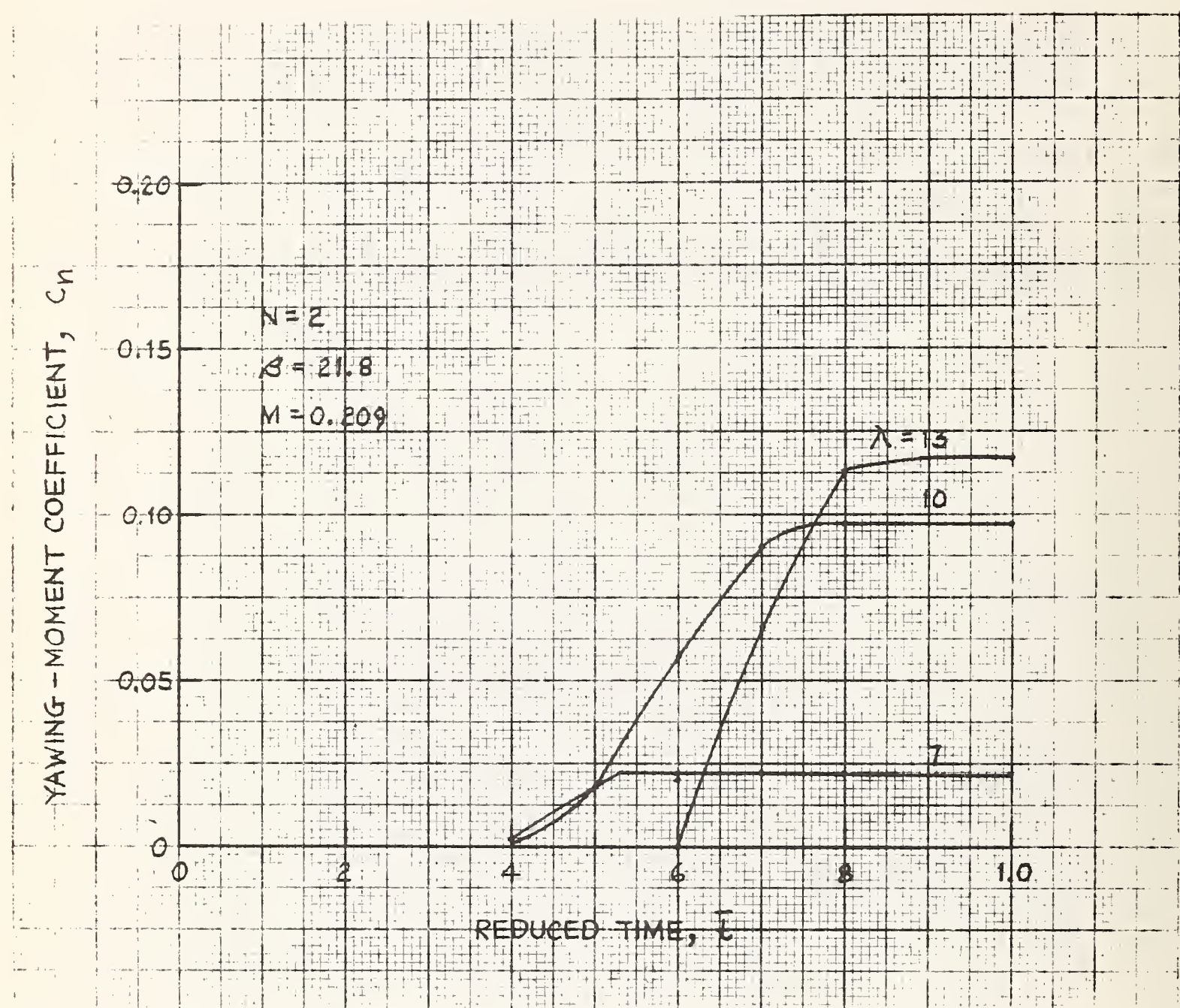
c.  $\gamma = 0.6$

Fig. 2.13 (Concluded)



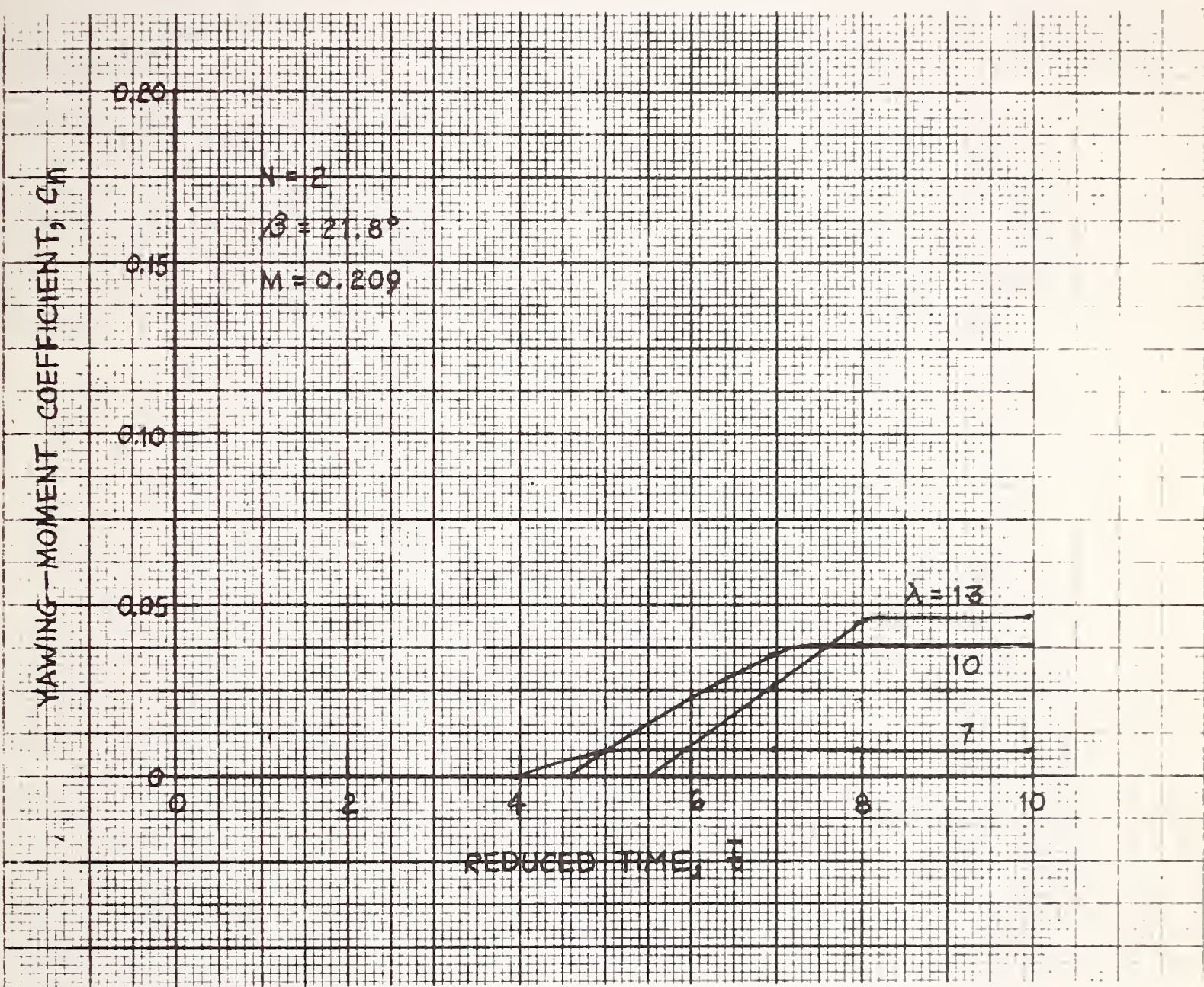
a.  $\gamma = 0$

Fig. 2.14 Variation of Yawing-Moment Coefficient With Reduced Time for Various Side-Rail Heights. Second Car.



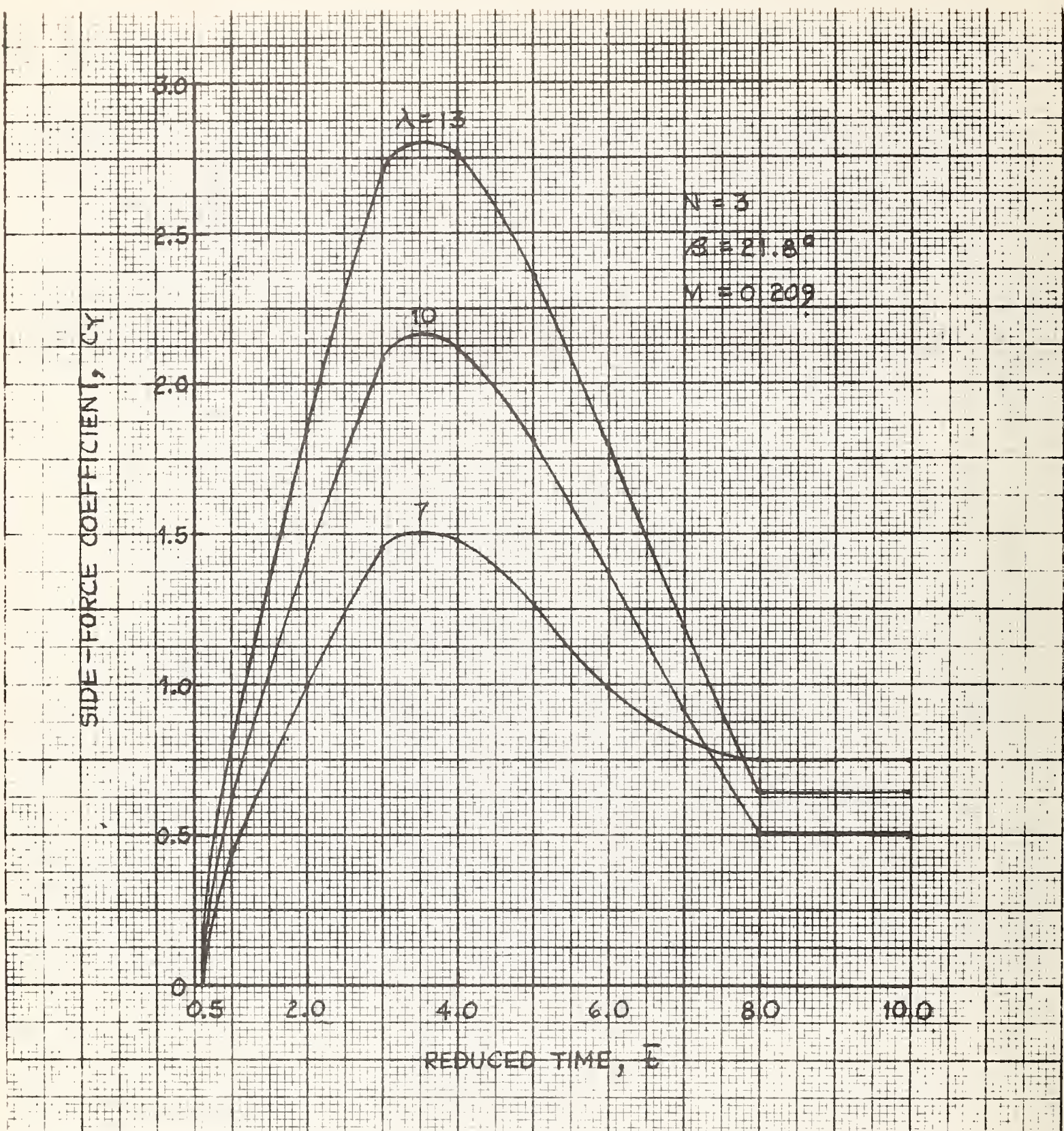
b.  $\gamma = 0.3$

Fig. 2.14 (Continued)



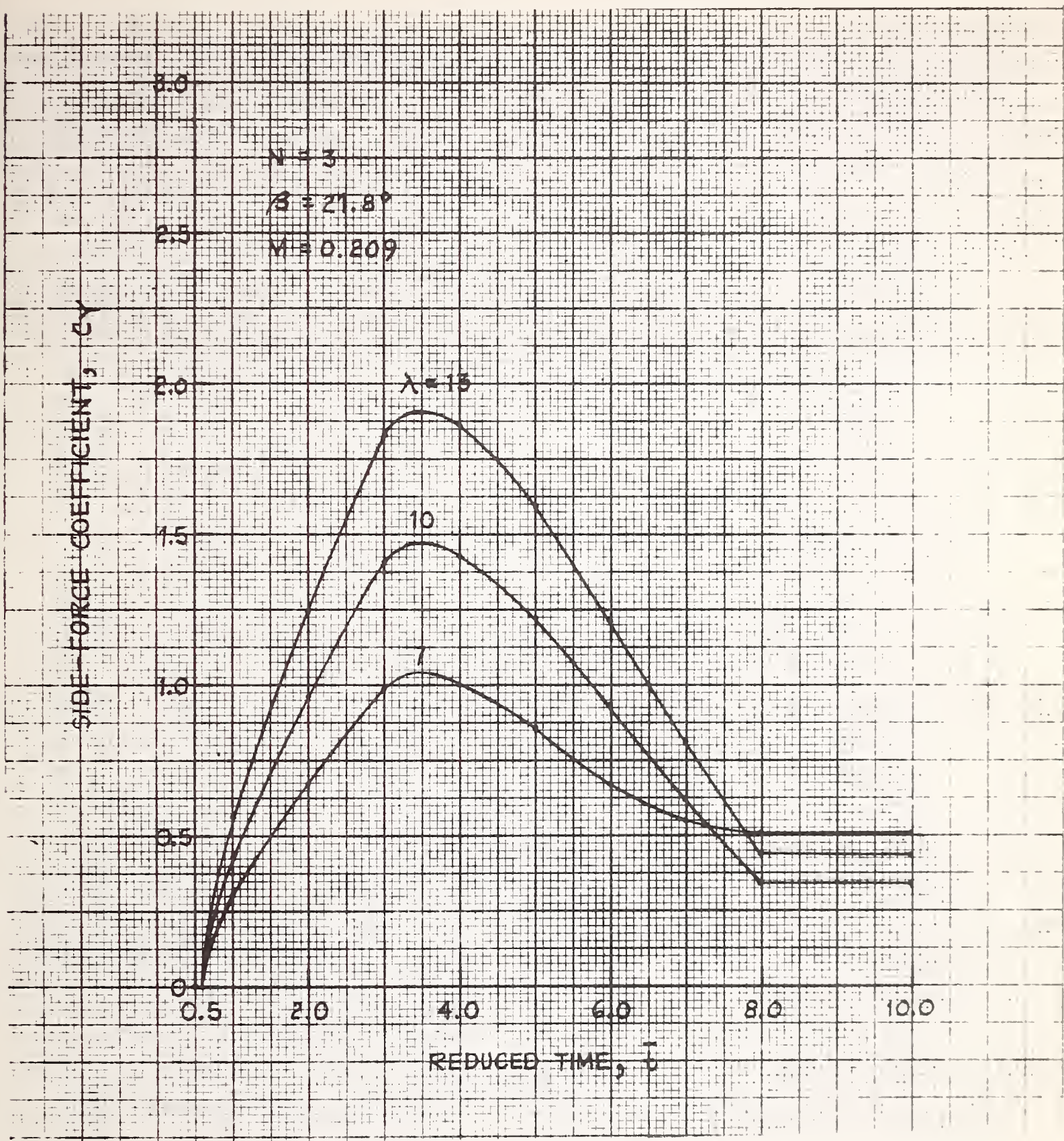
$$c. \gamma = 0.6$$

Fig. 2.14 (Concluded)



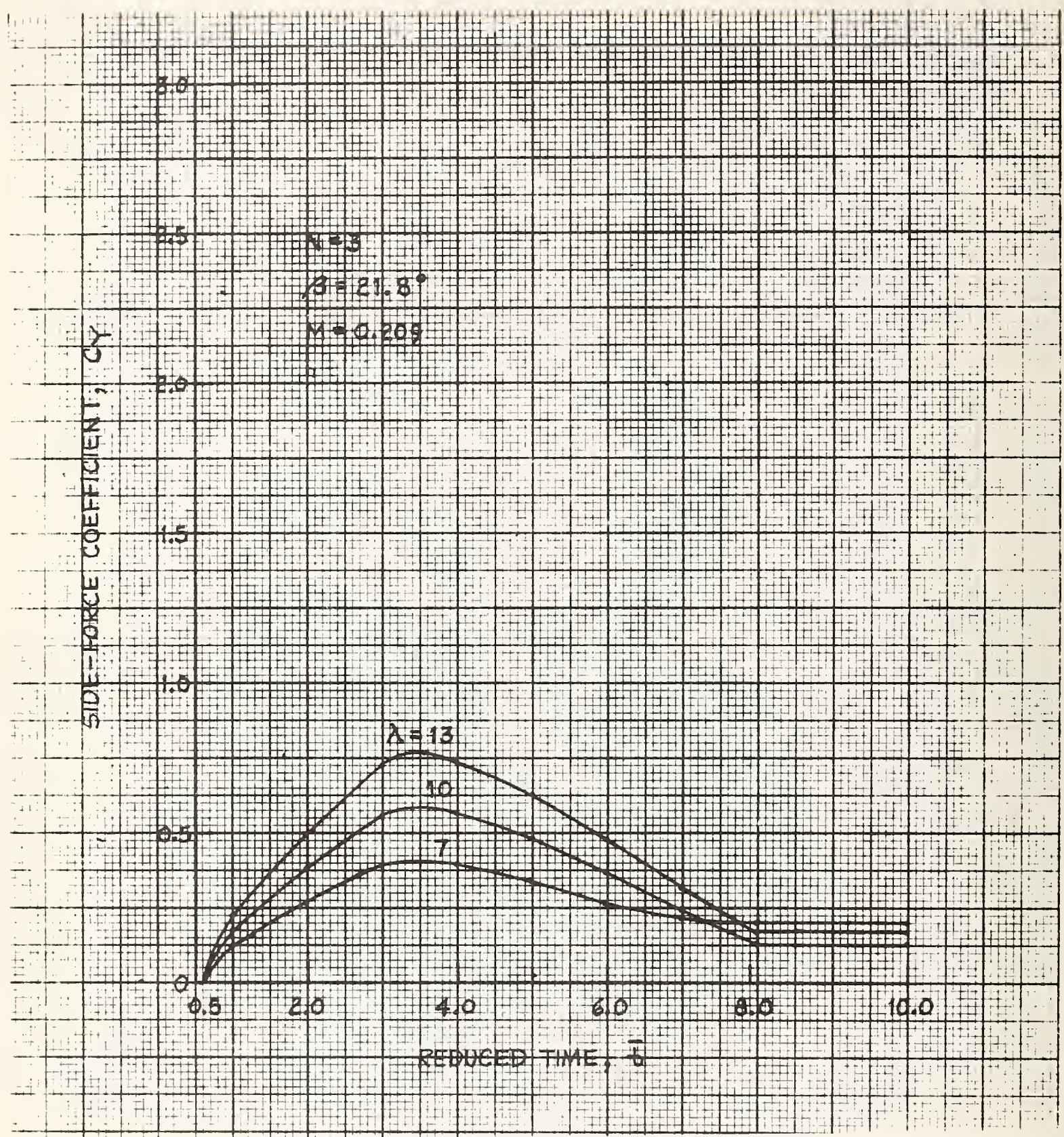
a.  $\gamma = 0$

Fig. 2.15 Variation of Side-Force Coefficient With Reduced Time for Various Side-Rail Heights. Third Car.



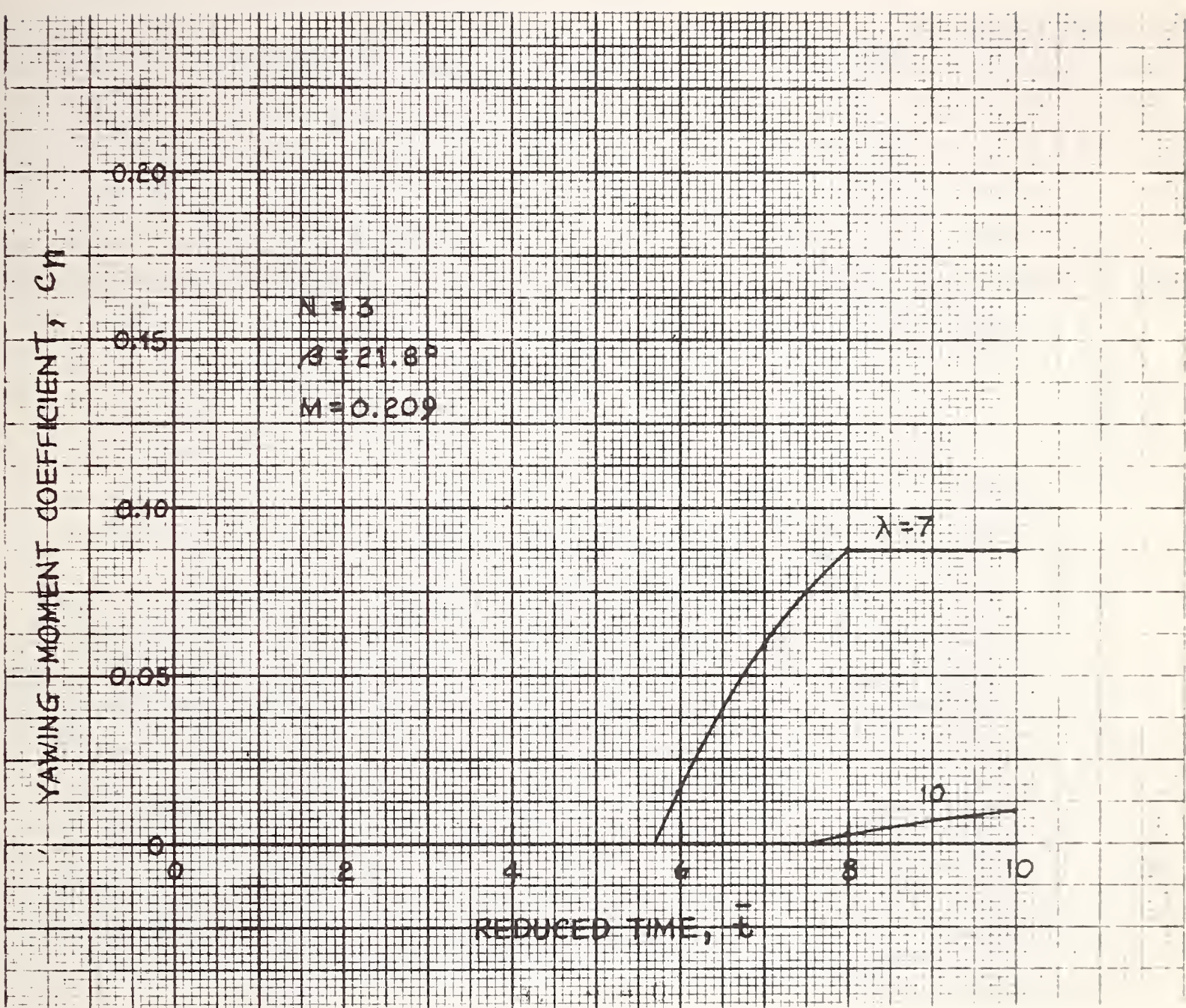
$$b \cdot \gamma = 0.3$$

Fig. 2.15 (Continued)



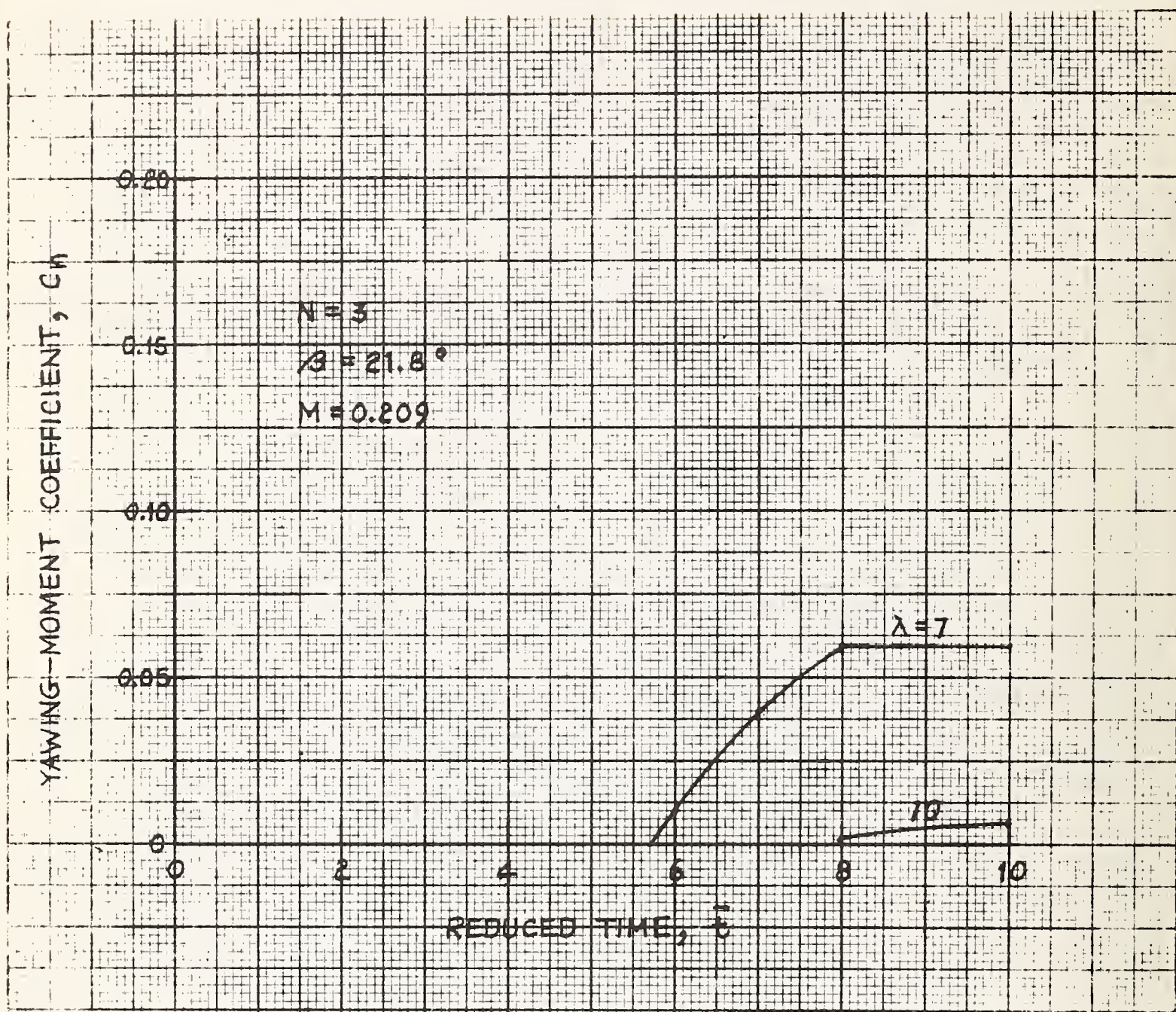
$$c. \quad \gamma = 0.6$$

Fig. 2.15 (Concluded)



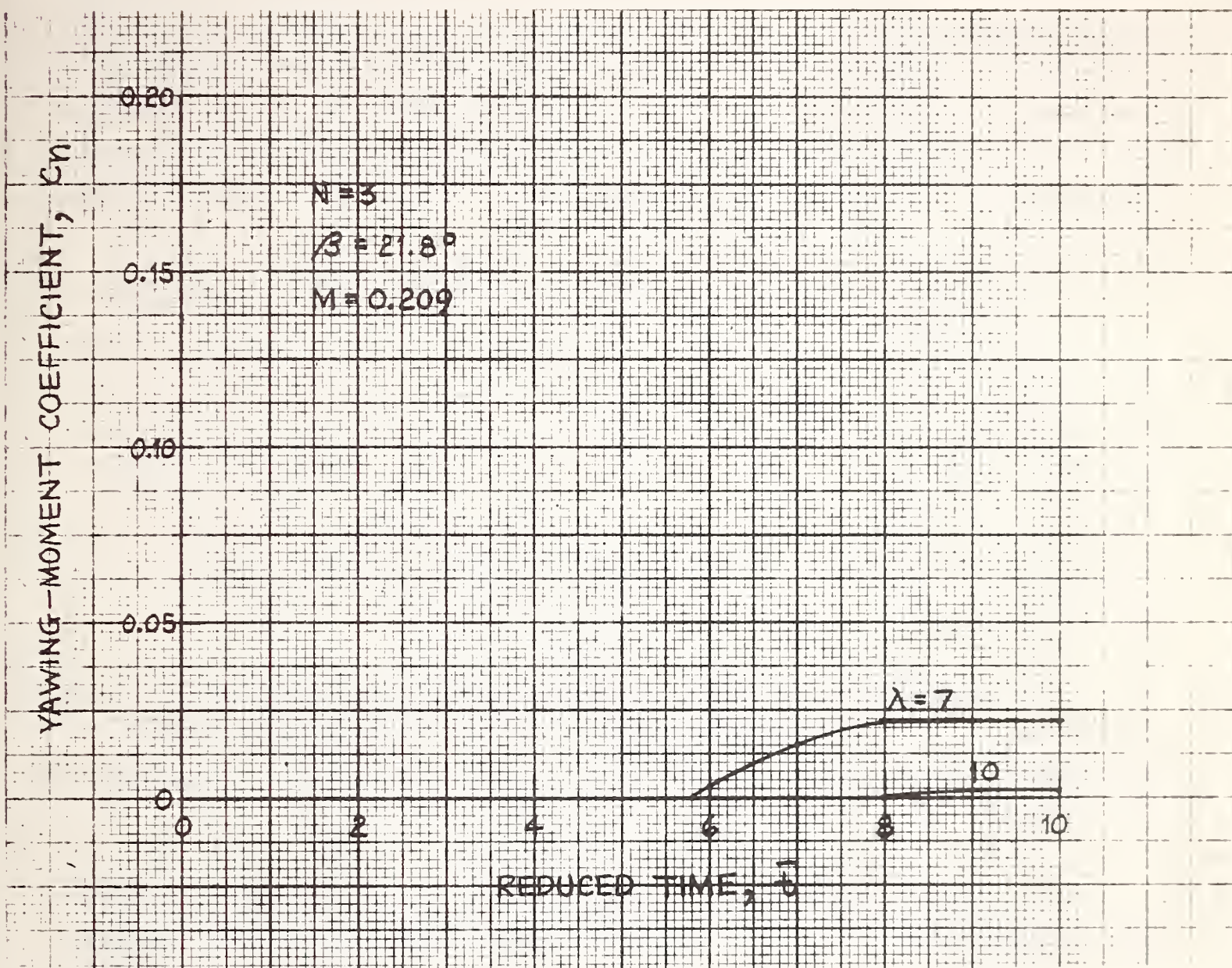
$$a. \quad \gamma = 0$$

Fig. 2.16 Variation of Yawing-Moment Coefficient With Reduced Time for Various Side-Rail Heights. Third Car.



b.  $\gamma = 0.3$

Fig. 2.16 (Continued)



$$c. \quad \gamma = 0.6$$

Fig. 2.16 (Concluded)

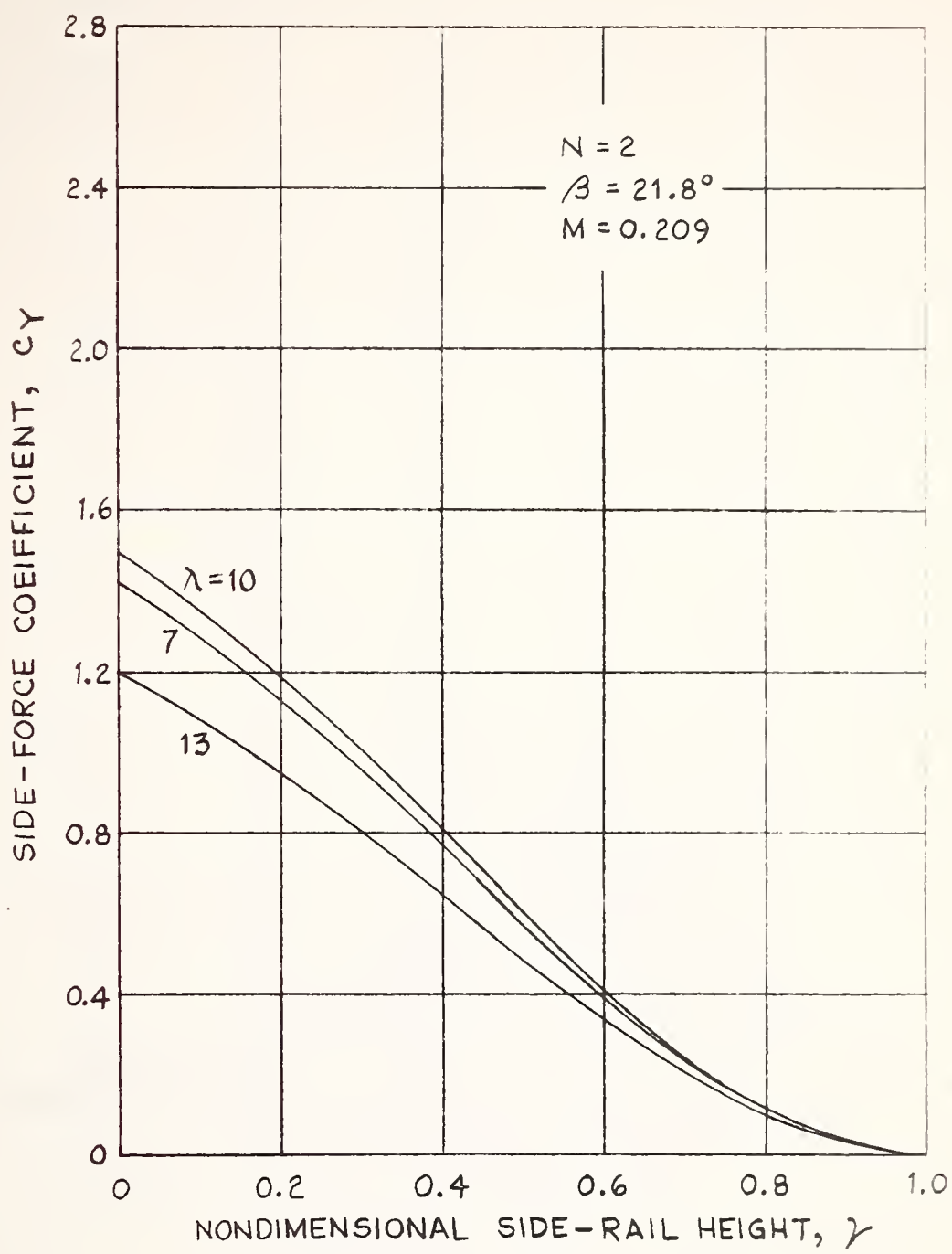
The importance of this transient peak in  $C_Y$  is that it would not be measured on the second and third cars in steady-state tests. However, the peak value for the second and third cars is very nearly equal to the steady-state value for the first car for these values of  $\lambda$  and  $\beta$ . This is due to the fact that the peak side force occurs when the leeward vortices are relatively close to the vehicles, at about the steady-state distance reached for the first vehicle.

The peak side force for all cars could be obtained from the steady-state value for the first car for a wide range of  $\lambda$  and  $\beta$ , but the question should be resolved individually for each case. If the train speed is doubled, for example, the peak section side force due to viscous cross flow would occur twice as far rearward, so for  $\lambda = 7$ , for example, the transient peak would be greater on the second and third car than the first car.

The yawing-moment coefficient for the second and third car grow essentially monotonically to the steady-state value. Therefore, the maximum value of  $C_n$  could be obtained from steady-state tests.

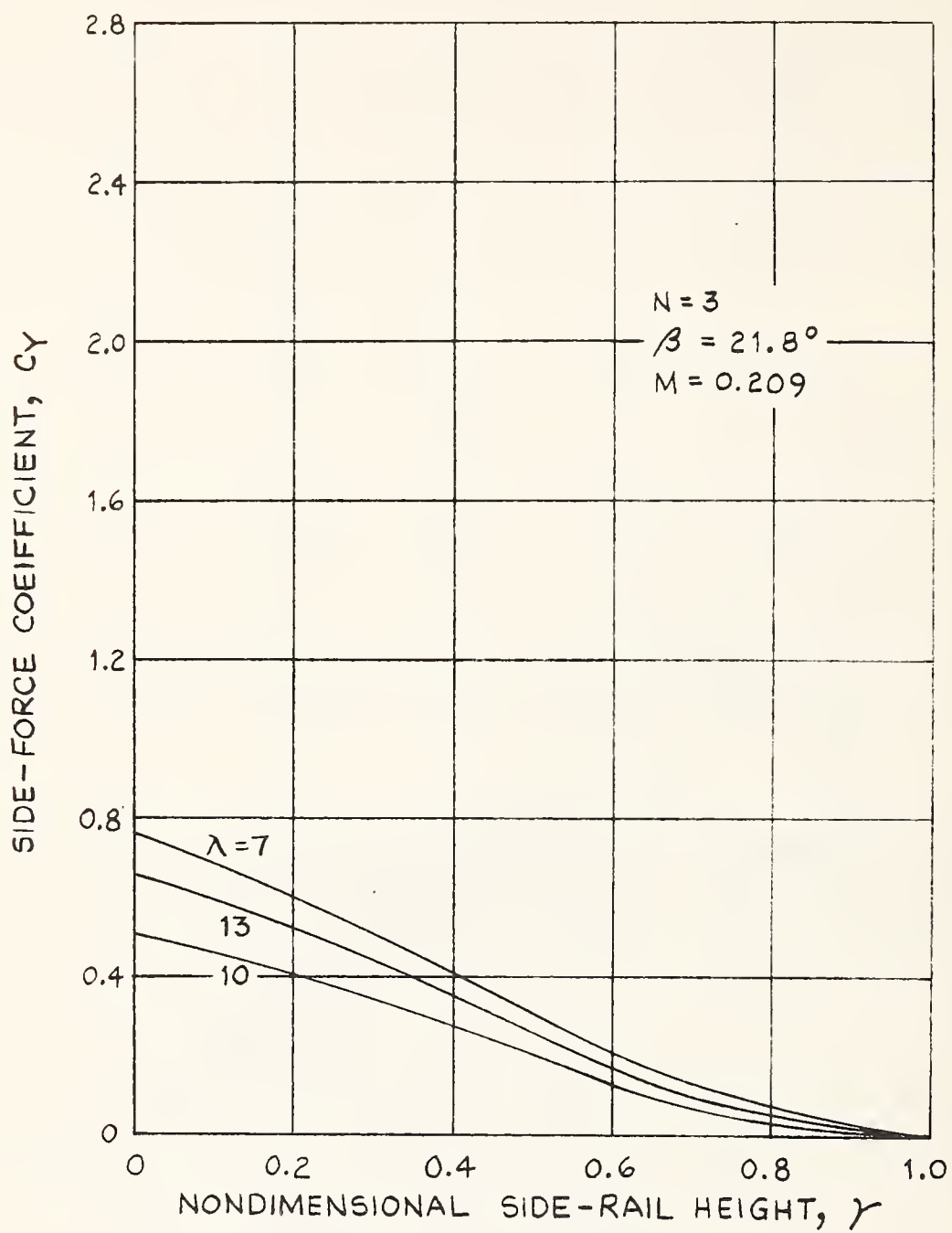
The effect of side-rail height is to markedly reduce the steady-state  $C_Y$  for the second and third cars also, Figure 2.18. A height equal to 43 percent of  $H_v$  would cut  $C_Y$  in half.

The side rail also reduces the steady-state  $C_n$  for the second and third car, Figure 2.19.  $C_n$  does not become negative, however, as it did for the first car (Figure 2.9).



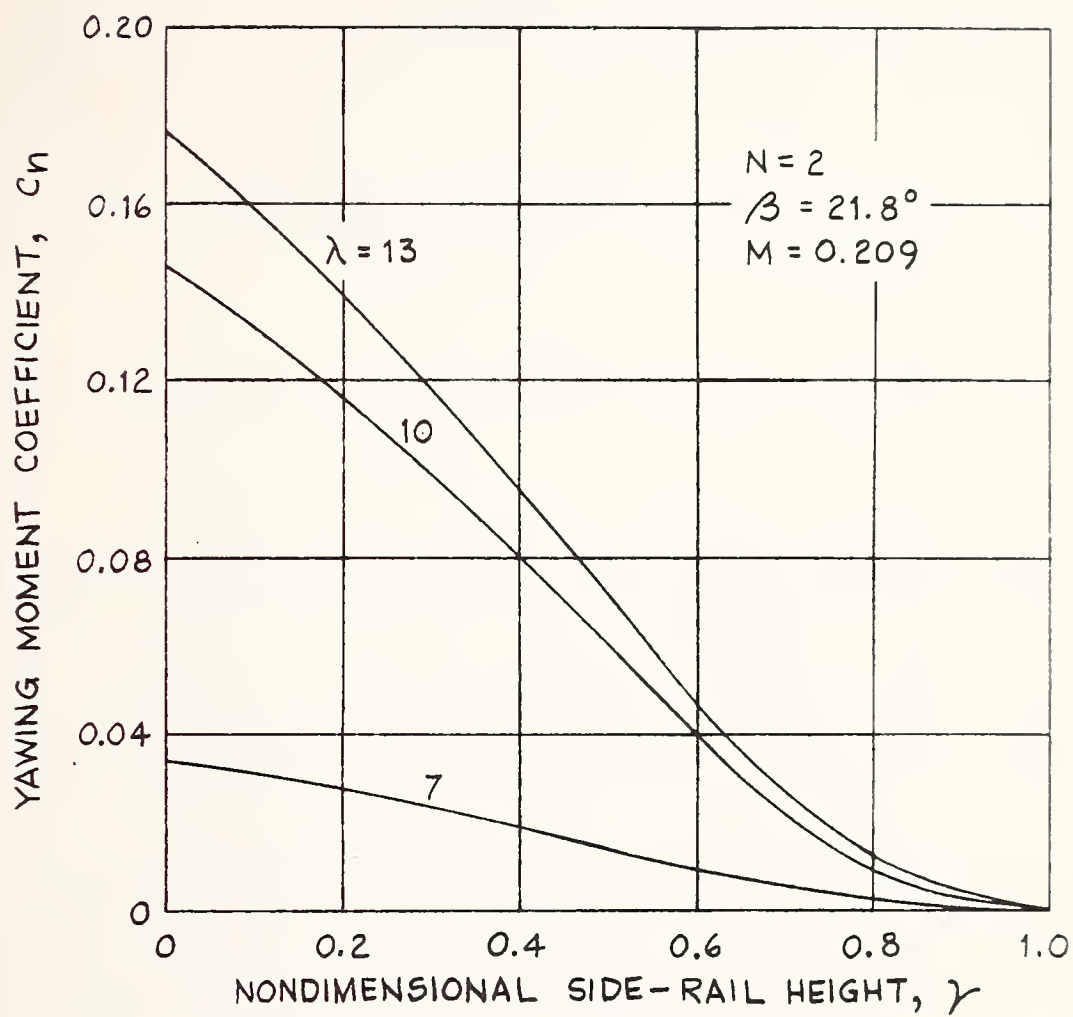
a. SECOND CAR

Fig. 2.18 Variation of Steady-State Side-Force Coefficient With Side-Rail Height.



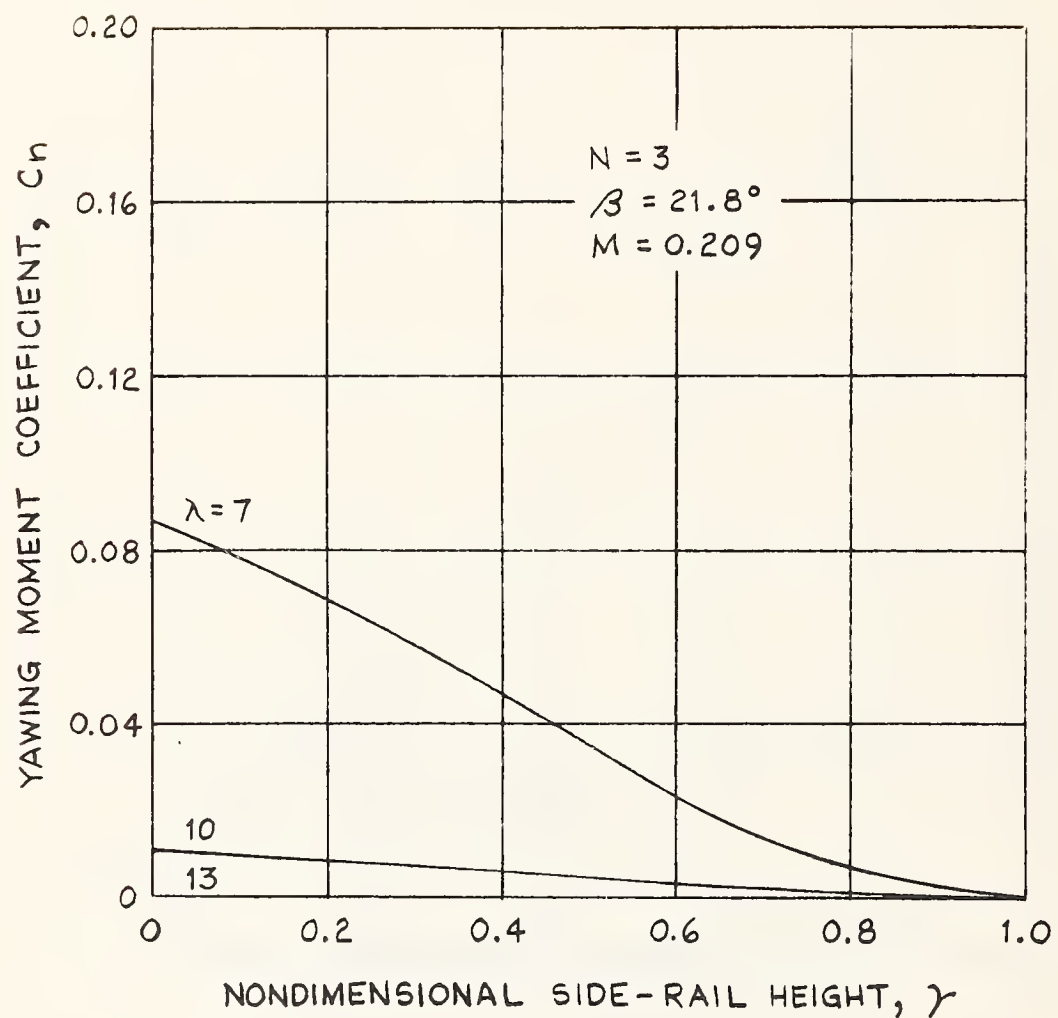
b. THIRD CAR

Fig. 2.18 (Concluded)



a. SECOND CAR

Fig. 2.19 Variation of Steady-State Yawing-Moment Coefficient With Side-Rail Height.



b. THIRD CAR

Fig. 2.19 (Concluded)

## 2.6 CONCLUSIONS

Based on the analysis of calculations carried out here for a vehicle subjected to a sudden side gust producing about a  $20^{\circ}$  sideslip angle and measurements reported by Grunwald<sup>2</sup>, the following conclusions are reached.

1. For TACV vehicles, the initial peak in the side force, due to non-viscous, slender-body forces, is probably too brief to be important. The side force reaches a second peak in about the time the gust-induced flow travels 2.5 to 3.5 body heights. This time depends upon the vehicle dimensions ( $\lambda$ ) and the sideslip angle ( $\beta$ ) produced by the gust. The ratio of this peak side force to the steady-state value is nearly unity for the first vehicle in a train, 1.1 to 2.4 for the second car, and 2.0 to 4.3 for the third car.

2. A side-rail height of 35 to 43 percent of the train height would reduce the steady-state side force 50 percent. Based on slender-body theory, Woolard<sup>10</sup> shows that a side-rail height of 23 percent would reduce the steady-state side force on a single car having an elliptic cross section by 50 percent. The inclusion of viscous forces, then, is to reduce the effect of side-rail blockage somewhat. The wall effect may be even greater than these theories indicate because of separation of the side wind from the windward rail in the vicinity of the nose which is not taken into account.

3. The predicted steady-state side force for a single vehicle is 2.13 times the value measured by Grunwald<sup>2</sup> on a half-circle-cross-section body. Measurements by Perkins and Jorgensen<sup>3</sup> and Schindel<sup>7</sup> on bodies in wind tunnels support the predicted value. The difference is apparently due to ground-plane effects, which are not included in the theory.

4. The measurements by Grunwald<sup>2</sup> on a body without side rails indicate the ground-plane gap and bottom configuration of the body have a strong and interacting effect on the steady-state side force, rolling moment and lift. Configurations with rounded bottoms have the greatest sensitivity to gap height, flat-bottomed configurations being nearly insensitive. At small gap heights, the side force for rounded bottoms is double the flat bottom value.

5. To evaluate ground-plane simulation in wind-tunnel tests and to determine the effects of ground plane gap, side-rail protection and body shape on side forces, pressure measurements on the body would be very useful.

6. Tests with a moving model should answer the unresolved questions on ground-plane simulation, side-rail effects, and passing-train-induced airloads.

### 3. FEASIBILITY ANALYSIS OF LABORATORY FACILITY FOR MEASURING TACV GUST AIRLOADS

#### 3.1 INTRODUCTION

The analysis of Section 2 indicates further development of ground-plane simulation could be important to the measurement of aerodynamic forces and moments on a TACV model. The airflow between the bottom of a TACV configuration and the ground plane appears to be critical, and it is expected to be effected by any boundary layer on the ground plane.

A belt moving at the free-stream velocity, as in the Langley facility<sup>2</sup>, eliminates boundary-layer formation, whereas a gust in the atmosphere, which a TACV would be exposed to, would develop a boundary layer. The magnitude of this effect is difficult to determine now, inasmuch as force and moment measurements by Grunwald<sup>2</sup> in the Langley facility indicate a relatively small difference for moving-belt and stopped-belt tests. It has been well demonstrated elsewhere, however, that flow separation is effected significantly by the presence of a boundary layer (drag of spike-nose bodies, control-surface separation, corner flow, etc.), therefore the ground-plane simulation with fixed models and partial boundary-layer simulation remains an open question.

Other questions a moving-model facility can be used for with definite advantage are: measurement of (1) side-rail effects and of (2) passing-train-induced airloads. A side rail is difficult to mount in a wind tunnel with provision for contact (or negligible clearance) with a moving-belt ground plane. Passing-train tests in a wind tunnel would require a track parallel to the load-test model and a passing-train speed double the wind-tunnel air speed.

These problems and questions on TACV simulation can, conceptually, be eliminated by testing with a moving model

and a fixed ground plane. The problem in the past has been to provide acceptable accuracy and workability in tests involving moving models. Yet, moving-model tests in an air medium have been carried out - gust-tunnel tests, for example. The feasibility of performing TACV simulation tests, therefore, with moving models in a laboratory facility is explored here. There generally are a number of design solutions to a design problem. The objective of the present study is not competitive design selection, but determination of feasibility.

### 3.2 GENERAL CONSIDERATIONS

#### Track Layout

The layout of the type of moving-model facility here considered is sketched in Figure 3.1. The test model moves on a linear track with an acceleration zone, a constant-speed zone and a deceleration zone. The wind for gust simulation is located in about the mid-region of the constant-speed zone. To verify that effects of the model acceleration have disappeared and to confirm balance tare data, tare measurements on the model balance would be made within the constant-speed zone before the model enters the wind. A zone is also provided after the model leaves the wind to recheck tare measurements before deceleration forces are applied.

A second track, parallel to the constant-speed zone, provides for passing-train airloads testing. Measurements would not be made on the second train, so an oval track with a straight section parallel to the constant-speed zone would suffice. Side rails, fences and other physical factors affecting TACV airloads could be added to the installation.

#### Model Characteristics

A representative model configuration, Figure 3.2, is selected for design purposes from the configurations tested by Grunwald<sup>2</sup>. This configuration was selected because, it is

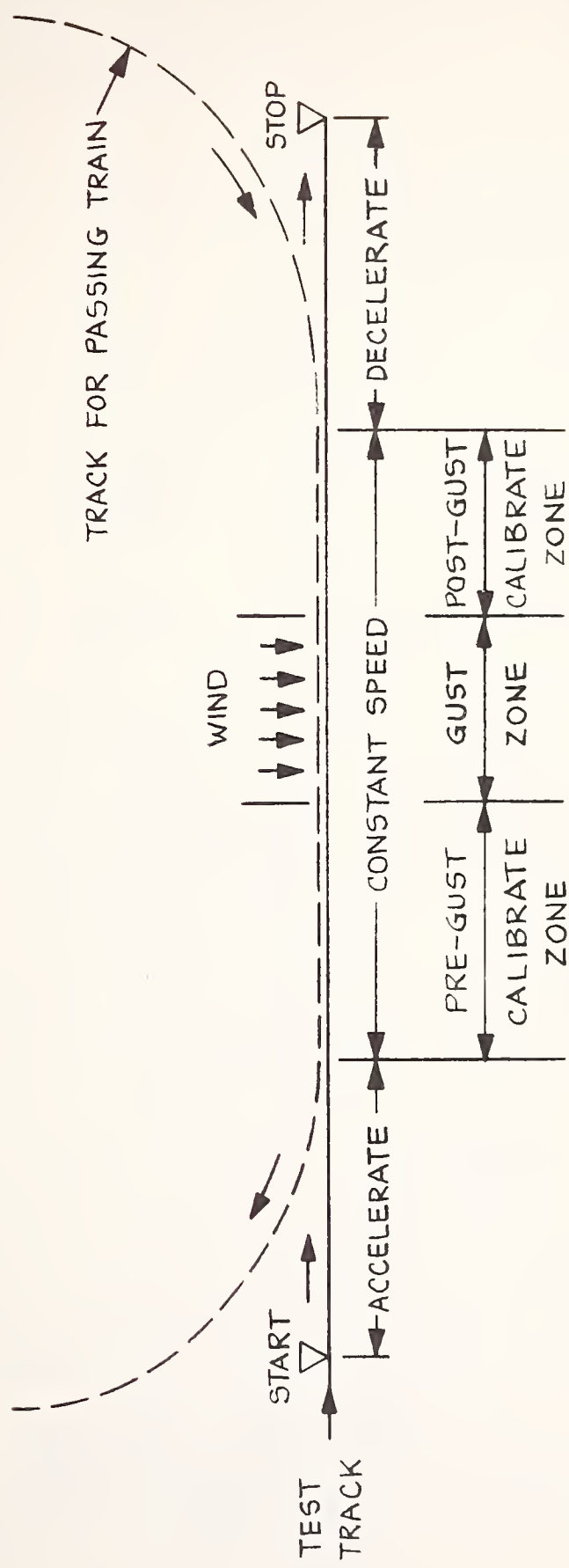


Fig. 3.1 Layout of Experimental Track

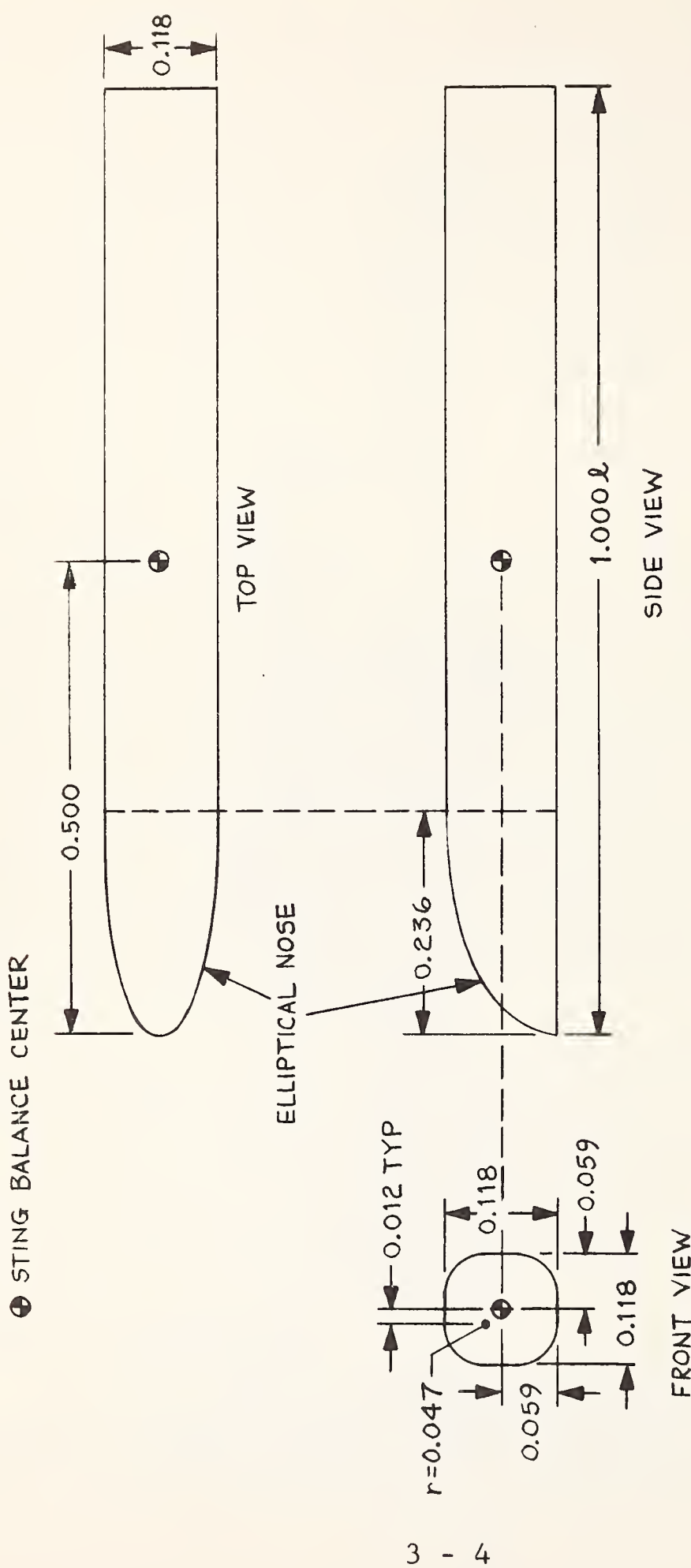


Fig. 3.2 Configuration of Representative Model Selected for Feasibility Study.

believed, it most nearly represents the shape that is used in present TACV designs. The corner radii on the bottom surface are relatively large, but some rounding may be advantageous, so this is not considered critical.

The model components are sketched in Figure 3.3. The model body is supported by a balance, mounted on a strut to a carriage. The balance is used to measure the forces and moments applied to the body. The loads are transmitted through the strut to the carriage, which travels on ways. A battery-powered amplifier inside the model body with appropriate bridge circuitry boosts the balance signal for transmission to external recorders through sliding contacts. The battery and amplifier are strut supported.

For small models, the amplifier and bridge could be mounted on the carriage. It is important to amplify the bridge signal before transmission to reduce contact noise effects. Weight and power requirements for an amplifier have not been examined, but it is assumed solid-state amplifiers currently available would meet the requirements. If necessary, a recorder could be mounted on the carriage (similar recorders have been used on board rocket-propelled sleds); propulsion requirements would increase considerably due to recorder weight, but it provides an alternative method.

Dimensions and estimated weights for three model sizes have been made, and the results are tabulated in Table 3.1. Model I is based on a 1.0-ft<sup>2</sup> cross section. The other dimensions follow from Figure 3.2. For the model body, a built-up structure of waffle-back stiffened plastic, cast or molded phenolic, is assumed. The balance-mounted weight, which includes the body shell, stiffeners and attachments, is 170 pounds. An equal weight is assumed for the balance, strut, carriage and electronic components, giving a total moving weight of 340 pounds.

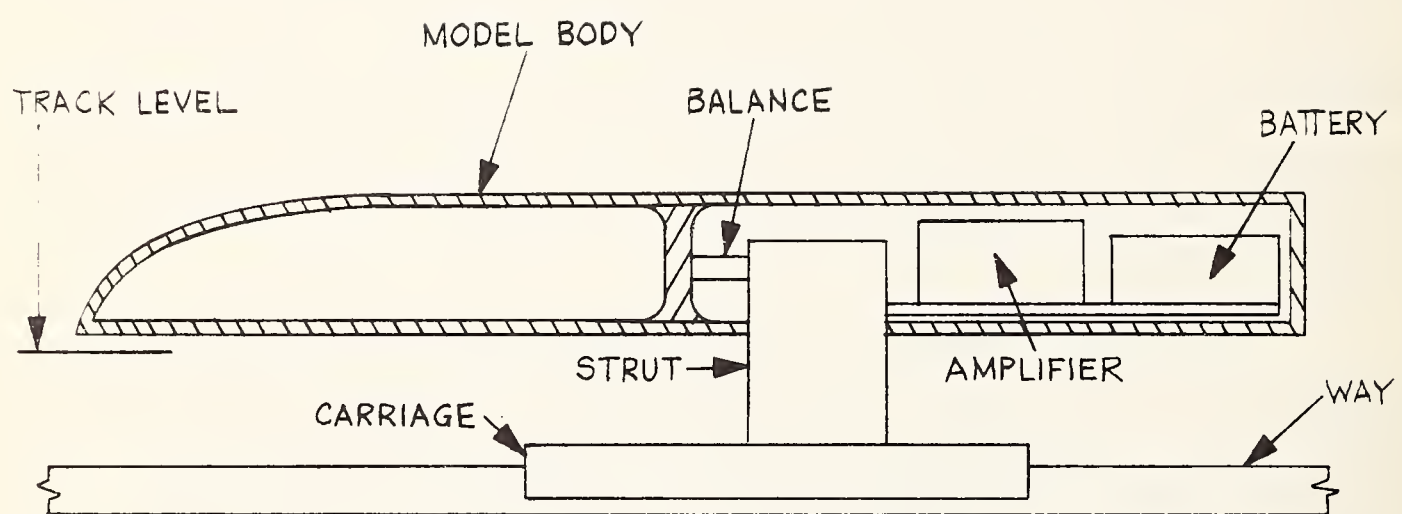


Fig. 3.3 Schematic Drawing of Model, Components, Balance, Strut, Carriage and Way.

Model II is based on a 1/2-ft model height. The weight is estimated by cubic scaling with the model dimensions.

TABLE 3.1  
MODEL  
DESIGN CHARACTERISTICS

MODEL	L ft.	H ft.	$S_b$ ft. <sup>2</sup>	$d_e$ ft.	BALANCE- MOUNTED WEIGHT 1b.	MOVING WEIGHT 1b.
I	9.118	1.08	<u>1.000</u>		170	340
II	4.25	<u>0.501</u>	0.216		17	34
III	<u>1.00</u>	0.118	0.0120	0.153	0.9	1.9

Model III is based on a one-foot model length. Because of associated weights, it does not appear reasonable to expect cubic scaling for small models, so the weight of model III is estimated from model II by square-law scaling.

#### Reynolds Number

The variation of model Reynolds number, based on model length, L, and speed, V, is presented in Figure 3.4 as a function of model speed for the 3 models. As a basis of reference, wind-tunnel tests by Perkins & Jorgensen<sup>3</sup> on a 10-caliber ogive-cylinder body with a 3-caliber nose indicate the loading at a  $10^\circ$  angle of attack changes between a Reynolds number of  $1.45 \times 10^6$  and  $4.4 \times 10^6$ , but at  $15^\circ$  and  $20^\circ$  it is essentially the same. The Reynolds number in tests by Grunwald<sup>2</sup> is indicated in Figure 3.4

For a gust-induced angle of sideslip of  $15^\circ$  or more, it appears the Reynolds number should be at least  $1.5 \times 10^6$ . Models I and II meet this criterion. The Reynolds number for

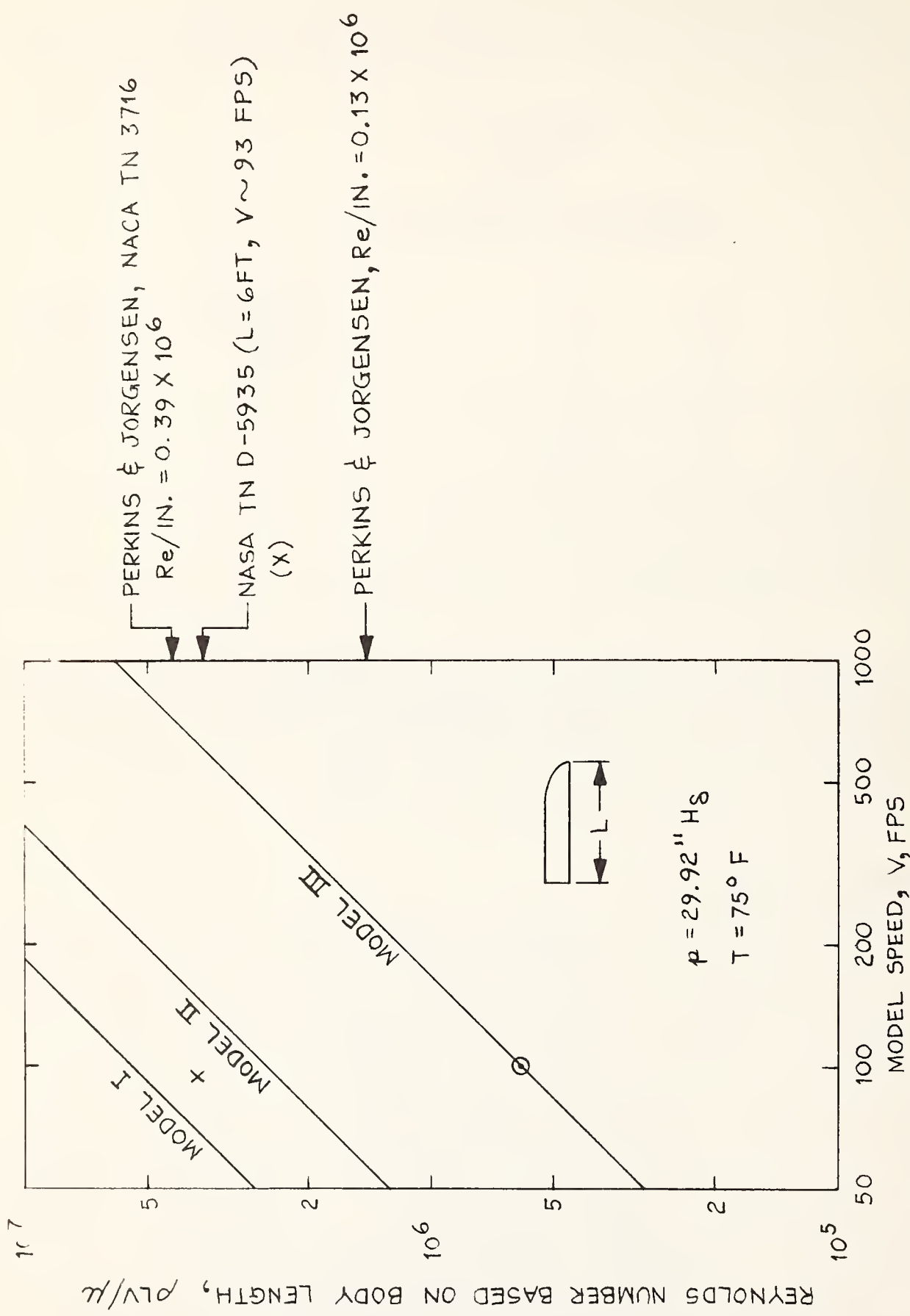


Fig. 3.4 Comparison of Reynolds Number Based on Model Length for Three Models and Values for Models Tested in Wind Tunnels as a Function of Model Speed.  
 $\rho = 20^\circ$

model III is  $0.6 \times 10^6$ , which means laminar separation might occur, resulting in a larger lateral force than for turbulent separation. From a safety point of view, this is conservative. To meet the Reynolds number requirement with model III, a speed of 250 fps is needed.

### Gust Side Force

The steady-state side force due to a side-slip angle of  $20^\circ$  is plotted in Figure 3.5 for the models. At 100 fps, it ranges from 26 pounds to 0.3 pounds. More important to balance measurements on a moving model is the ratio of the side force and model weight, shown in Figure 3.6. As this figure shows, the problem with a large model, as for birds and aeroplanes, is the trend toward a high mass to aerodynamic loading ratio. For models II and III, the side-force-to-weight ratio at 100 fps is 0.17.

### Acceleration Distance

The distance to accelerate (or decelerate) a model at constant forward acceleration,  $\ddot{x}$ , is plotted in Figure 3.7. From design experience, 50-g's is a reasonable upper limit on acceleration. Laboratory space frequently being a factor, 20-g's is taken as a lower limit on acceleration. It is expected that laboratory space for testing with large models would be greater than for small models, so a 50-ft. limit is placed on acceleration distance for model II and 10-ft. for model III. A lower speed of 150 fps is used for model II to meet the Reynolds number of the Langley tests.<sup>2</sup> The lower limit on speed for model III is set by requiring  $Y/W > 0.1$  at  $\beta = 20^\circ$ .

The design point for model II is chosen at  $V = 250$  fps,  $s = 30$  ft. and for model III at  $V = 100$  fps,  $s = 5$  ft.

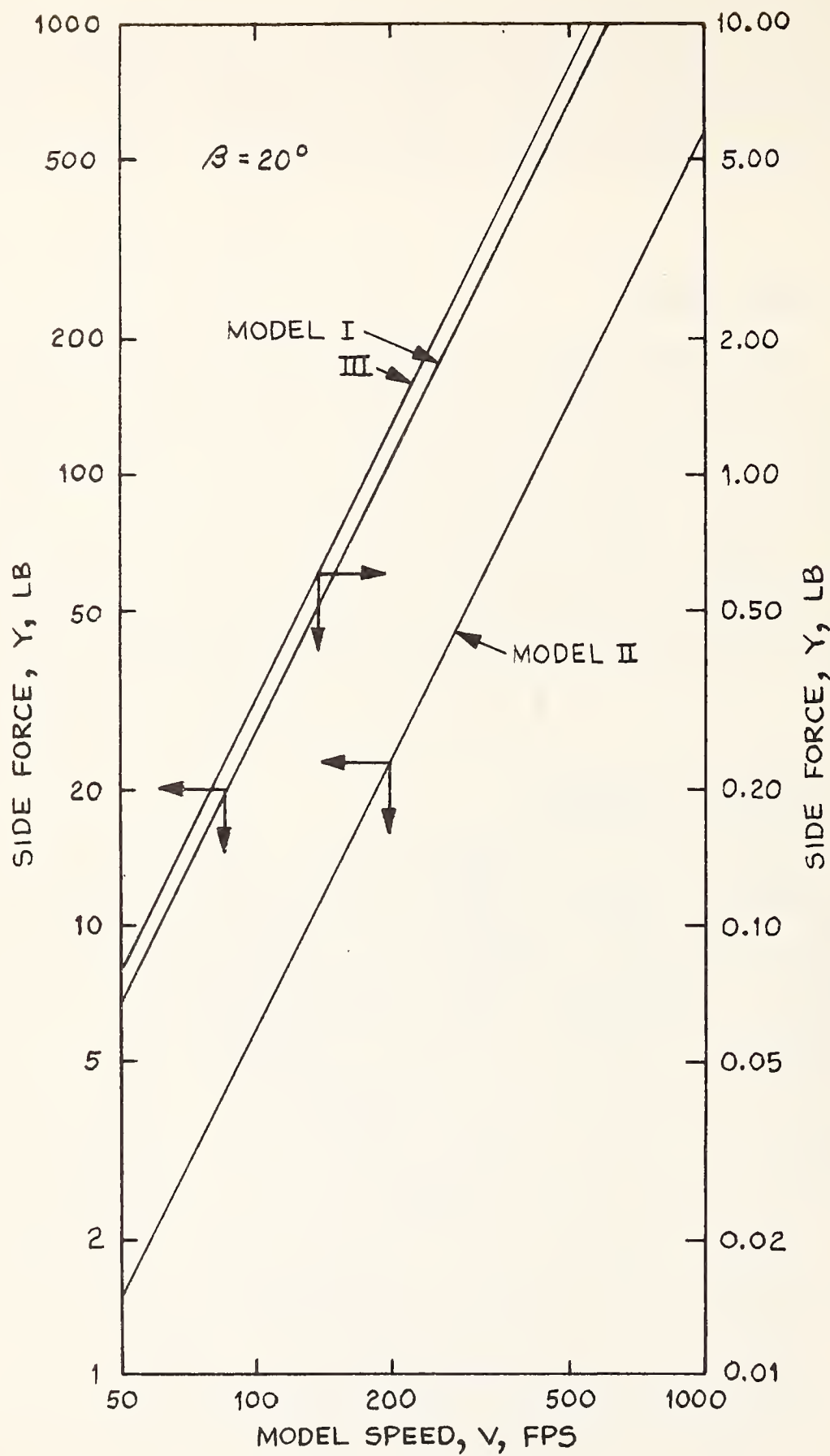


Fig. 3.5 Side Force for Three Models as a Function of Model Speed.  $\beta=20^\circ$ .

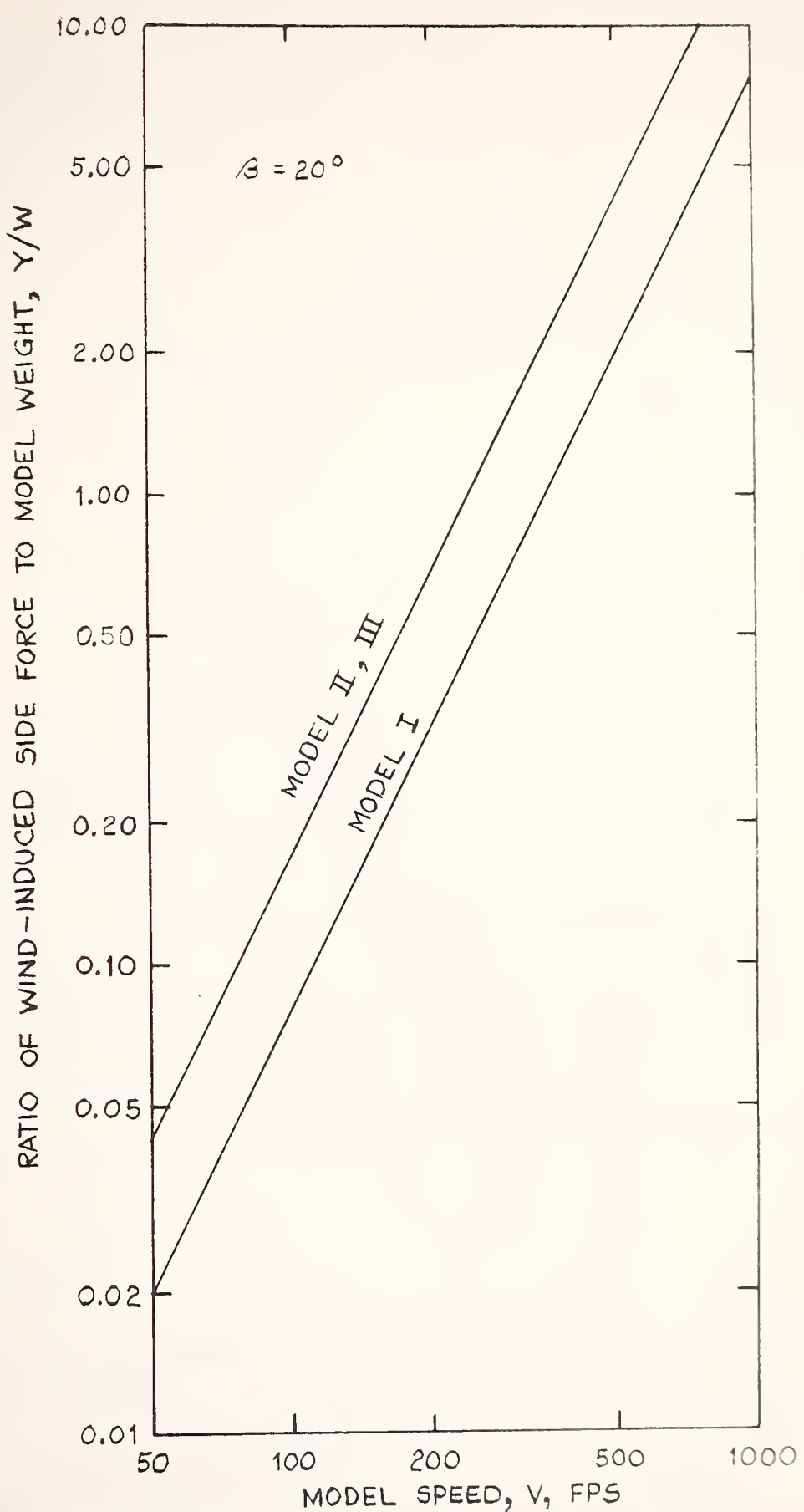


Fig. 3.6 Side-Force/Model-Weight Ratio for Three Models as a Function of Model Speed.

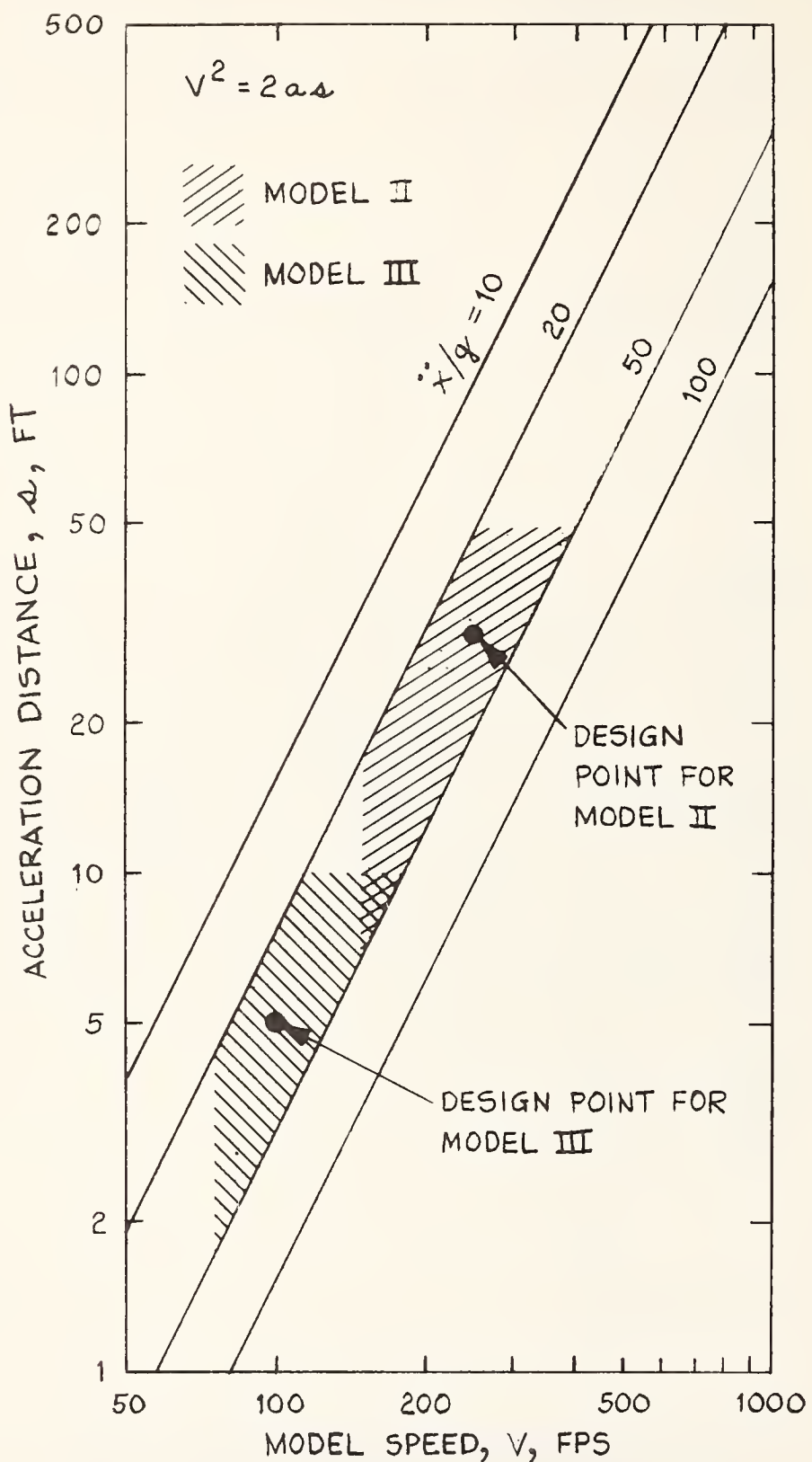


Fig. 3.7 Distance Required to Attain Test Speed with Constant Acceleration from Rest.

### Support-Carriage/Way Requirements

The support carriage must travel on a smooth way to minimize vertical acceleration of the model through the support. Vertical sinusoidal acceleration of a rigid model is plotted in Figure 3.8 as a function of the period with amplitude as a parameter.

For reference, a model traveling 100 fps through a 5-ft-wide wind field would experience a wind duration of 0.05 sec, which is roughly equivalent to a 0.1-sec period for a sinusoid. To keep the carriage-induced vibrations of a rigid system an order of magnitude below the steady-state wind-induced acceleration of 0.17 g's for models II and III, the half-amplitude of the waviness in the ways must be no more than  $\pm 0.002$  in. This requires a lathe-bed quality of smoothness. This smoothness requirement is limited to the constant-speed zone of the track. A lathe-bed length of 15 to 20 feet should be satisfactory for model III, so meeting guideway smoothness requirements appears feasible.

Model II traveling at 250 fps would experience a steady-state side force due to wind at  $20^\circ$  of 1.0 g's (Fig. 3.6). For the same sinusoidal period of 0.1 second and same vertical acceleration limitation of  $\ddot{y}/g < 0.1 Y/W$ , the half-amplitude would need to be 0.01 in. or less. This requirement is comparable to new runway construction; it could be readily met in a laboratory facility.

### 3.3 CABLE SYSTEM

Having considered the general factors in a moving-model facility, a means of propelling the carriage, model, etc. must be selected. A cable scheme is first examined, Fig. 3.9, for testing with model III.

In the cable system, as the others considered, the carriage travels on a way independent of the propulsion scheme.

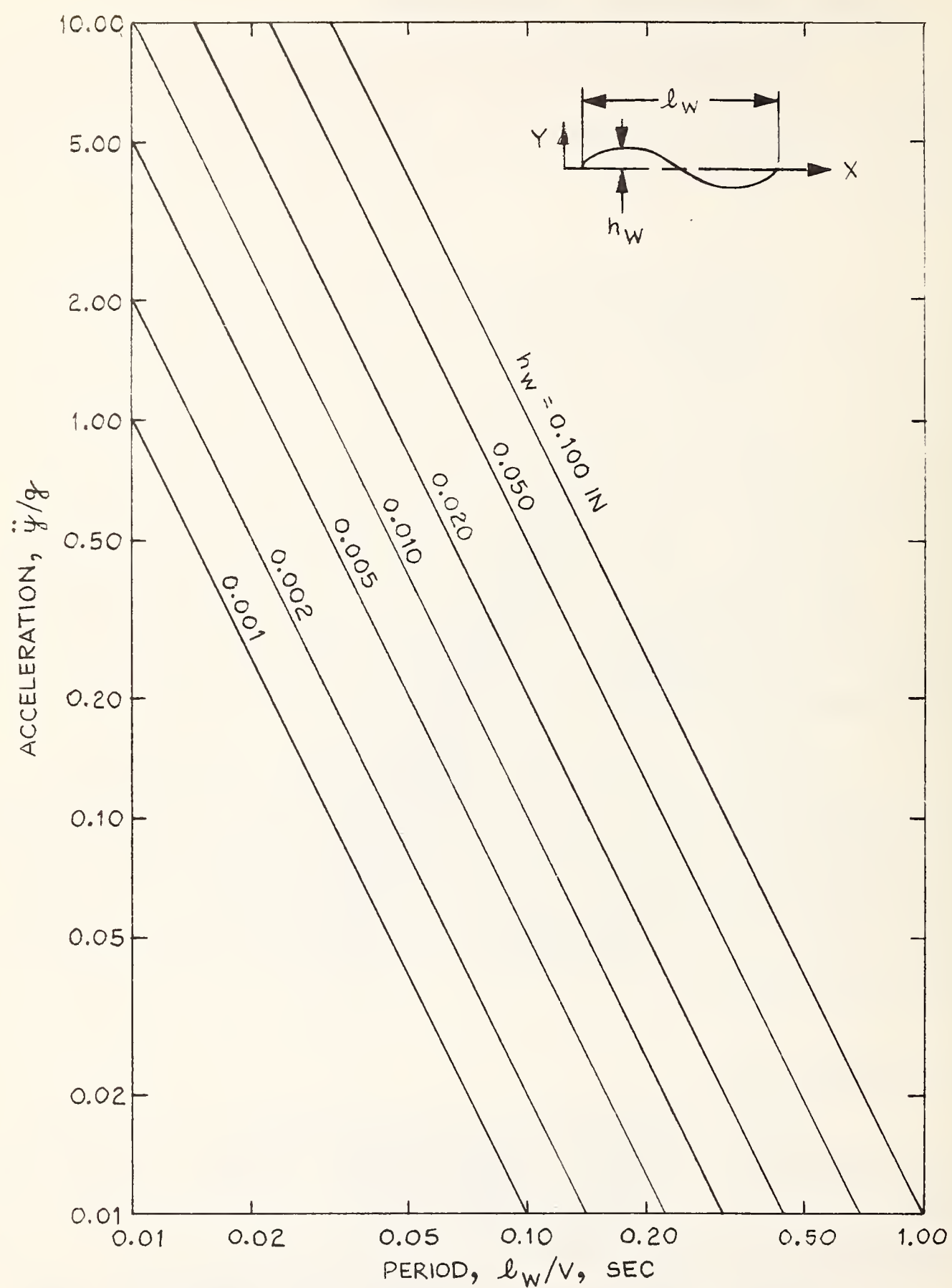
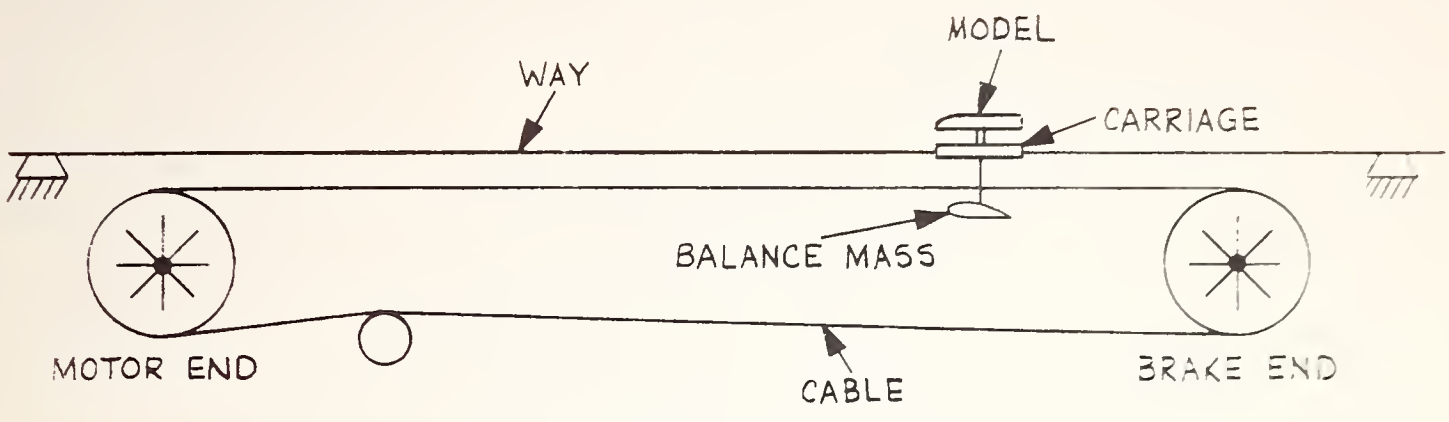
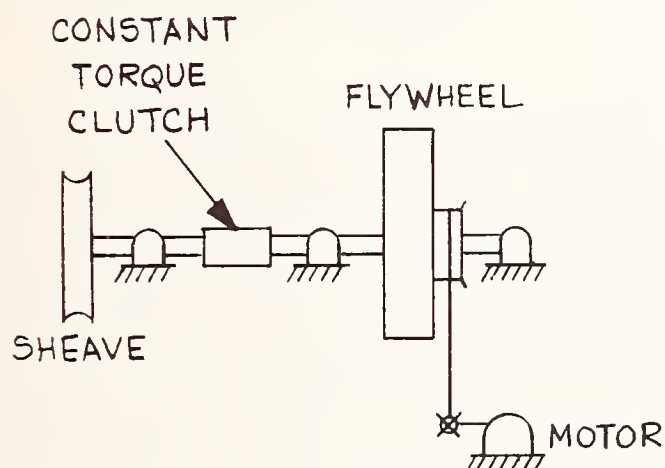


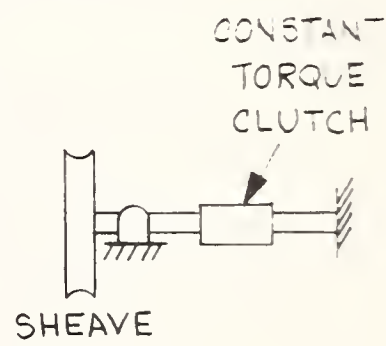
Fig. 3.8 Variation of Acceleration with Period for Sinusoid as a Function of Half Amplitude.



a. SKETCH OF LAYOUT



b. MOTOR END



c. BRAKE END

Fig. 3.9 Schematic Drawing of Test Facility Using Cable-Propelled Models.

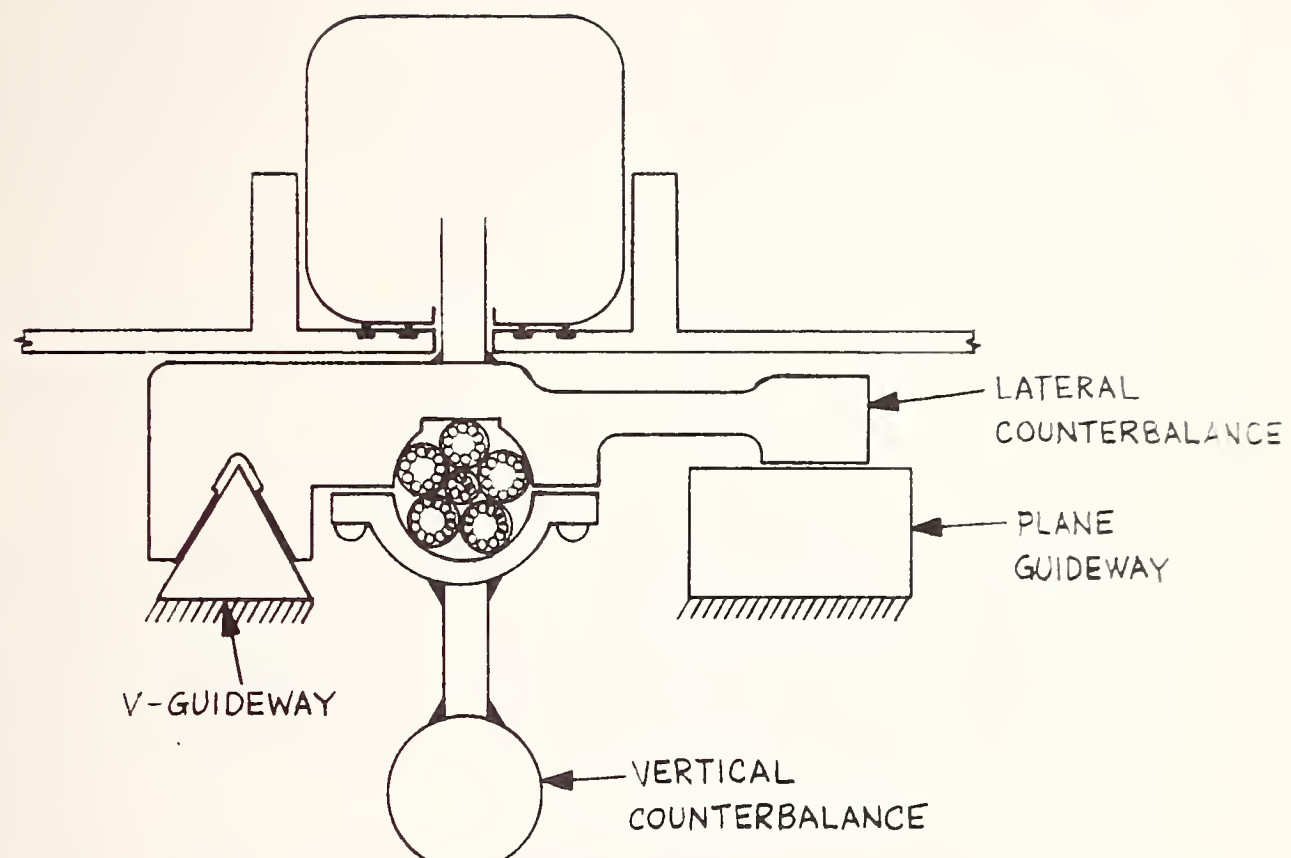
An endless steel cable running between two large sheaves is connected to the carriage, Figure 3.9. The cable is accelerated by the sheave on the motor end and decelerated by the sheave on the brake end. The carriage starts near the brake sheave and stops near the motor sheave.

The sequence of events is the following. A flywheel on the motor end is overspeeded and an electric constant-torque clutch is engaged, bringing the cable and carriage up to test speed. Power supplied by the motor maintains speed during the test. The system is stopped by disengaging the drive clutch and engaging a constant-torque clutch at the brake end.

A schematic of the carriage and model on a lathe-type way is sketched in Fig. 3.10a. The V-guideway establishes lateral position and, in combination with a plane guideway, vertical position. The cable passes through the center of gravity of the carriage-model system to minimize carriage-model rotation.

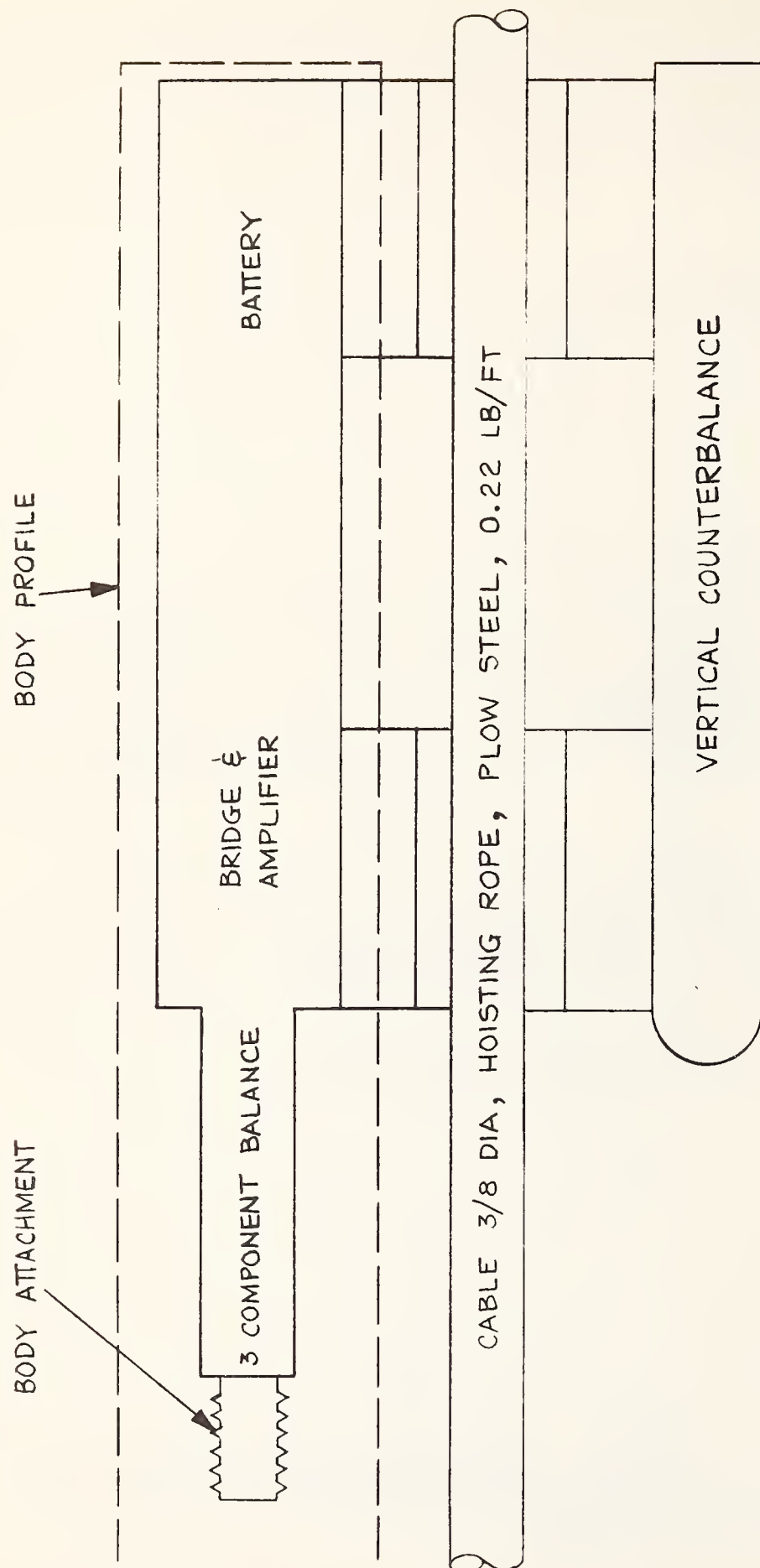
A side schematic is shown in Figure 3.10b. Hoisting rope, 3/8 dia., constructed of plow steel provides a breaking strength of 11,200 pounds. About 600 pounds force is applied to accelerate the carriage, model and cable, with additional force to accelerate the driven sheave and maintain rope tension.

The unknowns in this system are the vibratory vertical and lateral forces applied to the carriage due to whip in the rope induced by the initial acceleration forces. To apply and remove a 50-g acceleration force to the cable and isolate the model to less than 0.02 g's would require considerable care. Transmission of cable vibration might be reduced by using hold-downs on the ways or independent mounting of the cable attachment separate from the model carriage. Because of these problems, alternate means of propulsion are examined.



a. CROSS-SECTIONAL VIEW

Fig. 3.10 Schematic Drawing of Cable-Propelled Model and Carriage-Way System.



b. SIDE VIEW

Fig. 3.10 Concluded

### 3.4 ACCELERATE-COAST-DECELERATE SYSTEM

#### Accelerator

For model III traveling 100 fps, aerodynamic deceleration would be negligible. Therefore, a propulsion system comprising only of an accelerator and a decelerator is evaluated.

A simple air-piston accelerator, adapted from gun-tunnel launchers, is sketched in Figure 3.11. A ram attached to the end of a tubular ram driver pushes the model carriage from air pressure applied to the face of a piston attached to the driver. Air is supplied to the air chamber. The driver is restrained until the desired test time. After the driver is released, the ram pushes the carriage to the desired speed and is decelerated by the deceleration spring.

The piston could be constructed of a plastic with loose tolerances on the fit in the cylinder--air leakage past the piston and bearing, at the opposite end of the chamber, could be readily replenished by the supply air. The model speed would be controlled by the initial pressure in the air chamber.

The moving mass for model III is 1.9 lb. Allowing for future increases in model and carriage weight by a factor of 3, then 5.7 lb. of model and carriage system is to be accelerated. A 5-ft driving stroke of the ram, before reaching the spring, a 3-in ID cylinder and a 1-in OD driver would require pressure of about 135 psi to accelerate the model to 50-g. Increasing the cylinder diameter would allow for acceleration of larger models.

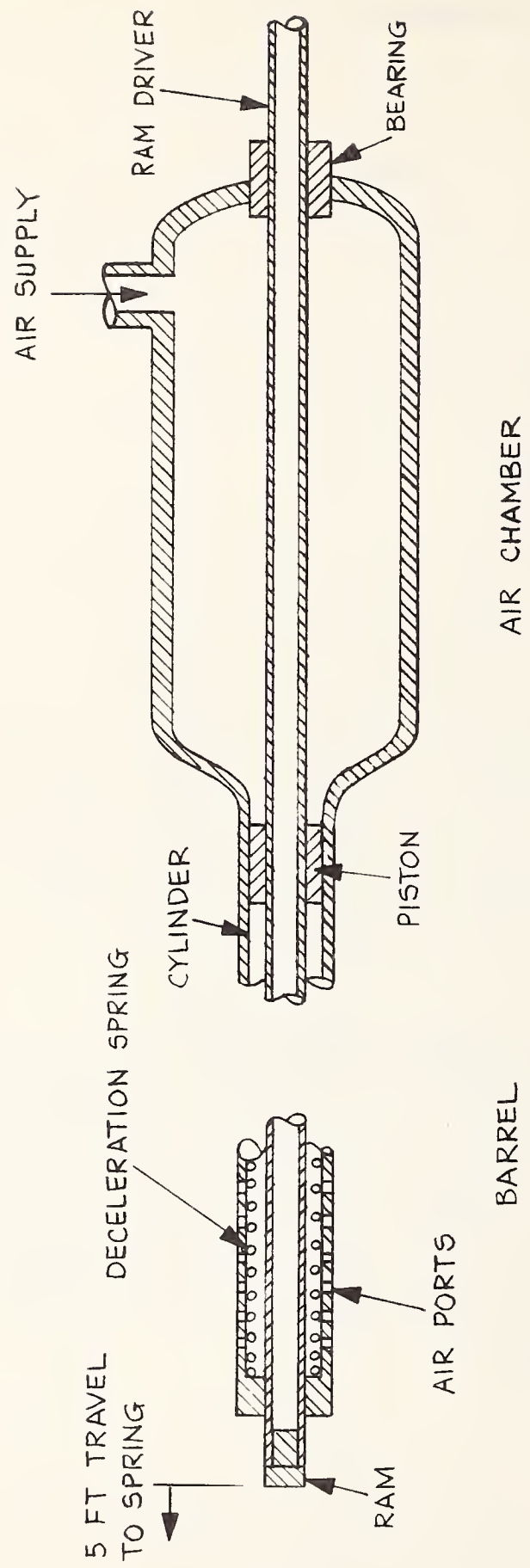


Fig. 3.11 Sketch of Air-Piston Accelerator to Propel Model.

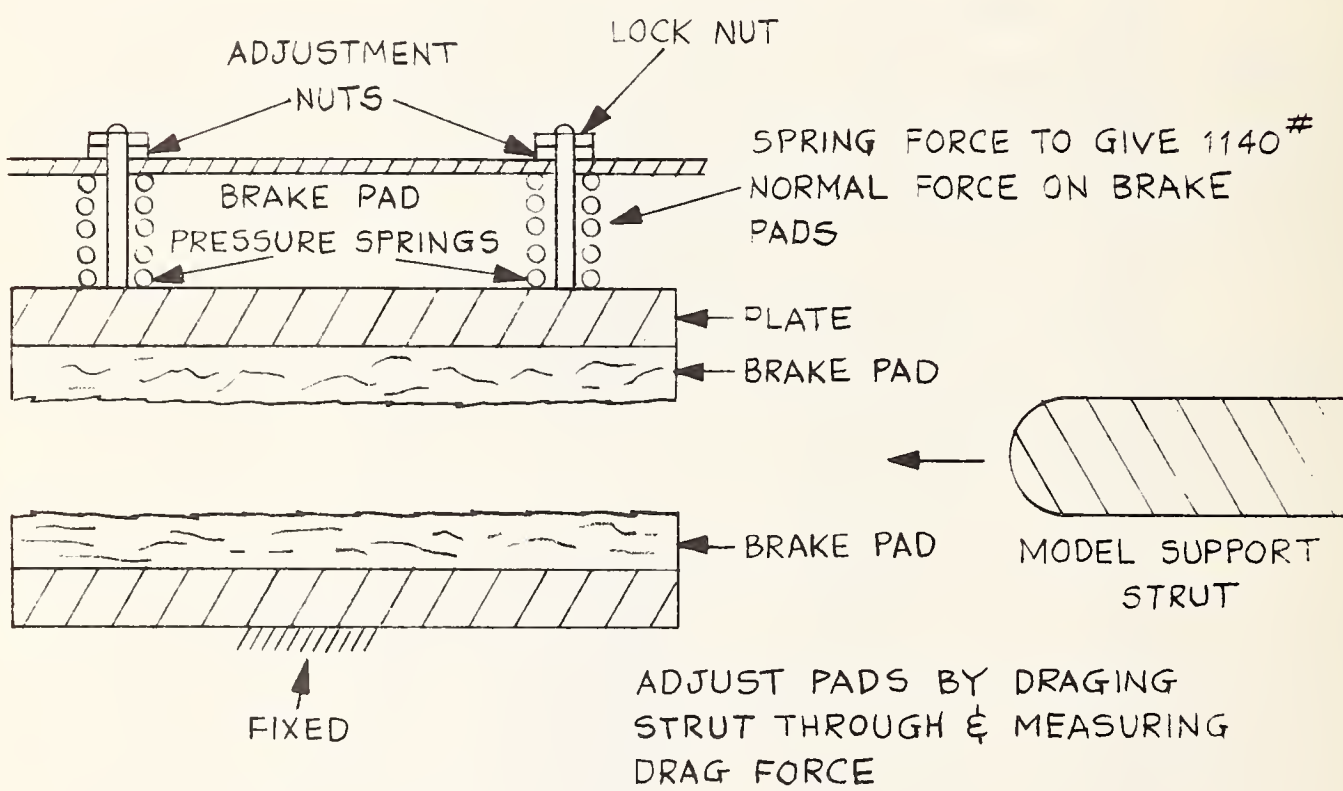
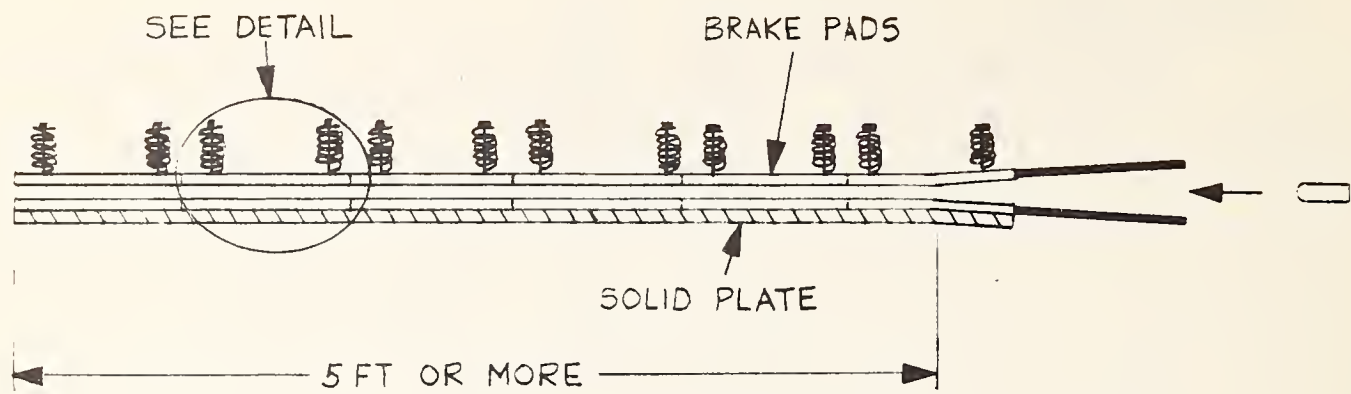
## Decelerator

Many simple schemes for deceleration of the model and carriage are conceivable. Where space is a limitation, the braking scheme sketched in Figure 3.12 provides for nearly constant-force deceleration. In this system, movable brake-shoe pads apply a preset normal force to the strut, between the model and carriage, against the fixed brake shoes. The strut, passing between the fixed and movable brake shoes, forces the adjustment nuts off their seats, enabling the springs to apply their preset force to the brake pads. A typical brake-shoe coefficient of friction of 0.25, to decelerate a 5.7 lb. mass at 50 g's, requires a normal force of 1140 pounds, which is a workable value.

The brake force could be preset by dragging the strut through the brake channel and adjusting to give the desired (moving) drag force. At high speed the friction force could decrease, but the adjustment nuts could be readjusted empirically as test speed is increased.

Another possible deceleration device is depicted in Figure 3.13. This system basically employs a pair of automotive-type shock absorbers connected through a pulley system to an arresting cable which engages the model strut.

Assuming, as previously, a model and carriage system of 5.7 lbs to be decelerated from an initial velocity of 100 ft/sec at the time when the model strut first engages the arresting cable, the total kinetic energy to be dissipated is on the order of 850 ft-lbs. Calculations indicate that a single automotive-type shock absorber with an assumed piston travel of 5 inches should be more than adequate in dissipating 425 ft-lbs of energy within the assumed piston travel limitation. It appears that it may be necessary to design the pulley system with a mechanical advantage sufficient to limit the piston travel in the event that the total downstream travel of the



b. DETAIL OF BRAKE SECTION

Fig. 3.12 Sketch of Channel-Brake for Model Deceleration.

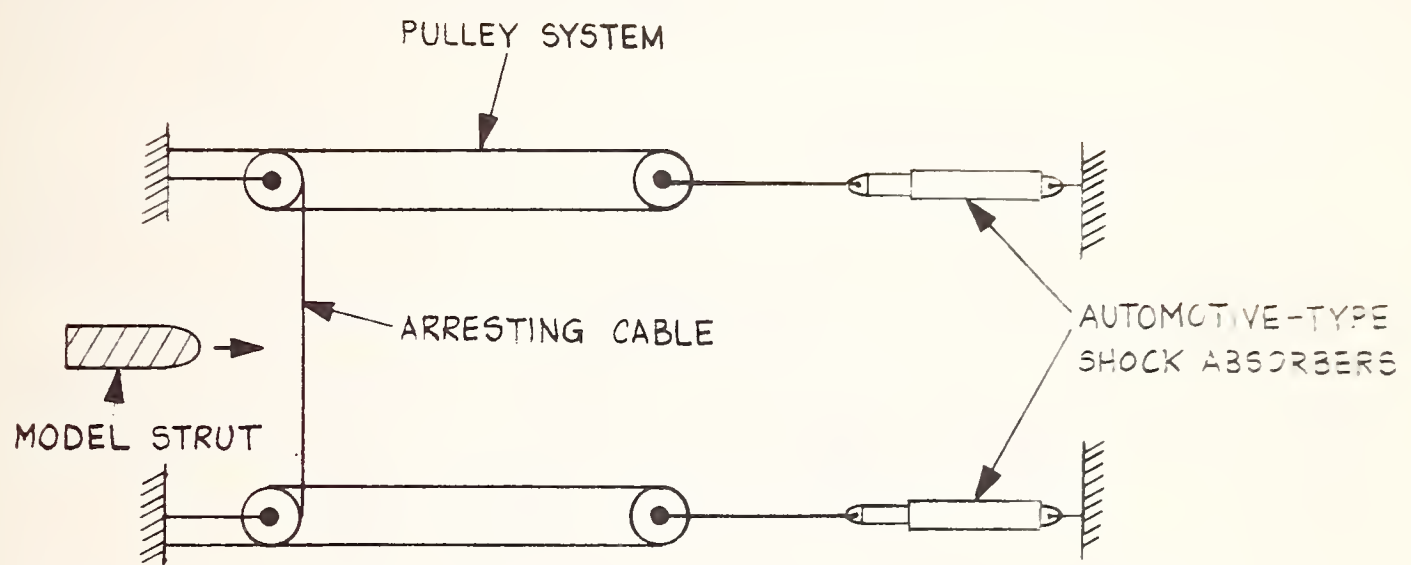


Fig. 3.13 Sketch of Arresting Cable System for Model Deceleration.

arresting cable exceeds the permissible shock-absorber piston displacement.

### 3.5 FORCE AND MOMENT BALANCE

The aerodynamic forces and moments on a model are measured using the balance inside the model. The balance is attached to the support on the carriage. For purposes of analyzing balance response, a rigid model, strut, and carriage are assumed with respect to lateral motion.

#### Response Requirements

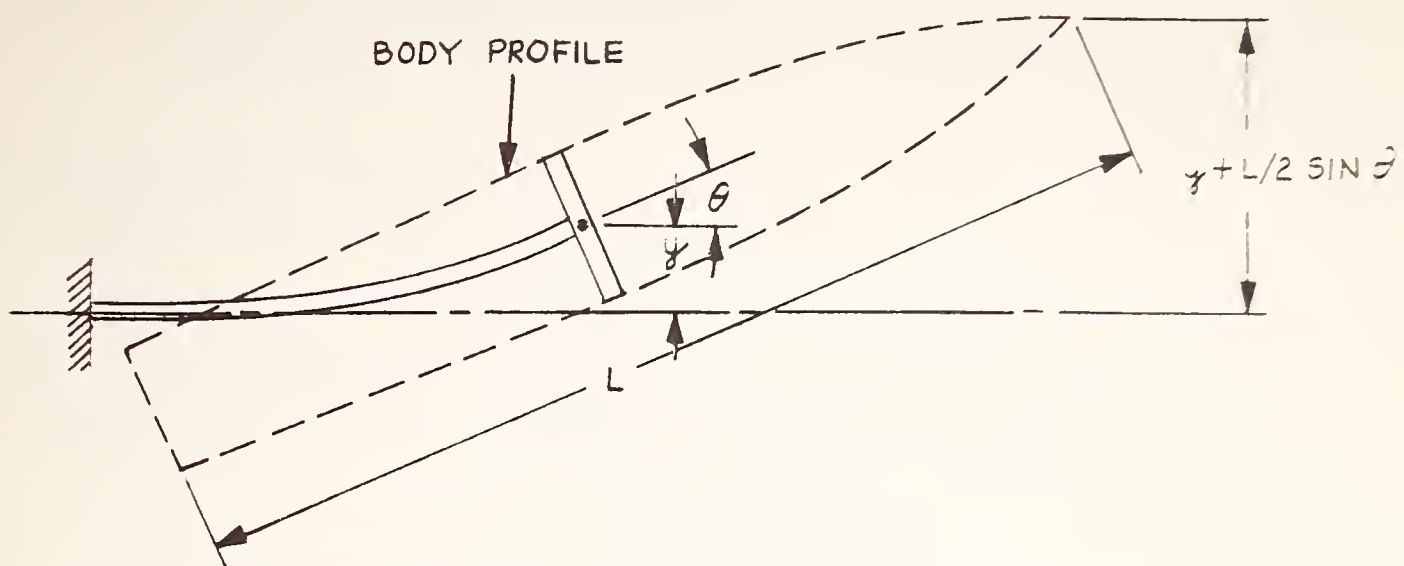
For model III traveling 100 fps through a 5-ft wide wind field, a minimum natural frequency of the model and balance of 100 Hz is assumed for measurement of the transient gust-induced airloads. By damping the balance mechanically, or the signal electrically, a response time of 0.01 second could be obtained.

#### Model Displacement Requirements

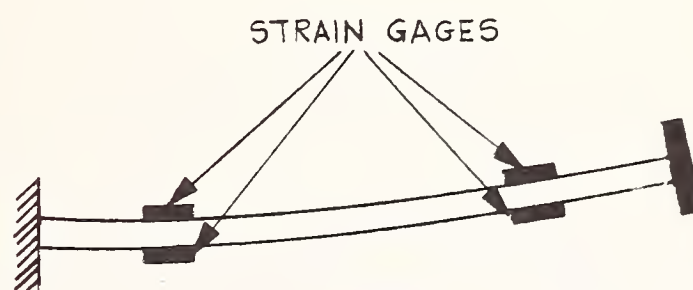
Model displacement must be kept small to maintain the gap between the model and track. For model III, with a 1.2-in width and an estimated minimum gap of 0.02 inches, a maximum lateral static displacement of 0.005 in is taken. Some displacement will occur in the carriage, etc., so a .002-in maximum static displacement of the model is budgeted due to the balance deflection.

#### Side-Force Balance

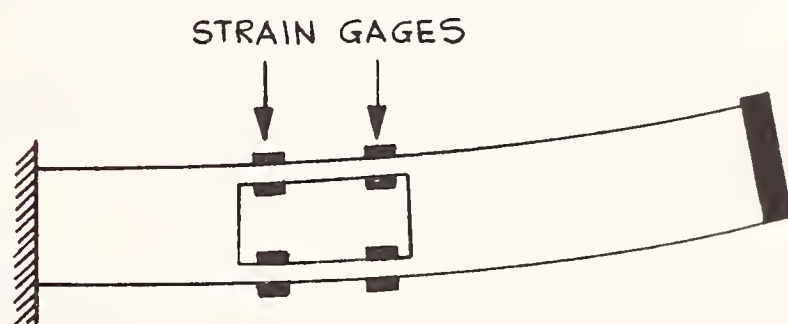
A conceptual sketch of the balance and model body is shown in Figure 3.14a. The balance is a cantilever beam with an applied side force,  $Y$ , and yawing moment,  $M_z$ . By suitable combination of the strain gauges in a bridge, the force and moment are measured individually. The design problem is to



a. CONCEPTUAL SKETCH OF BALANCE AND MODEL



b. RECTANGULAR-SECTION-BEAM BALANCE



c. CUTOUT-BEAM BALANCE

Fig. 3.14 Sketch of Cantilever Side-Force Balance.

achieve a large strain, for measurement purposes, maintaining a high natural frequency of the system and a small model displacement.

The simplest beam section is rectangular with strain gauges mounted on the top and bottom surfaces, Figure 3.14b. The differential strain between the top and bottom surfaces,  $\Delta e$ , is measured. Using semi-conductor strain gauges,  $\Delta e = 50 \mu\text{in/in}$  is taken as a measurable signal having acceptable accuracy. The lowest beam frequency,  $f_1$ , is plotted in Figure 3.15 as a function of the depth of the beam for practical mounting of the strain gauges. The reduced moment of inertia,  $r_o^2$ , defined  $r_o^2 = J/L^2M$ , where  $J$  is the model moment of inertia,  $L$  the model length, and  $M$  the model mass, is taken as unity; the frequency is relatively insensitive to selection of  $r_o$  near unity. The balance beam length is 1. The static deflection of the model nose is also plotted. To achieve a natural frequency of 100 hz, the beam length must be limited to 1 in and the beam depth must be 1 in. This configuration is unworkable due to model dimensions and the low beam length/depth ratio.

The advantage to be gained by reducing model weight and relaxing measurement accuracy is shown in Figure 3.16. It is assumed here model weight is reduced to 0.5 lb and the measured strain to 20 min/in. A natural frequency of 100 hz is readily achieved with  $l = 1$  in and  $d = 0.16$  in. The static nose deflection would be less than 0.002 in.

A cut-out cantilever beam, Figure 3.14c, produces a greater strain signal, at the expense of fabrication simplicity. Basically, relatively weak beam elements can be employed, but deflection is kept down by the large moment arm between the elements. By proper spacing of the elements, the beam moves as an elastic parallelogram.

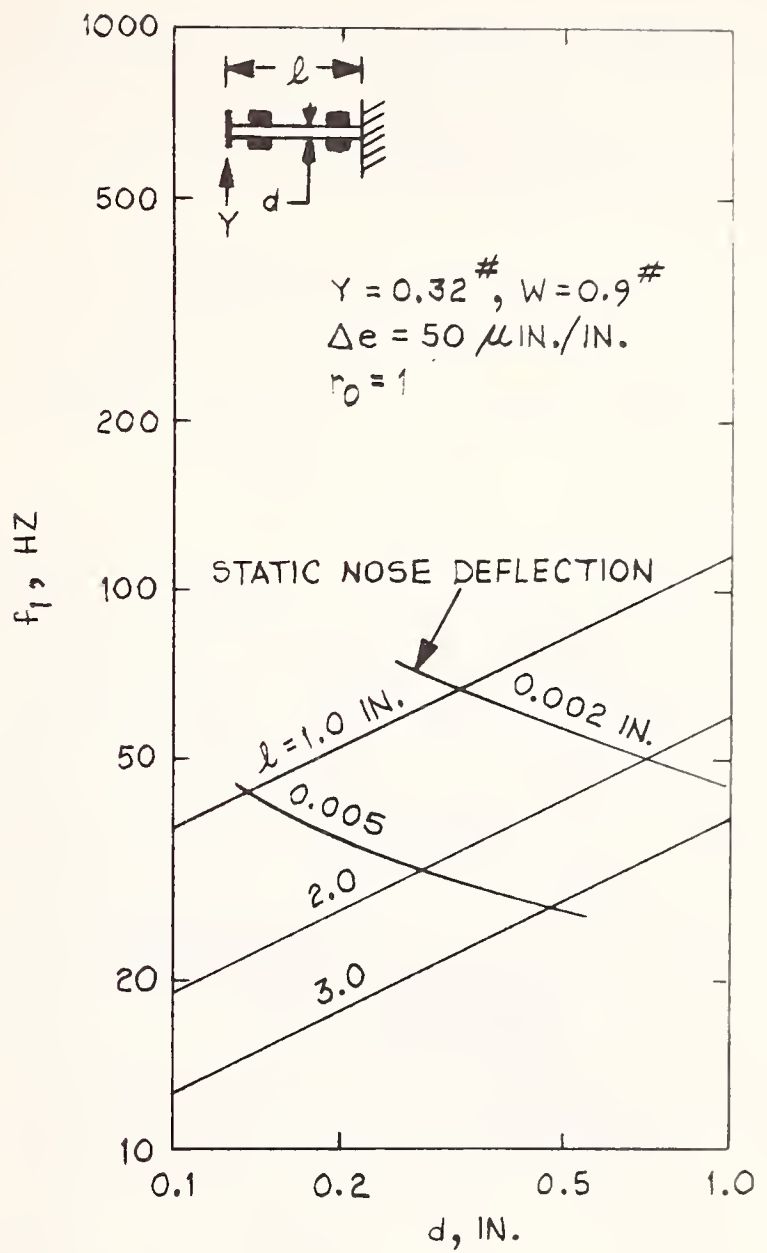


Fig. 3.15 First Frequency and Static Nose Deflection as a Function of Dimensions for Side-Force Balance with Rectangular Beam Cross Section.  $W=0.9 \text{ lb.}$ ,  $\Delta e=50\mu\text{in/in.}$

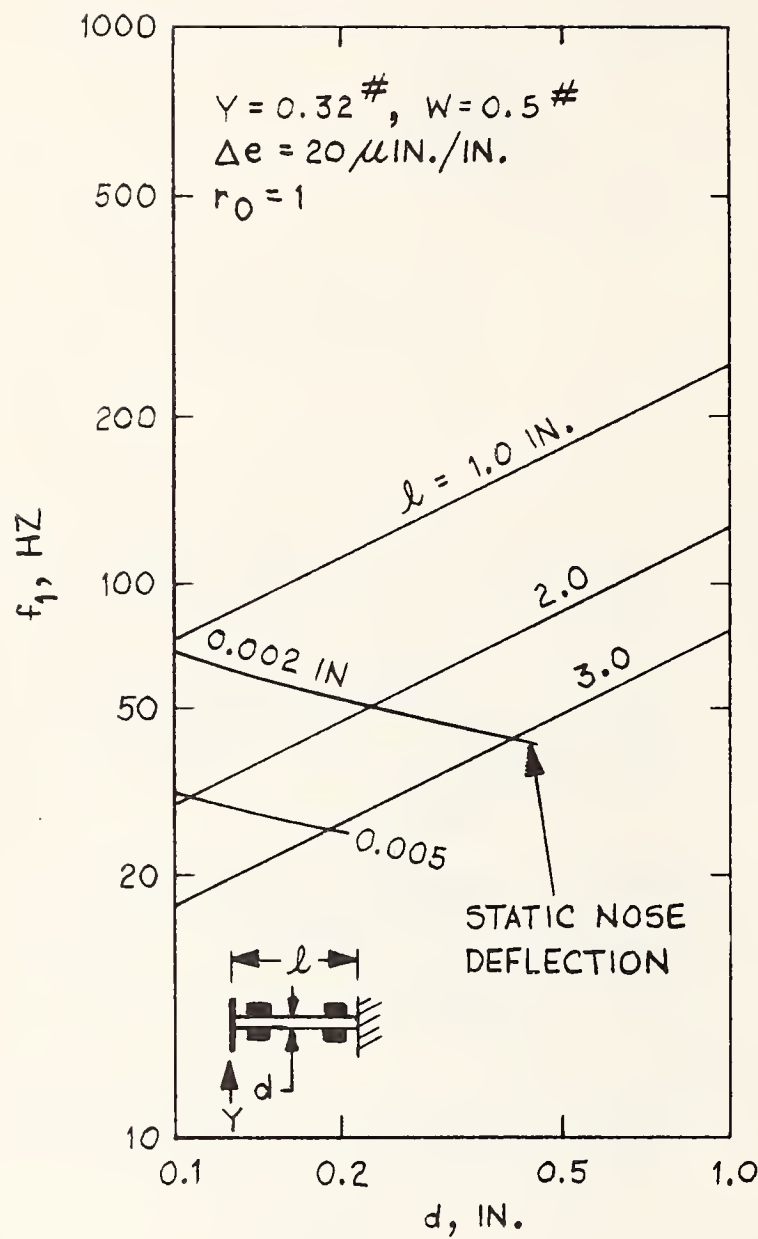


Fig. 3.16 First Frequency and Static Nose Deflection as a Function of Dimensions for Side-Force Balance with Rectangular Beam Cross Section.  $W=0.5 \text{ lb.}$ ,  $\Delta e=20\mu\text{in/in.}$

The natural frequency and static deflection of the cutout beam are plotted in Figure 3.17 as a function of the depth  $d$  of the elements. With  $\ell = 1.0$  in and  $d = 0.1$  in, a natural frequency of 300 cps is obtained and a negligible deflection.

The variation of strain signal,  $\Delta e$ , with natural frequency is plotted in Figure 3.18. For  $\ell = 1.0$  in and  $d = 0.1$  in, a value of  $\Delta e = 400 \mu\text{in/in}$  is achievable for  $f_n = 100$  hz.

For similar requirements of natural frequency and displacement, the signal for a cut-out cantilever beam is about 60 times as great as for a rectangular-cross-section beam.

### Rolling Moment

Figure 3.19 is a sketch of a balance for measuring rolling moment. Cantilever beams are arranged  $90^\circ$  apart around the cross section. Strain gauges on the faces of the beams measure beam bending, which is interpreted in terms of twist. A center post is used to take the axial force of the model.

Using rolling-moment data from Grunwald<sup>2</sup>, the strain in each beam for a 0.9-in diameter balance would be greater than the strain in the elements of the yaw balance, so measurement of the rolling moment would be relatively easily accomplished.

### Yawing Moment

The yawing moment is measured using a simple cantilever beam with a rectangular cross section, Figure 3.20. This configuration was discussed in the side-force measurement, so only the results are given.

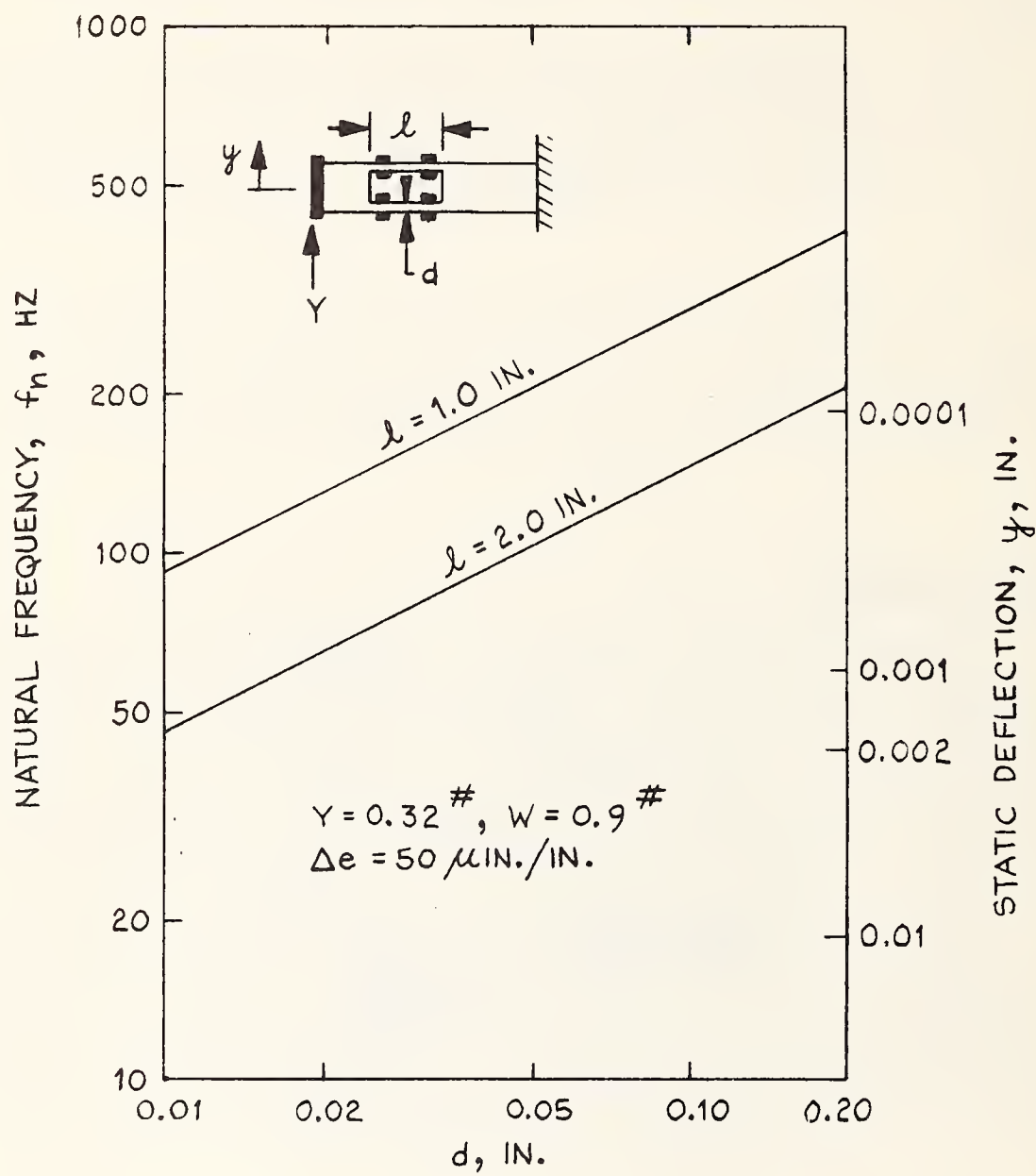


Fig. 3.17 First Frequency and Static Nose Deflection as a Function of Dimensions for Cut-Out-Beam Side-Force Balance.

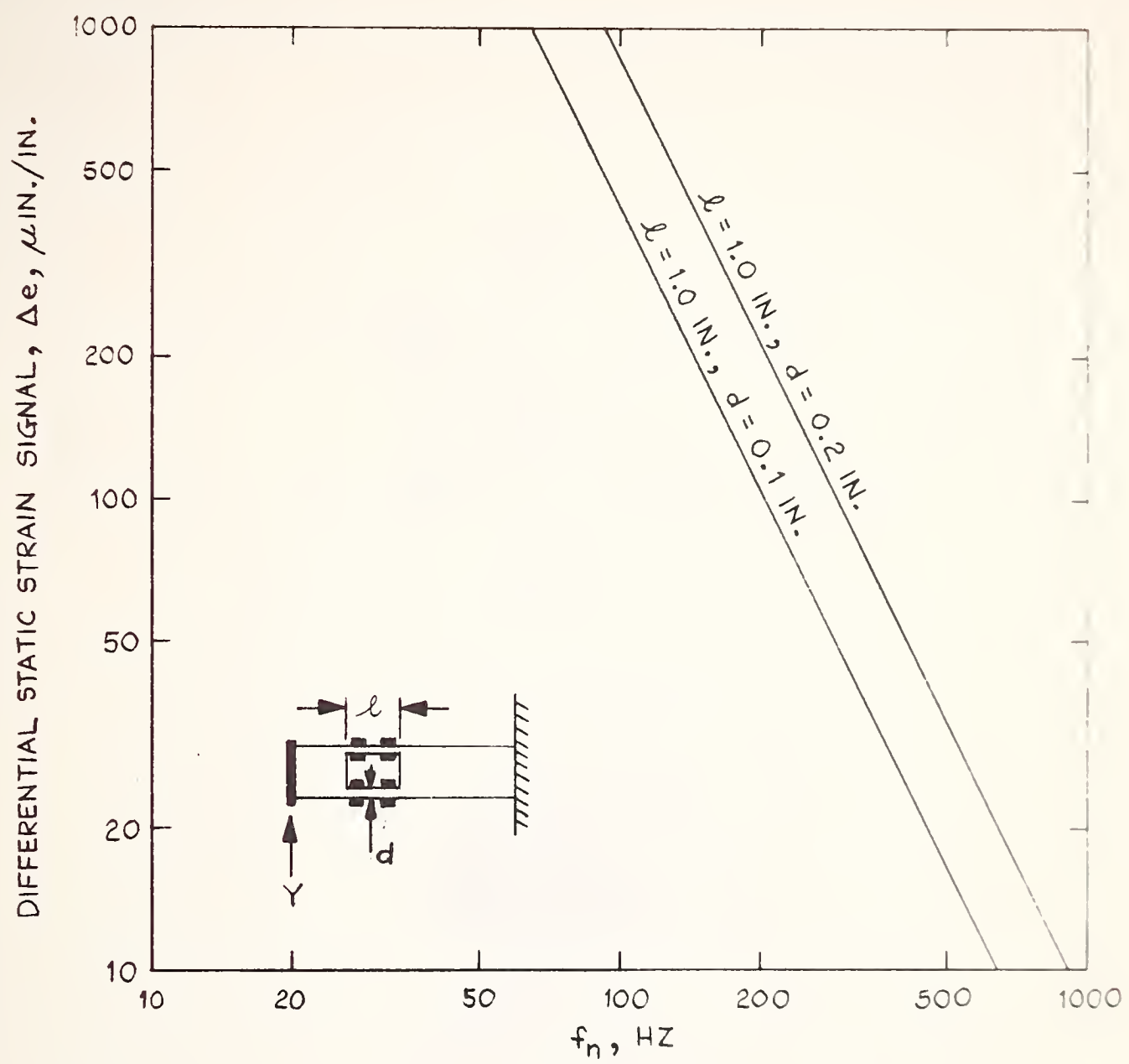


Fig. 3.18 Differential Static Strain Signal as a Function of First Frequency for Cut-Out-Beam Side-Force Balance.

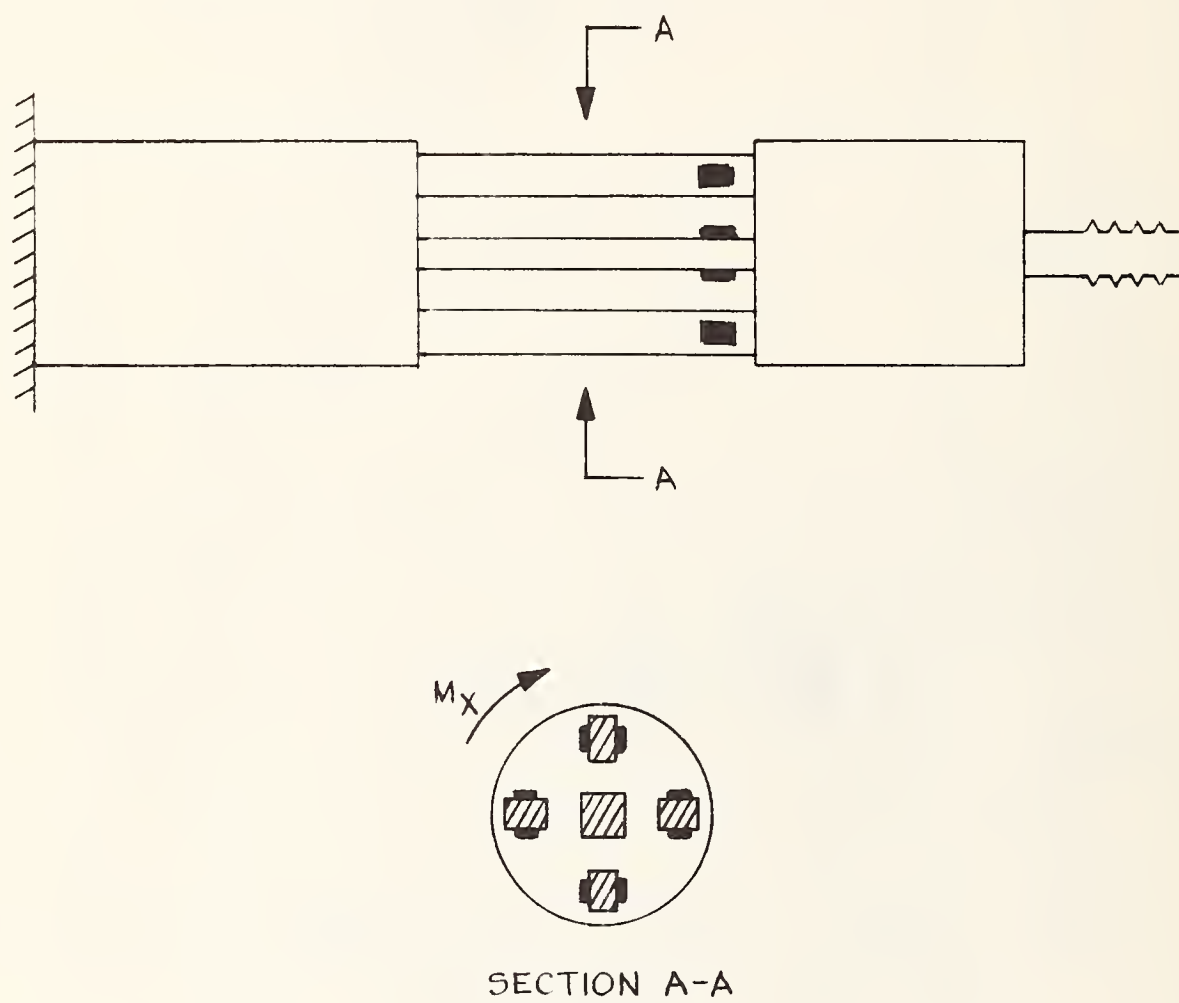


Fig. 3.19 Sketch of Rolling-Moment Balance.

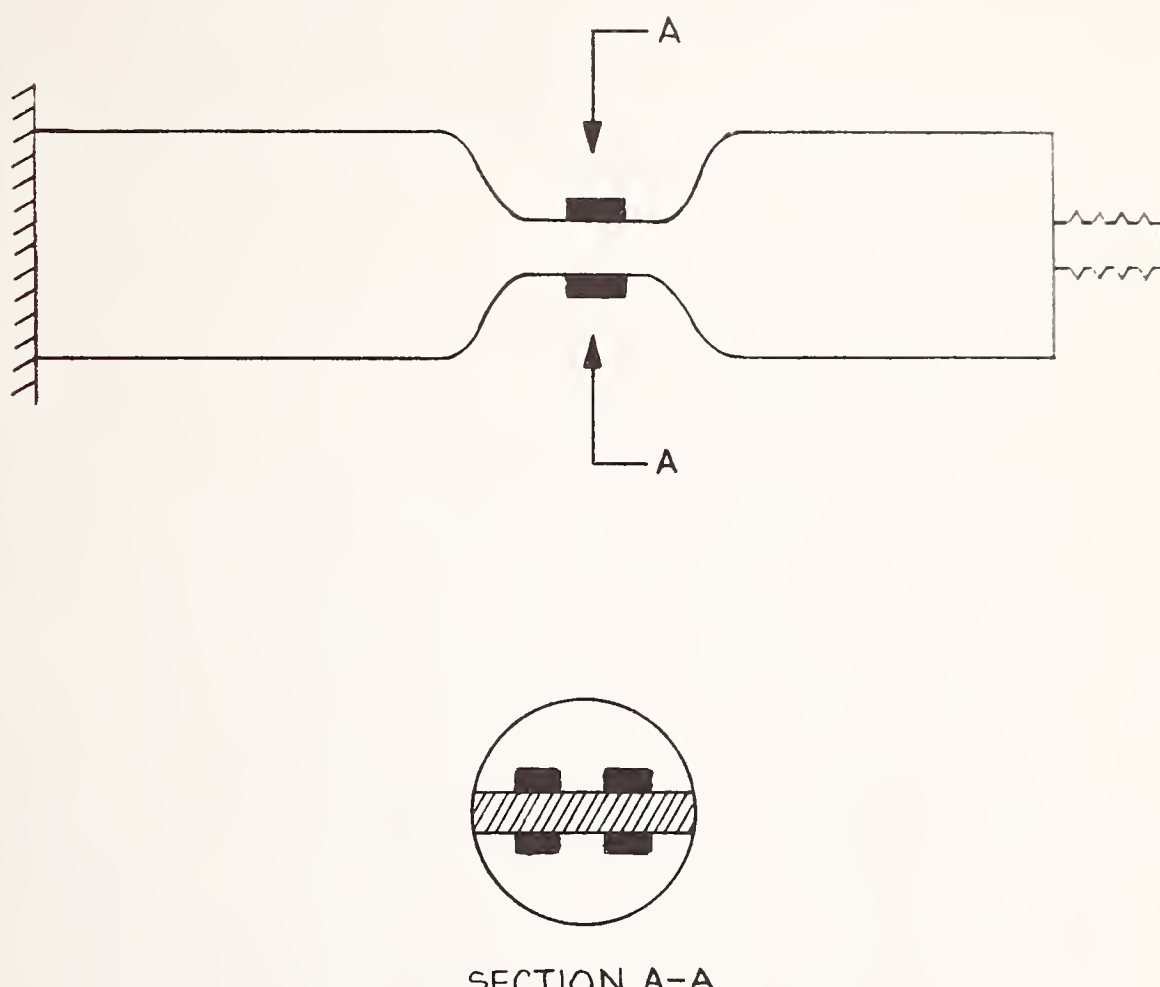


Fig. 3.20 Sketch of Yawing-Moment Balance.

Maintaining an adequate frequency is a problem. A beam with a length of 0.5 in would give a frequency of 93 hz and a deflection of the nose of 0.002 in. This is marginal, but probably close enough to be acceptable.

### 3.6 CONCLUSIONS

To provide a laboratory facility for TACV aerodynamic testing having correct simulation of side gust and ground plane, provision for tests with side-rails and tests of interference from passing trains, the feasibility of a scaled track facility with moving models has been examined.

A facility capable of testing 1-ft-length models (model III) to 100 fps could provide adequate measurement capability, but, because of a low Reynolds number, laminar (instead of turbulent) separation would probably occur, giving data indicating greater side forces on a full-scale TACV than exist. Model vibration from the transport carriage traveling on support ways requires lathe-bed tolerances of the ways in the test area. A 25 to 30-ft track is needed: a 5-ft section to accelerate a model, a 15 to 20-ft section for testing, and a 5-ft section for deceleration. It appears feasible to measure side force, rolling moment and yawing moment using available semiconductor strain gauges.

A larger facility, capable of testing 4 to 5-ft length models to 250 fps, would provide greater ease of measurement and less stringent requirements on support way tolerance (equivalent to new runway construction). Reynolds number simulation would be ample. A 120 to 140-ft track should be satisfactory: a 30-ft section for acceleration, a 60 to 80-ft section for testing, and a 30-ft section for deceleration.

Developing the smaller facility (1-ft models) first is expected to enable solution of test problems more readily because of the reduced size of the facility. The instrumentation and vibration problems appear more difficult, but, by

relaxing the accuracy requirements somewhat, interim tests of value could be performed.

For rapid acceleration of 1-ft models, a cable system may be workable, but vibration problems associated with cable acceleration must be solved. An air-piston-and-ram system appears to provide simple construction and controllable acceleration. For rapid deceleration, either a brake-shoe system or cable arresting system could be employed. The latter would appear to offer advantages in fabrication simplicity.



#### 4. REFERENCES

1. Ruetenik, J. R., and Brooks, W. B., Transient Airloads on a Body of Revolution Due to Indicial Sinking at a Large Angle of Attack, MIT, ASRL TR 121-1, August 1964.
2. Grunwald, K. J., Aerodynamic Characteristics of Vehicle Bodies at Crosswind Conditions in Ground Proximity, NASA TN D-5935, August 1970.
3. Perkins, E. W. and Jorgenson, L. H., Comparison of Experimental and Theoretical Normal-Force Distributions (including Reynolds Number effects) on an Ogive-Cylinder Body at Mach Number 1.98, NACA TN 3716, 1956.
4. Nielsen, J. N., Missile Aerodynamics, McGraw-Hill Book Company, Inc., New York, 1960.
5. Miles, J. W., Transient Loading of Slender Bodies of Revolution, U. S. Naval Ordnance Report No. 2052, Inyokern, California, 1953.
6. Bryson, A. E., Symmetric Vortex Separation on Circular Cylinders and Cones, Journal of Applied Mechanics, p. 643-48, December 1959.
7. Schindel, L. H., and Chamberlain, T. E., Vortex Separation on Slender Bodies of Elliptic Cross Section, MIT Aerophysics Laboratory, Tech. Report 138, August 1967.
8. Allen, H. J., Estimation of the Forces and Moments Acting on Inclined Bodies of Revolution of High Fineness Ratios, NACA RM A91 26, 1949.
9. Roshko, A., On the Drag and Shedding Frequency of Two-Dimensional Bluff Bodies, Calif. Inst. of Tech., NACA Report TN 3169, July 1954.
10. Woolard, Henry W., Slender-Body Aerodynamics for High-Speed Ground Vehicles, Journal of Aircraft, pp. 597 - 602, August 1971.



HE 18.5 A38  
no.DOT-TSC-171-  
1

171  
air  
BORROWER

Form DOT F 1720.2 (8  
FORMERLY FORM DOT F 1700

DOT LIBRARY



00351905